University of Leoben

Dissertation

Fracture of ultrafine-grained metals produced by severe plastic deformation

Anton Hohenwarter

Leoben, June 2010

This work was financially supported by the Christian Doppler Society.

Erich Schmid Institute of Materials Science
Austrian Academy of Sciences
Jahnstrasse 12
A–8700 Leoben

This thesis was typeset by the use of KOMA-Script and LaTeX 2_ε.

Affidavit

I declare in lieu and oath, that I wrote this thesis and performed the associated research myself, using only literature cited in this volume.

Leoben, June 2010

Danksagung

Zunächst möchte ich mich bei meinem Betreuer, Prof. Dr. Reinhard Pippan, für die Übertragung und Betreuung dieser Dissertation, für sein Entgegenkommen in jeglicher Hinsicht und seinen Blick fürs Wesentliche bedanken. Großen Dank gilt zugleich auch meinen Industriepartnern Dr. Peter Pointner und DI Richard Stock von der voestAlpine Schienen GmbH für die gute Zusammenarbeit und vor allem auch für die Toleranz Zeit und Geld in Grundlagenwissenschaft zu investieren. Hier ist an gleicher Stelle auch der Christian Doppler Forschungsgesellschaft zu danken.

Als nächstes möchte ich mich bei der ganzen Belegschaft des Erich Schmid Instituts bedanken. Besonders zu nennen sind an dieser Stelle die Jungs von der Werkstatt, Günter Aschauer, Hubner Franz und der Junglehrer Hannes Schlager. Jeder von Ihnen hat mit ihren Engagement und Einfallsreichtum zum Gelingen dieser Arbeit beigetragen. Weiters habe ich mich auch bei den Damen aus der Metallographie, Traudi, Gabi und Silke, für die prompte und gewissenhafte Erledigung von Arbeiten zu bedanken. Für administrative Probleme und Fragen hatte Doris Schrutt und Marianne Fliesser stehts ein offenes Ohr - ein herzliches Danke. Auch Peter Kutleša sei hier eigens erwähnt, der mir mit seinem Humor und Einsatzbereitschaft stehts eine große Hilfe war.

Außerdem danke ich allen "studentischen" Arbeitskollegen, die als Dissertanten und Diplomanden sozusagen im gleichen Boot saßen. Während der Arbeit hatten wir gemeinsam viel Spass und die Möglichkeit voneinander zu lernen. Ganz speziell will ich hier meinen "Dude" Gludovatz Bernd erwähnen, der wirklich eine Ahnung von Computer hat und auch ein toller Reiseleiter ist. Dein Engagement für Dinge aller Art auch abseits des Instituts ist phänomenal! Weiters bedanke ich mich auch bei meinen Bürokollegen für die gemeinsame illustre Zeit: Aidan Taylor (Musik-DJ, Tem-Spezialist und Lektor), Bo Yang (Mr. Smile) und Georg Rathmayr (Hobby-Rechtsgelehrter). Besonderer Dank gilt auch Martin Rester, Daniel Kiener, Stefan Wurster, Christoph Kammerhofer und Stephan Scheriau für ihre Mithilfe und Diskussionsbereitschaft in wissenschaftlichen und auch nicht-wissenschaftlichen Belangen.

Zum Schluss möchte ich mich speziell bei meiner ganzen Familie für euren Rückhalt und Optimismus bedanken. Last but definetely not least will ich mich bei Megan für die tolle Zeit bedanken, die wir in den letzten Jahren gemeinsam verbracht haben und auch in Zukunft verbringen werden - Thanks MJ!

Abstract

In the last two decades bulk solids with grain sizes typically smaller than 1 μm down to several nanometers have attracted great scientific interest driven by their promising enhanced mechanical and physical properties. Among different possibilities to produce such materials the Severe Plastic Deformation (SPD) approach has possibly gained the most prominence currently reflected by the large number of publications in this field. This is mainly due to the technical simplicity of most processes and the large variety of processable materials. Besides classical mechanical material parameters, like strength or hardness after SPD processing, the fracture toughness is also of great concern, especially when structural applications are planned in future. Despite this, the fracture behavior of such materials has been widely omitted in the SPD community so far.

In this thesis for the first time an extensive study into the fracture behavior of different SPD processed materials has been conducted. Main work was done on an one phase bcc and fcc metal, namely Armco iron and nickel. Additionally also a steel with a fully pearlitic microstructure was under investigation where experiments were performed as a function of pre-deformation. Special focus was given on a possible influence of the testing direction on the fracture toughness results.

It will be shown that the deformation microstructure causes an intensive anisotropy in the fracture behavior from brittle to ductile fracture in the investigated bcc materials, Armco iron and the pearlitic steel. The anisotropy was related to one testing direction of fairly low fracture toughness which simultaneously favored a strong enhancement in the other directions. In contrast to this the fcc-example, Nickel, exhibited a good combination of strength and fracture toughness. The high fracture toughness and the less pronounced anisotropy are a result of the occuring ductile fracture compared to the brittle intercrystalline fracture of iron.

Contents

Affidavit III

Danksagung V

Abstract VII

1 Motivation and aim of the present work 1

2 Introduction 3
2.1 Grain refinement by severe plastic deformation 3
2.2 Short overview on SPD techniques 4

3 Summary of the results from the thesis 7
3.1 Investigated materials 7
3.1.1 HPT processed metals with steady state microstructures . . . 8
3.1.2 HPT processed metals without steady state microstructures . 11
3.2 Fracture toughness measurements 13
3.2.1 Specimens orientations 13
3.2.2 Fracture toughness of Armco iron 14
3.2.3 Pearlitic steel R260 17
3.2.4 Nickel 19
3.2.5 Comparison of the fracture behavior 24

4 Conclusions 29

5 List of appended papers 35

A Technical parameters affecting grain refinement by high pressure torsion 37
A.1 Introduction 38
A.2 An overview of HPT equipment 39
A.2.1 The idealised HPT process 39
A.2.2 Real HPT 40
A.3 Technical factors affecting HPT results 41
A.3.1 The HPT setup 41
A.3.2 The applied pressure 41

A.4 Upscaling of HPT and limitations of the sample size 44
A.4.1 Technical aspects 44
A.4.2 The homogeneity of deformation 45
A.5 Summary 52

B Severe plastic deformation of a bainitic rail steel 55
B.1 Introduction 56
B.2 Experimental 56
B.3 Microstructure of the starting material 57
B.4 Microstructural changes due to High Pressure Torsion 58
B.5 Mechanical measurements 58
B.6 Concluding remarks 60

C Anisotropic fracture behavior of ultrafine-grained iron 65
C.1 Introduction 66
C.2 Experimental 66
C.3 Results 68
C.3.1 Microstructure 68
C.3.2 Tensile tests 69
C.3.3 Fracture toughness measurements 70
C.3.4 Fractography 72
C.4 Discussion 74
C.4.1 Anisotropy of the fracture toughness 74
C.4.2 A method for improving the fracture toughness 78
C.5 Conclusions and summary 79

D Effect of large shear deformations on the fracture behavior of a fully pearlitic steel 83
D.1 Introduction 84
D.2 Experimental 84
D.3 Results 86
D.3.1 Evolution of the microstructure 86
D.3.2 Changes in the hardness 88
D.4 Discussion 90
D.4.1 Microstructure and hardness 90
D.4.2 Evolving anisotropy in the fracture toughness 91
D.5 Summary and conclusions 97

E The ductile to brittle transition of ultrafine-grained Armco iron: an experimental study 101
E.1 Introduction 102

E.2 Experimental 102
E.3 Results 104
E.3.1 Microstructure 104
E.3.2 Fracture toughness results 104
E.4 Discussion 107
E.4.1 Dependency of the DBTT on grain size 107
E.4.2 The influence of the crack plane orientation on the DBTT . . 110
E.5 Conclusions and summary 113

1

Motivation and aim of the present work

Ultrafine-grained (UFG) and nanocrystalline (NC) metals obtained via various Severe Plastic Deformation (SPD) processes commonly exhibit a variety of improved mechanical and physical properties. Experimental results can be found in different comprehensive overview articles [1–3]. Often the ductility of these materials is deteriorated as usually seen after cold working. Despite this different strategies have been suggested and seem to be successful in certain cases to overcome this strong limitation. For instance, by introducing second-phase particles [4], using bimodal grain-size structures [5], or changing the strain rate in a wide range [6]. Besides the ductility of a metal, the fracture toughness, describing the resistance against crack propagation, has to also be considered. Firstly for a possible safe implementation for structural applications and secondly, to obtain a more objective view onto the deformation and fracture behavior of these metals. On the contrary the fracture properties have been widely neglected by the SPD-community with only some exceptions [7–10]. From the fracture mechanics viewpoint, SPD processed metals also give the opportunity to perform basic research on pure metals (e.g. the ductile to brittle transition) with grain sizes which have not been accessible so far in the past.

These considerations motivated to deepen the understanding for the underlying fracture processes of SPD processed metals and to obtain mechanical measurements in order to classify their performance enabling a comparison with traditional used materials. In this thesis for the first time a systematic study into the fracture behavior of different metals and alloys deformed by HPT was performed. The fracture behavior assessed by fracture toughness measurements were performed for different crack plane orientations in order to get a more versatile look onto the fracture behavior. The measurements cover classical one phase metals, for example iron and nickel in their SPD-state, but also treat the fracture behavior of a classical pearlitic steel representing a two phase material, which is normally used as a rail material. In such

a material severely plastically deformed surface layers can arise naturally during the rail-wheel contact [11]. The contact can be characterized by high compressive forces and large shear stresses, which finally leads to a strong plastic deformation of the rail surface which often form the initiation point of RCF (Roll Cycle Fatigue) related crack like defects such as head-checks and squats [12].

After a short introduction into SPD the results of the thesis will be presented in the following sections. In the conclusion the new findings including similarities regarding the different materials will be elucidated. In the end the publications originating from this work are attached.

2 Introduction

2.1 Grain refinement by severe plastic deformation

In metal physics various methods to increase the strength of metals and alloys are known. Among the classical hardening mechanisms, such as precipitation and dispersion hardening, solid solution strengthening and cold work hardening, grain refinement resembles possibly the most prominent hardening mechanism, which is still under extensive investigation today. This is because grain refinement down to microstructural sizes smaller than 1 μm, so called ultrafine-grained metals or even smaller than 100 nm, named nanocrystalline metals, promise outstanding physical and mechanical properties [13–19].

Considering pure single phase metals, excluding here steels with their large possibilities of thermomechanical treatments, grain refinement can be achieved by strong cold working followed often by a recrystallization treatment. To induce the cold working, classical deformation techniques such as rolling, forging and drawing are in use. These techniques mainly lead to microstructures in the range of several micrometers when combinations of single deformation steps followed by heat-treatments are performed since during the deformation also damage evolves, which restricts the maximum deformation to a certain extent. This limitation depends mainly on the characteristic stress state of the deformation process and the temperature. On the contrary for a stronger grain refinement additional cold working would be needed. In order to exceed these technological limits different other approaches have been elaborated. Regarding their synthesis process these techniques can be divided into bottom-up and top-down approaches [20]. Examples for bottom-up processes where already nanocrystalline units become assembled to bulk material are electrodeposition, inert gas condensation and powder compaction.

The second group of approaches, the top-down processes pursue a refinement of a coarse structured bulk material into a nanostructured material. The most popular representative in this group is grain refinement through Severe Plastic Deformation (SPD). In contrast to the aforementioned classical deformation techniques these processes posses the ability to impose very large strains, typically in the order of hundreds of percents onto a metal without large changes of the specimen dimensions [21]. Due to the very large imposed strains a strong grain refinement is induced. Explanation approaches for the processes behind the grain fragmentation can be found e.g. in [22–24]. Such techniques for the production of ultrafine-grained and nanocrystalline metals have become fairly popular in the last two decades. The growing interest for SPD is also reflected by the huge number of papers and conferences devoted to the mechanical and physical properties of these materials. The majority of successful work nowadays done in this field can be backtracked to three major techniques, namely Accumulative Roll Bonding (ARB), Equal Channel Angular Pressing (ECAP) and High Pressure Torsion (HPT). They will be described shortly in the following section.

2.2 Short overview on SPD techniques

Accumulative Roll Bonding (ARB) descends from a very similar fabrication technique consisting of several forging and folding steps for the production of swords used more than 2000 thousands year ago in China [25]. In the modern version a metal sheet is rolled to the half of the initial thickness, then cut into two pieces of the same size, stacked together and rolled again. Through degreasing and wire-brushing the surfaces an appropriate bonding in the next deformation step [26] is obtained through cold welding. By repeating the aforementioned procedure many layers can be introduced into the sheet. The number of layers scales with 2^n where n is the number of steps. Considering a sheet of 1 mm thickness and 10 deformation steps a layer thickness of about 100 nm is reached. Advantages of this technique can be seen in the simple use of already existing rolling devices and the efficiency of the nanostructurization. Disadvantages are the fact that this process is exclusively working with ductile materials having a rather low melting point, the introduction of a huge number of interfaces that could lead to additional impurities and some technological problems, for instance crack formation at the margins of the sheet.

Equal Channel Angular Pressing (ECAP) The origins of this popular deformation technique go back to principle works performed by Segal [27]. Here two channels of the same cross section intersect under a certain angle, which defines the degree of shear deformation per step. A metal billet is pressed through the channel and shear deformed in the intersection of the channels. By varying the way the billet is inserted into the channel in the subsequent deformation steps,(e.g. it can be rotated 90 degrees around the long axis with respect to the first deformation step), different deformation routes can be established [2]. The major advantage of this technique is the size of the processed billets, especially when industrialization

is considered. Drawbacks are the absence of hydrostatic pressure that can be partly overcome by using back pressure, the resulting limitation in deformation strain and the restriction to rather soft materials.

The principles of **High Pressure Torsion (HPT)** were given by Bridgman [28], who found that the fracture strain in torsional tests can be strongly increased by imposing hydrostatic pressure. This basic concept was picked up again by Russian scientists in the 1980s and is nowadays called HPT [3]. Here a penny shaped specimen is placed between two anvils, subjected to high pressures and consequently torsional strained without slip between anvil and specimen. The deformation strain in terms of the von Mises equivalent strain ϵ_{vM} can be evaluated with

$$\epsilon_{\mathrm{vM}} = \frac{2\pi r}{t\sqrt{3}} n. \tag{2.1}$$

Here r is the radius, t the thickness of the specimen and n the number of revolutions. A drawback of this technique must be seen in the strain gradient that samples posses and often leads to the misunderstanding that the specimens exhibit an inhomogenous microstructure. Furthermore the restricted specimen size is criticized, but can, as will be shown later, be easily overcome by upscaling the process. Significant advantages are the possibility to process brittle metals, such as tungsten [29] or intermetallics [30] whereas the degree of deformation is almost unrestricted. A further point is that no porosity or chemical changes can be introduced during straining as to be considered for various bottom-up processes. Moreover the setup is fairly simple so that experiments at elevated or cryogenic temperature can be performed. Due to the importance of this process and the basic requirement to upscale the specimen size for this thesis Paper A is devoted to HPT giving more details concerning this deformation technique.

Besides these techniques, used mostly on the laboratory scale, other processes have emerged over the last years with potential for industrialization. Some of these new techniques are derived from the traditional ECAP process transformed into a continuous technique, such as the conshearing process [31], the continuous confined strip shearing process (C2S2) [32] and ECAP-Conform [33]. Another notable attempts for commercialization derived from HPT are continuous HPT [34] and the torsion extrusion process [35].

3

Summary of the results from the thesis

An essential requirement for the measurements and especially to account for the influence of different crack propagation directions in SPD materials was to increase the size of the specimens. For that reason a new deformation tool with a loading capacity of 4 MN and a maximum torque of 13 KNm was planned and acquired by our SPD group [36]. A feasibility study regarding a possible useful size of the specimens and the expected homogeneity in radial and axial direction were conducted. Details referring basic rules for upscaling the HPT process and a profound study into the homogeneity of HPT processed metals is given in Paper A.

3.1 Investigated materials

The main work of the thesis was performed with the pure metals Armco iron (∼99.9 wt%) and Nickel (∼99.7 wt%), as well as a two phase pearlitic steel, denominated as R 260. The chemical composition of these materials is given in Table 3.1.

Table 3.1 Chemical composition of the main investigated materials. Numbers are given in weight percent [wt%]

Material	C	Mn	P	S	Si	Co	Cu	
Armco Fe	0.009	0.06	0.009	0.007	-	-	-	Fe in balance
Ni	0.01	0.03	0.02	$\prec$ 0.003	0.02	0.03	0.16	Ni in balance
R260	0.76	1	0.017	0.014	0.35	-	-	Fe in balance

Further investigations, in order to clarify certain fracture aspects, were performed on an Fe-based alloy named P 800 and an iron with a purity of 99.99 wt%. Experimental details will be given in the individual papers, only some basic data regarding the HPT deformation process are outlined. High Pressure Torsion of the pure metals was performed at a nominal pressure of 2.8 GPa up to 10 rotations to obtain the starting materials for the further experiments. The pearlitic steel was deformed up to 1, 2 and 3 rotations at a nominal pressure of 5.4 GPa. For the interpretation of the results the obtained microstructures after HPT are of great importance and will be shortly discussed in the following.

3.1.1 HPT processed metals with steady state microstructures

In Figure 3.1 typical micrographs of microstructures deformed up to the saturation regime are shown. Saturation in this context means that a maximum of grain refinement or a minimum grain size during the fragmentation process is reached [37].

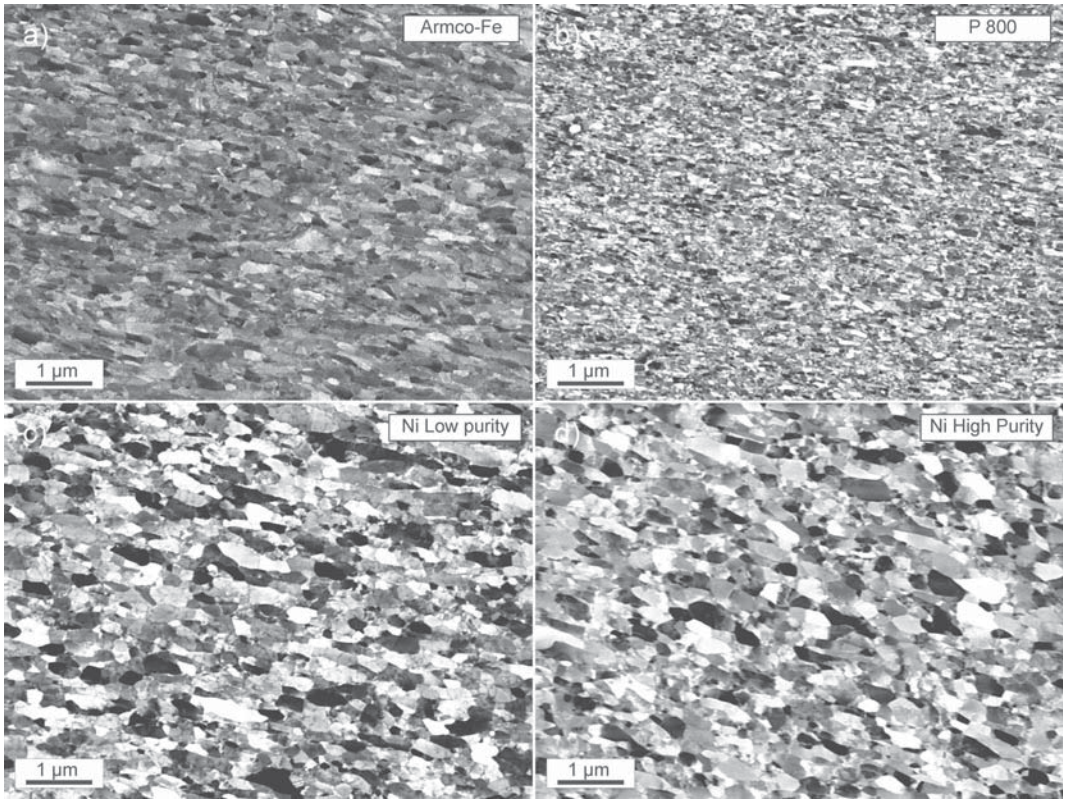

Figure 3.1 Overview micrographs of SPD deformed metals in the steady state looking into the radial direction. Similarities such as the elongated grain structure and the inclination of the grains with respect to the shear direction are recognizable.

A further increase in strain does not lead to an additional refinement. The minimum grain size, also termed steady state grain size, depends on various factors, such as the material itself and the processing temperature [38], purity of the material [39] and strain rate [40]. The influence of the pressure leads to deviating results from no influence [41] to a pronounced influence [42]. Besides the investigated one phase microstructures Ni with a high purity (99.99 wt%) is also shown in order to show the effect of purity on the grain size in comparsion with a Nickel of lower purity (99.7 wt%). Typical for the radial observation direction is that, independent of the material, especially regarding purity and crystal structure similarities can be found typical of SPD deformation. The grains exhibit after room temperature deformation a pronounced elongated grain structure and an inclination with respect to the shear direction, which is parallel to the long margins of the micrographs, as found in [43] for HPT, however also present in metals subjected to ECAP [44]. The elongation of the grains is normally in Transmission Electron Microscopy (TEM) micrographs better to recognize as shown in Fig. 3.2a and b for Armco iron and Nickel, respectively. Due to the TEM preparation process the information of the inclination with respect to an outer coordinate system gets lost.

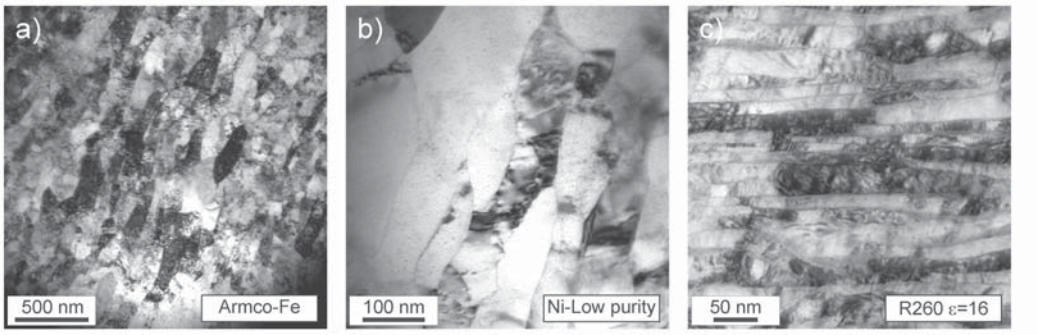

Figure 3.2 Overview of the main investigated materials investigated with TEM brightfield contrast.The pure metals (a) Armco iron and (b) Nickel show an elongated grain structure. The pearlitic steel (c) exhibits an alignment of the lamellae into the shear direction.

The grain sizes in the saturation regime varies between well bellow 100 nm for the P800 alloy and about 300 nm for Ni with the 99.99 wt% quality. Nickel with the lower quality and Armco iron have a grain size of about 200 nm.

The grain size is only an estimate but the trend in the differences is reflected by hardness measurements, see Fig. 3.3. Here the hardness after 10 rotations for different one phase materials is plotted. Besides the trends in the grain size a more significant aspect important for this work can be found. In large parts of the disc an almost homogenous hardness is present along the radius, which reflects directly the existence of a steady state grain size. After 10 rotations the minimum strain for maximum grain refinement is already reached at small radii and thus a large part of the disc exhibits the same hardness as shown before in [45, 46]. The required minimum strain is at room temperature around ϵ_{vM}=16 for one phase materials.

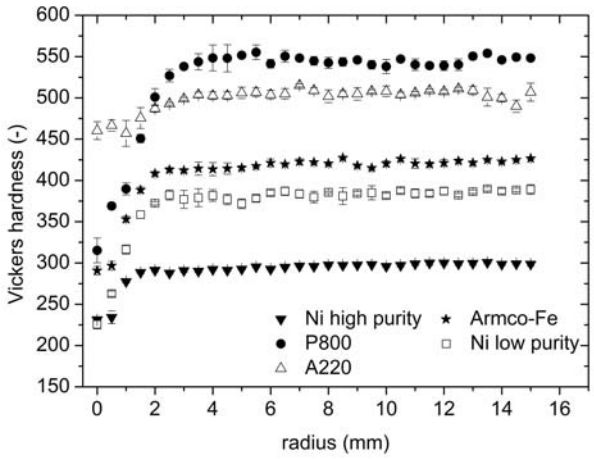

Figure 3.3 Comparison of the hardness distribution along the radius for different one phase metals showing a homogenous hardness after 10 rotations except near the center of the sample.

Regarding the typical geometry of the large deformed HPT discs the minimum v.Mises strain ϵ_{vM} of about 16 is reached at a radius of 2.5 mm. From this radius, also in the plot in Fig. 3.3 the onset of homogeneous hardness can be found.

3.1.2 HPT processed metals without steady state microstructures

In contrast to the features presented for the pure metals, homogeneity due to the presence of a minimum achievable grain size, the elongation of the grains and their inclination, the pearlitic steel, R 260, has to be treated separately. Starting from the hardness plots, see Figure 3.4, no saturation in hardness can be found.

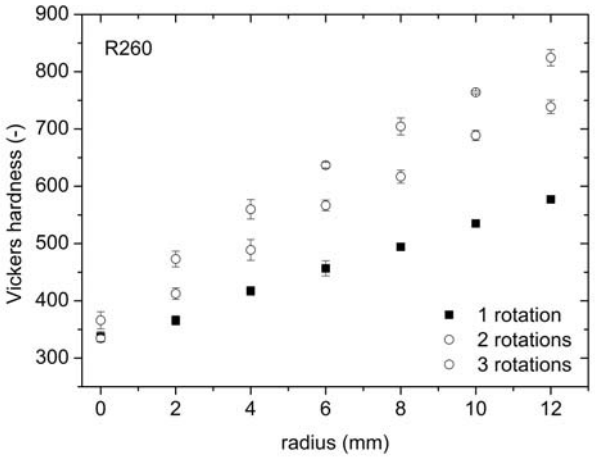

Figure 3.4 Hardness distribution along the radius for the pearlitic steel R260 having a hardness gradient within the disc as a function of different number of rotations.

The hardness increases linearly with the radius for different number of rotations. The reason for the ongoing increase of the hardness is that in the investigated deformation range, ϵ_{vM} is about 0-16, no saturation of refinement occurs. Only three full rotations could be applied. The reason for that is, that after three rotations at the very edge of the HPT disc a hardness comparable to the hardness of the HPT anvils is reached, which does not allow a further deformation without total damage of the anvils. Features of the microstructural fragmentation process should be shortly discussed as a next point.

In Figure 3.5a-d the evolution of the microstructure of the R 260 steel looking into the radial direction is presented. Former investigations of SPD deformed pearlitic steels via HPT were published in references [47, 48] and also presented in Paper D. In Figure 3.5a the undeformed pearlitic starting structure consisting of the cementite lamellae embedded in the ferritic matrix is shown. The lamellae are parallel within the pearlitic colonies, the lamella spacing is about 200 nm and appear black. With increasing strain the lamellae align into the shear direction, which is parallel to the horizontal direction of all micrographs and the lamella spacing is decreasing, see Figure 3.5b (in these micrographs the lamellae appear white). At higher strains, Figure 3.5c, the microstructure is almost fully aligned, in only some areas the pearlitic structure is still unaligned. At the highest strain investigated with the SEM, $\epsilon_{\mathrm{vM}}\sim$16 in Figure 3.5d, the entire pearlitic structure is aligned in the shear

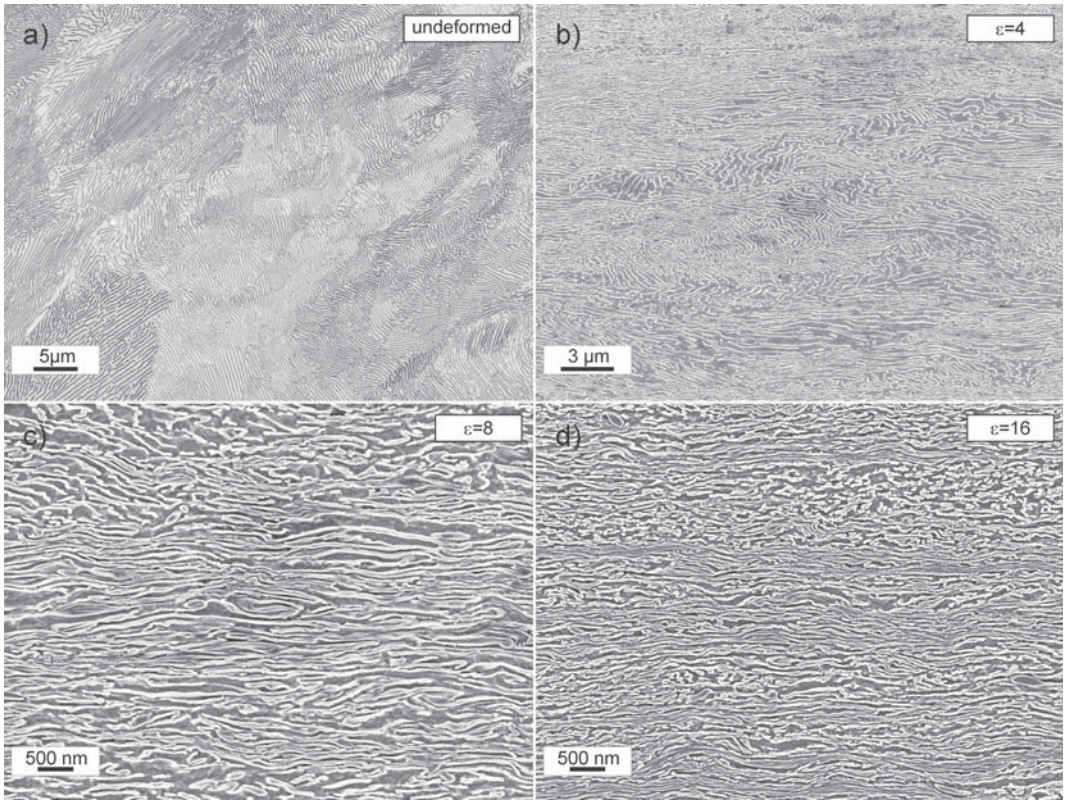

Figure 3.5 SEM-micrographs of the investigated material R260 taken at different equivalent strains (a-d) looking into the radial direction. (a) undeformed starting material, (b) ϵ_{vM}=4, (c) ϵ_{vM}=8, (d) ϵ_{vM}=16.

direction and the lamellar structure is partly broken up into individual carbides. In Figure 3.2c the lamellar structure in a TEM-micrograph is shown again, where the lamellar structure is still visible. The large increase in hardness (referring to the edge region after 3 rotations of more than 800 HV are measureable) can be attributed mainly to the strong decrease in the lamella spacing [49, 50] from about 200 nm to 10-15 nm after equvivalent strains ϵ_{vM} of about 16, which is more clearly visible in Figure 3.2c. Eventually it should be noted that no saturation of microstructural fragmentation only implies that it was not found in the investigated deformation range, which is given by technical circumstances. Also a one phase alloy having a theoretical minimum grain size with a hardness higher than the one of the anvils would not show a saturation in hardness. That means, the discrimination between microstructure showing either a steady state microstructure or not, is only based on a technical restriction.

3.2 Fracture toughness measurements

In the next part of the work the fracture toughness measurements will be discussed. In general, the results showed a pronounced influence of the crack plane orientation on the fracture toughness in Armco iron and the pearitic steel, R260. In Nickel the fracture toughness anisotropy was less pronounced. As an introduction the specimen orientations and the resulting specimen denominations, used throughout the work, will be presented. Afterwards the results of the different investigated materials will be summarized and underlined with fractographic investigations.

3.2.1 Specimens orientations

In Figure 3.6 a schematic of the HPT disc and the extracted fracture specimens can be found. The specimens are denominated as orientation A, B, C and D.

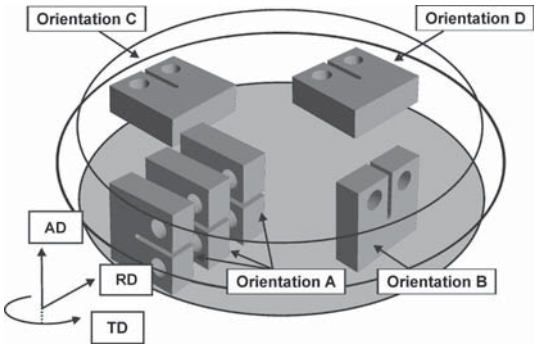

Figure 3.6 Schematic representation of the former HPT disc, the fracture specimens with their different denominations used in this work and the used coordinate system with an axial (AD), radial (RD) and tangential (TD) direction.

Specimens with Orientation A (also termed tangential orientation) have the tangential direction as the desired crack propagation direction. Orientation B (also termed axial orientation) has the axial direction and Orientation C (also termed radial orientation) the radial direction. The orientations are all in accordance to the used coordinate system, see Figure 3.6. The difference between Orientation A and C should be noted. The radial direction (Orientation C) here means the direction heading to the center of the disc, whereas for Orientation A the tangential direction means tangential to the circumference of the disc of a particular radius. Orientation D is a special case of Orientation C, where the specimens crack propagation direction is the tangential direction. As indicated for orientation A, the specimens could be extracted from different radii. As shown for metals with steady state microstructures, no difference in the mechanical fracture behavior should be found as long the specimens were taken from areas where a homogeneous hardness

was reached. This was also shown in Paper C. Since for the pearlitic steel R260 this feature could not be reached the specimens will have a gradient in hardness and degree of deformation through the entire specimen. This could be seen as a drawback but on the other hand it offers the possibility to measure the fracture toughness as a function of applied strain. Regarding Orientation A and B a strain gradient through the thickness is present. The specimens will be denoted with the average strain experienced by the deformation process. Specimens with orientation C have the same deformation strain through the thickness, but a gradient along the crack propagation direction. Since the plastic zones are small with respect to the change of the hardness within the plastic zone no strain gradient effects are expected to be present. Referring to orientation C, the crack propagation direction was heading to an increasing radius for Nickel and the steel samples, whereas for Armco iron the crack propagation direction was heading to a decreasing radius as also depicted in Figure 3.6.

Details to the principles of the measurements, the data acquisition and analyses can be found in the individual papers. Principally it was attempted to fulfill to general standards [51, 52] used for fracture toughness measurements as far as the miniaturization of the specimens allowed for it.

3.2.2 Fracture toughness of Armco iron

In Figure 3.7 the fracture toughness results for the different specimen orientations are presented. Every single data point is the average of three measurements and the error bar represents the standard deviation. The graph indicates that for Orientation

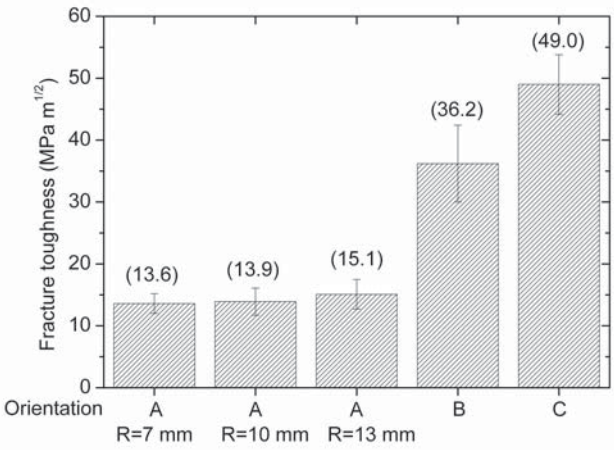

Figure 3.7 Comparison of the fracture toughness results of the different measured crack plane orientations.

A, measured for different radii (R=7,10 and 13 mm), where the specific radius was the middle of the specimen, no specific influence of the specimen position on the

fracture toughness was found. Additionally, some scatter is present, which will be explained in a later chapter. The most striking observation is the large differences of the fracture toughness at the different specimen orientations. Orientation A shows the lowest fracture toughness with an average fracture toughness of 14.2 MPa $m^{1/2}$, which was related to the intercrystalline crack path, see Figure 3.8a, exhibiting a low fracture work due to the observed grain boundary fracture. Such a fracture behavior for UFG iron was not reported so far, since the deformation and fracture behavior was exclusively characterized by tensile or compression tests [53, 54].

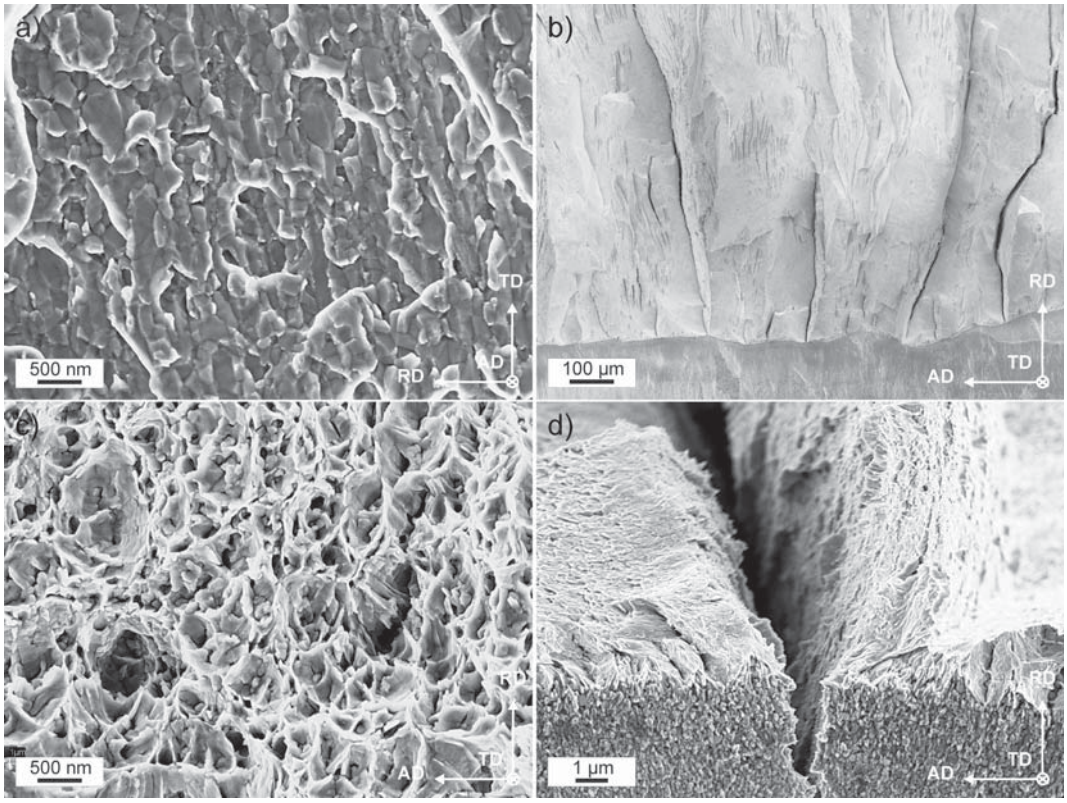

Figure 3.8 Detail and overview fractographs showing important fracture features of SPD-deformed Armco iron.

A pronounced increase in the fracture toughness of Orientation B was inferred from an occurring crack bifurcation almost perpendicular to the desired crack path, see also Paper C. Short kinked cracks exhibit a lower local driving force, which leads to a higher global fracture toughness. Due to the crack bifurcation the obtained value needs to be seen only as a lower bound for the real Mode-I fracture toughness [55]. The fracture surface exhibits the same features as those found for specimens with Orientation A. This is because the kinked crack runs into the same direction as the same specimen would be oriented in Orientation A. The reason of the crack bifurcation was explained by the low fracture toughness of orientation A and the elongated grain structure perpendicular to the required crack propagation direction,

which additionally hinders the crack propagation.

Orientation C showed the highest fracture toughness, which could be explained by a well known toughening mechanism, which can be found in classical textbooks, see e.g. [56] and is also under discussion in other publications regarding the impact toughness of UGF metals [57, 58] but also in reports dealing for instance with Al-alloys [59] or classical coarser structured steels [60]. This toughening mechanism is working by dividing the actual fracture surface into smaller ligaments during the fracture process, called delaminations, see Figure 3.8b. This configuration with reference to laminate structures is also called the crack divider orientation. These internal free surfaces cause naturally a reduction of the in-plane stress component. So the stress triaxiality ahead of the crack tip and the driving force for the crack propagation is reduced. Additionally, the ligaments between these naturally formed internal surfaces can deform stronger, which leads to local ductile fracture as shown in Figure 3.8c and also found for tensile tests, see Paper C. An important aspect regarding this toughening mechanism is the origin of these internal surfaces. In literature the occurrence of the delaminations are referred to either an alignment of particles and inclusions during a rolling process or due to textural aspects. In this work the origin of the delaminations can be presumably related to the existence of the low fracture toughness in orientation A. This circumstance is presented in Figure 3.8d again. Here the transition of the fatigue pre-crack to the overload fracture surface is shown. In the lower part of the micrograph, the fatigue fracture surface with a granular structure, in which the delamination initiates, is visible. In the upper part the delamination is present. A comparison of the coordinate systems in Figure 3.8a and d implies that for both testing directions the axial direction (AD) is the crack opening direction. As the fracture toughness of Orientation A is very low and Figure 3.8d illustrates that the delamination initiates in the granular structure along the grain boundaries of the fatigue-pre-crack, the origin of the delaminations can be seen in the low fracture toughness of Orientation A. In other words, the high fracture toughness of Orientation C is a result of the low fracture toughness of Orientation A. As the intercrystalline fracture strongly promotes the mechanical anisotropy of the fracture toughness of iron the possible reasons for this crack path will be discussed in a later section.

Additionally the intercrystalline crack path is connected with a change in the ductile to brittle transition behavior of iron. Classically a change from transcrystalline fracture in the low temperature regime to ductile fracture above the ductile to brittle transition is expected with a large increase in fracture toughness. On the contrary the SPD microstructure promotes intercrystalline fracture in the low temperature regime with only a weak increase in fracture toughness compared with coarse-grained iron in the same temperature range. Further details to these findings are given in Paper E.

3.2.3 Pearlitic steel R260

The measurements of the steel were performed with respect to different crack propagation directions and as a function of different degrees of pre-deformation, see Figure 3.9. For the low deformation regime, up to equivalent strains of 2, data points from reference [9] are incorporated stemming from ECAP deformed material. Fractogrphic results supporting the results can be found in Paper D.
Focusing on Orientation A it was found that with increasing pre-deformation the fracture toughness strongly decreases from a starting value of about 50 MPa $m^{1/2}$ down to values of about 4 MPa $m^{1/2}$ after ϵ_{vM}=17. The reasons for this behavior is classically a consequence of the strong increase in the hardness as shown in the section before. Simultaneously the crack resistance decreases with increasing pre-deformation due to the increasing alignment of the lamellae parallel to the crack propagation direction.

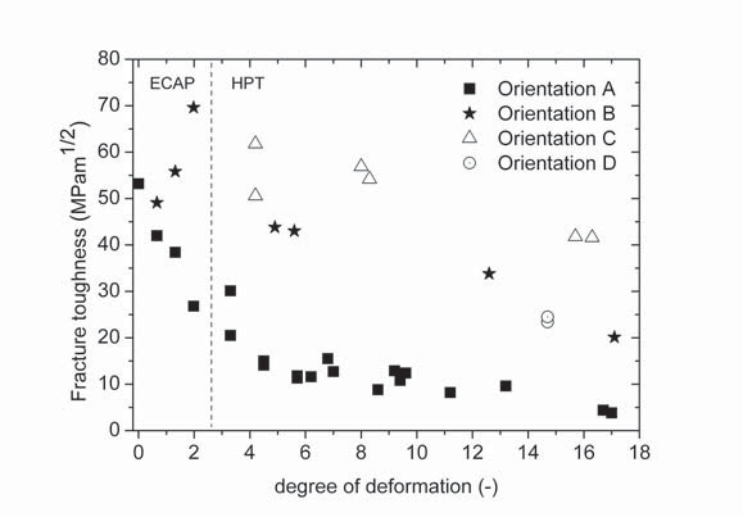

Figure 3.9 Fracture toughness results as a function of pre-deformation and for different crack plane orientations.

However for Orientation B an increase of the fracture toughness was measured in the low deformation range. In this Orientation the lamellae become aligned perpendicular to the desired crack propagation direction during ongoing deformation. The increase of the fracture toughness was inferred from crack branching ahead of the crack tip, which decreases the driving force for crack propagation. After equivalent strains of ϵ_{vM}=2 a decrease in fracture toughness occurred. Here the global crack deviated from its desired crack propagation, similarly reported for Armco iron in the previous section, into the direction of lower fracture toughness, Orientation A. The large crack resistance due to the alignment perpendicular to the crack propagation inhibits the crack propagation.

Orientation C shows in the measured deformation interval an ongoing drop in the fracture toughness. Despite this at the highest pre-deformation the fracture tough-

ness is about 10 times higher than for Orientation C. The toughening mechanism, namely delamination induced toughening is the same as explained for the iron. In contrast to iron, where the direction of lowest fracture toughness was caused by the intercrystalline crack path, the occurrence of the delaminations here is a result of the low toughness of the iron/cementite interface, which seems to be the preferential crack path for Orientation A at high pre-strains.

Finally also attempts for measuring the fracture toughness for Orientation D were made, where the focus of interest was only the highest possible pre-deformed state. Due to geometrical reasons, only measurements at a strain of about 15 could be performed. The result in Figure 3.9 show a marked decrease in the fracture toughness even though the pre-deformation was more or less the same. Fractographic studies were performed to investigate this unexpected drop in fracture toughness.

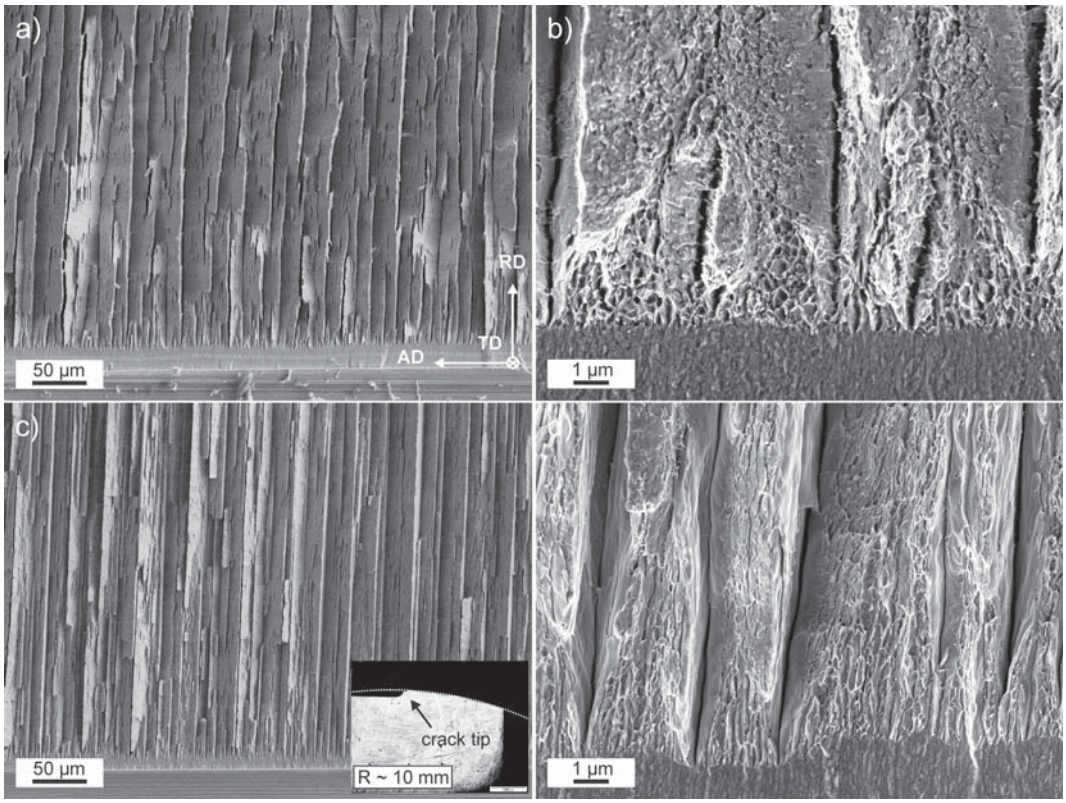

Figure 3.10 Fractographs comparing orientation C (a,b) and orientation D (c,d) at the same magnifications

In Figure 3.10a and b Orientation C is compared with Orientation D (Figure 3.10c and d) with fractographs taken at the same magnifications, respectively. With increasing pre-deformation the distance of the lamellae seems to decrease. At low magnifications, Figure 3.10a and c, a lower distance between the delaminations for Orientation D seems to be present and they look generally straighter. As paper D showed, with decreasing distance of the delaminations the fracture toughness de-

creases and so a drop can be expected. At high magnifications (Figure 3.10b and d) the remaining ligaments between the delaminations are better visible. A larger distance between them consumes more shear work for their separation and also a stronger necking is possible. Both factors, shear work and the necking, increase the fracture work and toughness. Therefore Orientation D exhibits a lower fracture toughness. The reason for the apparent smaller distance is not clear yet. Possibly it is due to compressive residual stresses in the circumferential direction of the HPT disc. Measurements of residual stresses were not performed, however an additional hint in favor of this assumption is given by the fracture specimen itself, see inset picture in Figure 3.10c. Here a half of a specimen after fracture is shown. The crack propagation direction is implied by the bent dotted line. The crack propagated along a curve and its radius is about 10 mm, which is almost exactly the position of the radius of the crack tip with respect to the former position in the HPT disc.

3.2.4 Nickel

For the results of Nickel no publication has been prepared and so some experimental details need to be mentioned. Specimens were extracted for the three major specimen orientations A, B and C. For convenience the specimen size varies between Orientation A, B and C. Specimens with Orientation C have a width, W, of 10 mm and a thickness, B, of 5 mm, whereas specimens with orientation A and B had only a width, W, of 5.2 mm and a thickness, B, of 2.6 mm. The fracture toughness was assessed by J-Integral measurements and a multiple specimen test procedure was applied. The motivation for this experimental study was to obtain a comparison with the bcc SPD-iron. The blunting line was determined in accordance to the equation:

$$J = M\sigma_{\mathrm{y}}\Delta a. \tag{3.1}$$

The pre-factor M was taken as 2. As an approximation σ_{y} was taken as a third of the hardness (380 HV):

$$\sigma_{\mathrm{y}} = \frac{H}{3}, \tag{3.2}$$

therefore a value of σ_{y}=1260 MPa was taken. In Figure 3.11 the obtained data points are shown as a function of the crack extension measured in the SEM.

A linear fit of the 3 data points was made in order to obtain the intersection point with the blunting line. As the graph shows for Orientations A and C the values for $J_{0.2,\mathrm{Bl}}$ are almost the same with a value of 96.5 KJ/m^2 for Orientation A and 99.8 KJ/m^2 for Orientation C. However, it should be noted that these numbers represent values that already contain a distinctive stable crack growth similar to the yield stress $R_{\mathrm{P0.2}}$ and accounts for a non-proportional displacement of 0.2 percent. In contrast to the $J_{0.2,\mathrm{Bl}}$ the fracture toughness value K_{IC} resembles the maximum stress intensity without crack propagation. In order to express this consideration

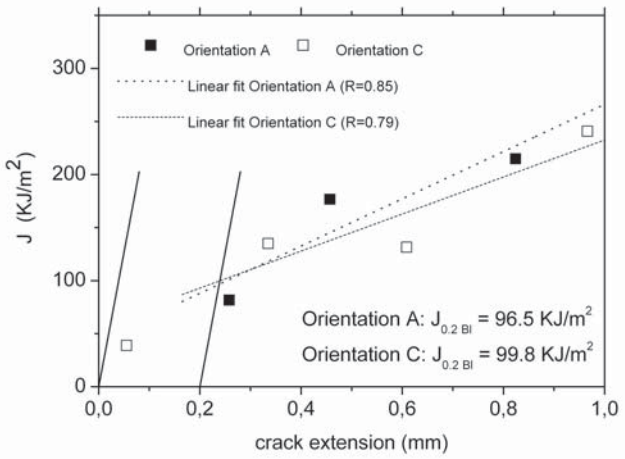

Figure 3.11 J-Δa plot for Nickel for Orientation A and C

.

with a measurement another point in the graph is depicted with a J-Integral value of 38.9 KJ/m^2 but only with a crack extension of about 55 μm, which would normally be excluded according to the ASTM standard [52]. Also, a comparison of fractographs representing typical fracture features for Orientation A and C do not show large differences.

In Figure 3.12a an overview fractograph, representing Orientation C, is presented showing ductile fracture with voids typically initiated by remaining inclusions. Beside these voids a second type of void can be found with typical diameters in the range of less than 1 μm, however larger than the grain size. As 3.12b shows in these small voids individual grains and grain boundaries between them can be distinguished. This leads to the assumption that these voids are caused by the grain structure itself and initiated at grain boundary triple junctions as also reported in [61] analyzed with in-situ TEM observations. Similar features of the fracture surface were also found for Orientation A, see 3.13a and b. A notable difference for Orientation A is a large dimple field in the lower part of the figure, whereas for Orientation C a clear separation between fatigue pre-crack and overload fracture area can be seen.

Although J-Integral values $J_{0.2,\mathrm{Bl}}$ for Orientation A and C were fairly similar the same behavior cannot be assumed for Orientation B. Here the crack was deviating almost perpendicular to the expected crack propagation direction. This is also shown in Figure 3.14. Thus it was almost impossible to measure a Mode-I crack propagation and the individual J-values could not be associated with a crack extension caused by Mode-I crack propagation.

In order to give at least an estimate for the fracture toughness of this specimen orientation, the stretched zone width (SZW) was measured. Table 3.2 represents the

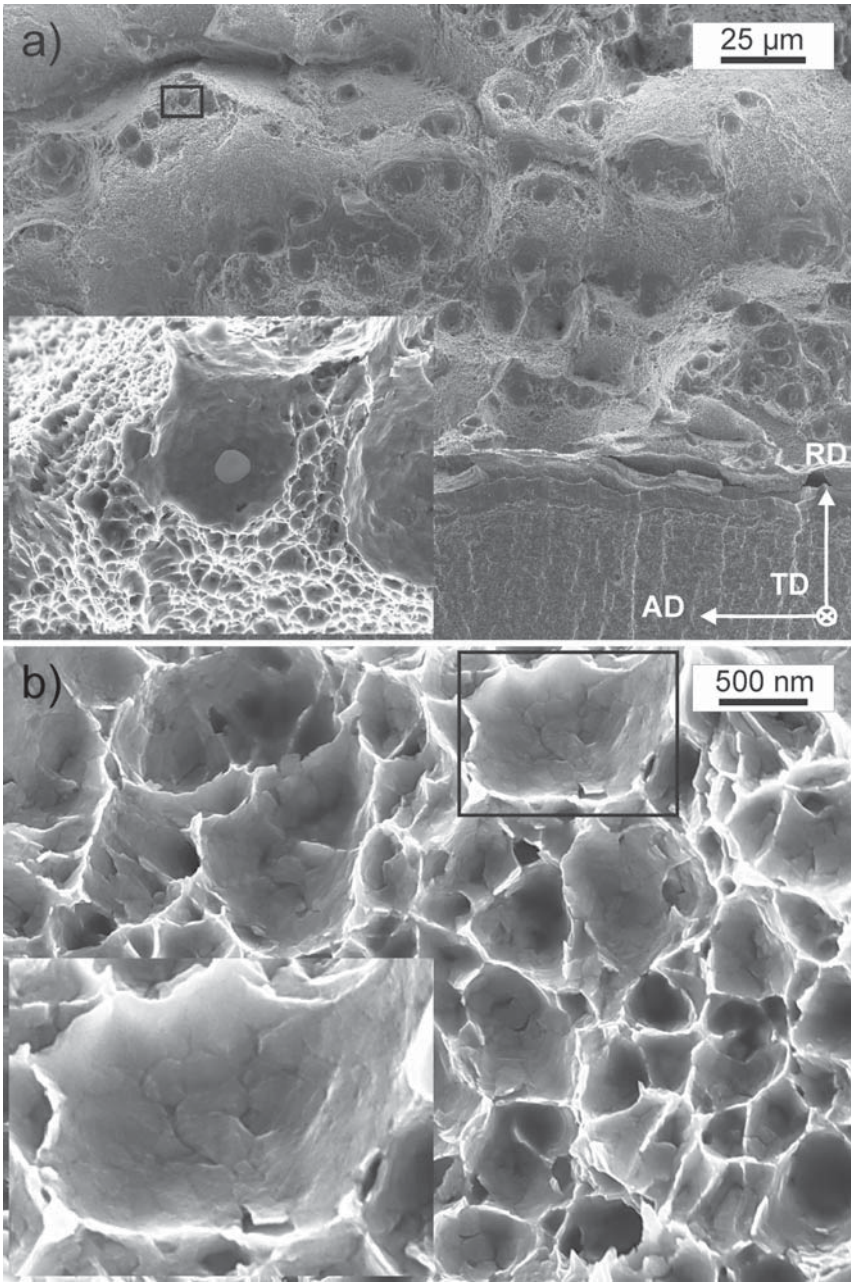

Figure 3.12 Fractographs representing Orientation C of SPD nickel. (a) Overview picture showing ductile fracture and typical voids initiated by inclusions (inset-picture). (b) Microvoids revealing individual grains in their interior.

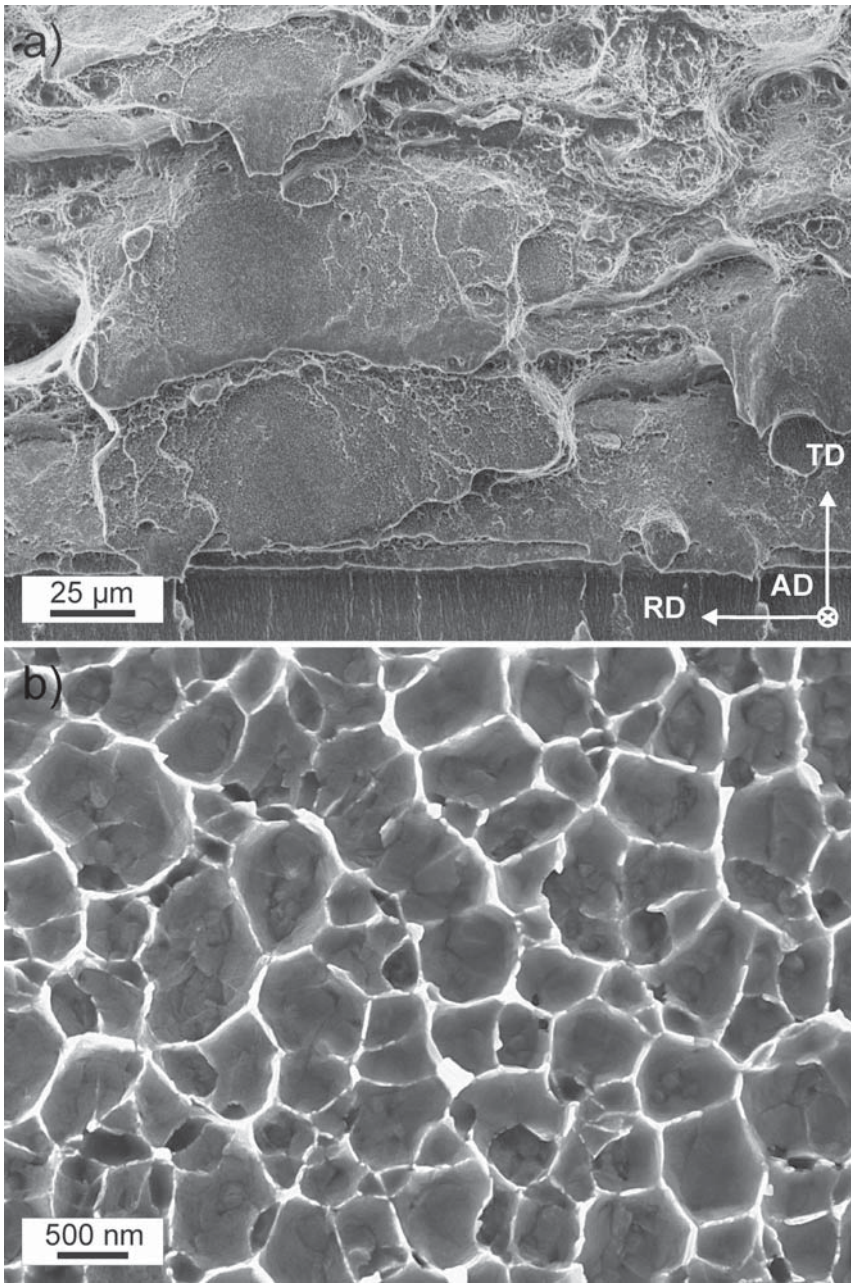

Figure 3.13 Fractographs representing Orientation A of SPD nickel. (a) Overview picture showing ductile fracture. (b) Microvoids initiated at grain boundaries.

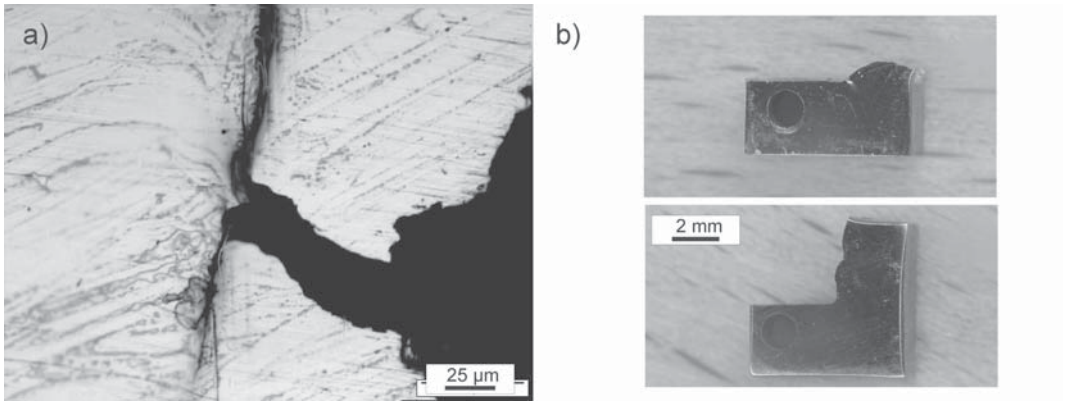

Figure 3.14 Observed crack paths in nickel. (a) Micrograph showing the strong crack deviation for Orientation B. (b) Comparison of two fracture specimens with Orientation A (upper picture) and Orientation B (lower picture).

measurements of the SZW_{C}, which were performed in the middle of the specimen with the largest crack extension, respectively. At least three measurements were performed per data point. The table shows that for Orientation B the stretched zone width shows a significant increase with regard to Orientation A and C, where the J-Integral measurements exhibit similar values. However, it must also admitted that in case of Orientation B a strong shear zone evolves at the crack tip, see also Figure 3.14, which might have not the same physical significance as the stretched zone considering a pure Mode I crack propagation.

Table 3.2 Stretched zone width measurement results.

Orientation	$SZW_{\mathbf{C}}$ [μm]
Orientation A	17.6
Orientation B	38.8
Orientation C	17.5

Despite this, Nickel has a pronounced fracture anisotropy, since as Figure 3.14b shows, the global crack paths of Orientation A and B differ significantly. In Orientation B the crack propagates almost perpendicular to the expected crack propagation direction (Figure 3.14a). The crack deflection is caused again by the aligned and elongated microstructure as already found for iron. However, in comparison with iron no intercrystalline crack path evolves and fracture is dominated by microvoid formation. Fracture features are not shown again because they are almost identical with Orientation A. Regardless, the microvoids have a preferential growing direction due to the mixed mode loading. The anisotropy between Orientation A and B may be induced by the typical shear texture found in HPT processed nickel [24].

3.2.5 Comparison of the fracture behavior

In the following a compilation of data presented in the sections before is given. In order to make the results more clear some examples of coarse grained iron and nickel found in the literature are added [62, 63]. Some of the data is missing, see stretched zone width and J-Integral, but is not significant. The intention was to have a value for the fracture toughness measured in terms of K and critical crack openening displacement (CTOD) for all different microstructural states. Following relations were used in order to recalculate needed values and were taken from a common textbook [64]. An estimate for the CTOD was derived from

$$CTOD = m\frac{K^2}{\sigma_{\mathrm{y}}E} \tag{3.3}$$

where K is the fracture toughness, m is about 0.5 for plane strain conditions and E is the Young's Modulus with 210 GPa for iron and 200 GPa for nickel. The yield strength σ_{y} for iron is 1400 MPa and for nickel 1260 MPa. The yield stresses of the other material states can be found in the papers of Srinivas [62, 63].

An estimate for the J_{IC} for SPD nickel with Orientation B was obtained from measuring the critical stretched zone width SZW_{C}

$$J_{\mathrm{IC}} \approx 4\sigma_{\mathrm{yt}}SZW_{\mathrm{C}} \tag{3.4}$$

where σ_{yt} is the average value of the yield and the ultimate tensile strength. The tensile strength σ_{UTS} is 1400 MPa measured in a tensile test. σ_{yt} was calculated to be 1330 MPa.

The fracture toughness in terms of K derived from J-measurements was calculated with

$$K_{\mathrm{IC}} = \sqrt{\frac{JE}{(1-\nu^2)}}. \tag{3.5}$$

A Poisson ratio of 0.3 was taken.

Intercrystalline fracture of iron

One striking result shown in Table 3.3, is the low fracture toughness of iron with Orientation A. The value of around 14 MPa $\mathrm{m}^{1/2}$ is fairly low in comparison to the fracture toughness of coarse grained iron. However, in comparison with the Griffith toughness, which is around 1 MPa $\mathrm{m}^{1/2}$ [65] plasticity must be present during the fracture process in this specific specimen orientation. Additional contributions enhancing the fracture toughness were enumerated in Paper C: The fracture surface possesses steps and ledges which need to be sheared off to fracture entirely. Also, nanovoids ahead of the crack tip which may form would increase the toughness and the plastic deformation of the individual grains.

The reason for the occurrence of intercrystalline fracture cannot be explained entirely. Intergranular fracture is often associated with a certain type of grain boundary embrittlement, where sulphur and phosphor are well known examples in connection with steels leading to a pronounced grain boundary embrittlement. However, this assumption cannot be used here due to experiments disproving its validity. In paper E heat-treatments are described to increase the grain size of SPD-deformed iron. Since at room temperature the coarse grained structures failed by ductile fracture embrittlment of SPD iron has to be excluded. In a case of an embrittlment the impurities would be dragged along the grain boundary. Because of the grain coarsening the amount of impurities at the grain boundary should increase as the fraction of grain boundary decreases.

Table 3.3 Fracture toughness comparison of iron and nickel for different microstructural states and orientations. For clarity, values taken from literature are in bold type, calculated values are italic and measured values are in plane type.

	K_{IC} [MPa $m^{1/2}$]	J_{IC} [kJ/m^2]	CTOD [μm]	SZW [μm]	σ_{Uts} [MPa]	K.σ_{Uts} [(MPa)^2 $m^{1/2}$]
Fe-SPD O-A	14.2±1.9	-	*0.34*	-	1616±12	*22947*
Fe-SPD O-B	36.2±6.2	-	*2.23*	-	1616±12	*58499*
Fe-SPD O-C	49.0±4.8	-	*4.08*	-	1616±12	*79184*
Fe-38 μm	**202.0**	-	*467.1*	**210**	**299**	*60398*
Fe-420 μm	**142.0**	-	*317.9*	**110**	**271**	*38482*
Ni-SPD O-A	*145.6*	96.5	*42.1*	17.6	1400	*203855*
Ni-SPD O-B	*213.0*	*206.4*	*90.0*	38.8	1400	*298191*
Ni-SPD O-C	*148.1*	99.8	*43.5*	17.5	1400	*207342*
Ni - 95 μm	*222.4*	**225.0**	*718.8*	**228**	**341**	*75830*

Another aspect weakening the assumption of grain boundary embrittlement is found by the influence of the testing temperature. An increase in the testing temperature of SPD iron leads to an increase in fracture toughness and dimple formation was also observed at high testing temperatures. (see Paper E). This feature implies that for SPD iron, similar to coarse grained iron, a ductile to brittle transition is present [66]. Compared to the classical transition, in this work intercrystalline fracture occurs in contrast to transcrystalline cleavage fracture in the lower shelf region. Therefore, the large scatter of the fracture data becomes clearer, which is often observed in the transition zone from brittle to fully ductile behavior. The increase in fracture toughness is caused by the decrease in the yield strength which seems to promote the ductile fracture. Additionally, a simple fracture test with an iron sample with a purity of 99.99 % was conducted, which again exhibited intercrystalline fracture.

The assumption, which was made to prevent grain boundary fracture, was to test a bcc alloy with a high amount of alloying elements. It was assumed that the strong alloying could enhance the grain boundary toughness and initiate dimple

fracture. The tested material was denominated as P 800 and is usually used for magnetic applications. The main alloying component is Co, further details on the microstructure and magnetic properties can be found in [67]. Testing Orientation A gave a fracture toughness of 4.1 MPa $m^{1/2}$ and Orientation C a fracture toughness of 32 MPa $m^{1/2}$. Again, intercrystalline fracture occurs, see Figure 3.15b. The fracture toughness is even lower due to the higher hardness of the material, see section *HPT processed metals with steady state microstructures*. However, for Orientation C a quite moderate fracture toughness due to delamination induced toughening, demonstrated in Figure 3.15a, was found.

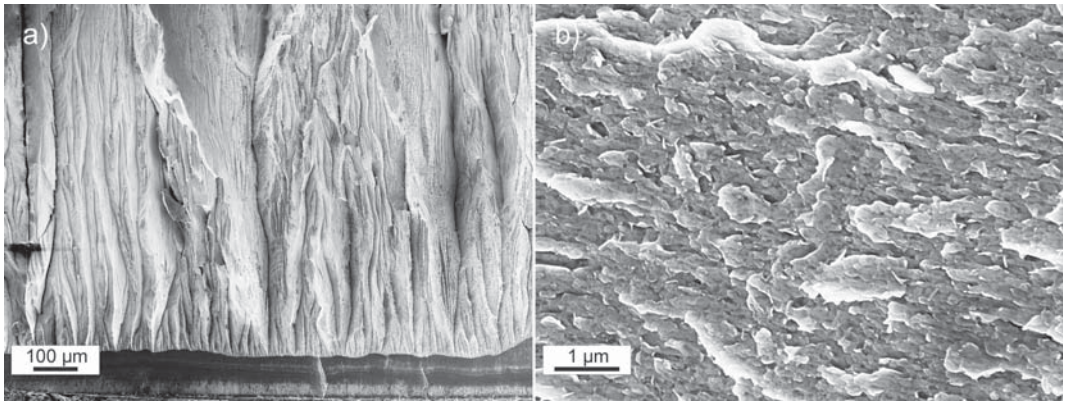

Figure 3.15 Fractographs of P800. (a) Delaminations in Orientation C. (b) Intercrystalline fracture in Orientation A.

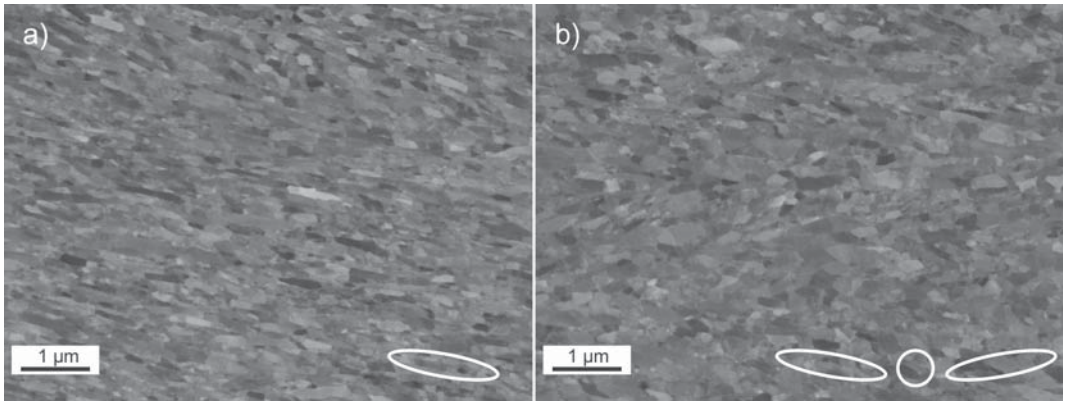

Figure 3.16 Microstructural comparison of different deformation routes: (a) Route A. (b) Route C.

Another attempt to shed more light on the intercrystalline crack path is described in Paper C. By changing the deformation path during HPT a modification of the grain structure could be achieved. Further details are given in [68], additionally in Figure 3.16 the difference in the microstructure is shown. For monotonic deformation, called route A, Figure 3.16a, the microstructure is strongly aligned with

elongated grains. By changing the deformation path, called Route C (see Paper C for further details), equiaxed grains and grains having an alignment in the opposite direction can be found (Figure 3.16b). The mixture of elongated and equiaxed grains lead to a stronger blunting of the crack tip and to a higher toughness, even though the hardness remains more or less the same. This shows that the grain shape, its aspect ratio and the alignment of the microstructure are significant factors for the observed crack path.

The experimental facts mentioned so far should indicate that the occurrence of the the intercrystalline crack path seems to be an intrinsic property of SPD bcc iron. Also in literature a similar behavior for nanocrystalline bcc crystals can be found, see references [69–72]. Here under certain conditions, regarding temperature and strain rate, an intercrystalline crack path was found. The fracture mechanism can be shortly described as the formation of nanovoids ahead of the crack tip which coalesce with the main crack along the grain boundaries. However, due to calculation time, these simulations are mostly restricted to grain sizes in the range of 10 nm and therefore approximately by a factor of 10 smaller as in the present case. Despite this, the proposed mechanisms could be also a possible explanation in the present case.

Although the fracture toughness is low for Orientation A a remarkable increase for Orientation B and C was found and explained in the previous sections. It must be admitted that an increase in strength, as done here with SPD, generally leads to a deterioration of the fracture behavior. For that reason it is often very useful to look into fracture behavior from a more objective point, which means to also look simultaneously on the strength of the material. In Table 3.3 also the product of strength and fracture toughness can be found. Regarding this product the SPD states, especially Orientation B and C, exhibit a remarkable performance compared to the coarse grained iron examples.

Ductile fracture of Nickel

Table 3.3 shows also the results for nickel. In comparison with iron a much larger fracture toughness was found. The fractographs showed ductile fracture. Regarding the anisotropy for Orientation B a crack deflection was found into the direction of the aligned microstructure. For Orientation C no delaminations occurred because of the high toughness of Orientation A. Therefore the fracture toughness was more or less the same. Looking onto the product of strength and toughness an exceptional improvement compared to the coarse grained example was found. The key factor for the large fracture toughness compared to the results of iron must be the difference in the crystal lattice and the connected differences in the deformation behavior at these small grain sizes. In the dimples still grain boundaries and individual grains were found. This shows that the deformation behavior is comparable to the one of bcc iron but a stronger local deformation may allow for a dimple formation. A similarity regarding the difference in the deformation behavior can be inferred from tensile tests exhibiting a different stress state. Ultrafine-grained bcc-metals tend

rather to fail through deformation concentration in a shear band [73] whereas fcc metals allow larger uniform deformation and fail through classical necking, which increases the fracture work dramatically.

4 Conclusions

In this thesis the effect of Severe Plastic Deformation (SPD) on the fracture behavior of different metals was investigated. Main focus was to investigate the model materials of pure iron and nickel, along with a classical pearlitic steel. The samples were deformed by the high pressure torsion (HPT) process, a rather simple and effective technique to impose very large plastic strains onto a metal. Afterwards fracture toughness experiments with respect to different crack plane orientations were conducted.

SPD of pure one phase metals leads to elongated grains with average grain sizes of some hundred nanometers after reaching the saturation regime of grain refinement. The pearlitic steel exhibits in the investigated deformation range an ongoing decrease in the lamella distance connected with a pronounced alignment of the lamellae into the shear-direction in the entire specimen.

In both materials, the resulting fracture properties are markedly controlled by the SPD deformation process. Although the investigated bcc metal and alloy, Armco iron and the pearlitic steel, posses different microstructures, both exhibit a very similar influence of the specimen orientation on the fracture toughness ranging from ductile to brittle fracture after SPD deformation. The mechanical anisotropy can be related to one testing direction with a fairly diminished fracture toughness. Fractographic studies in iron revealed intercrystalline fracture along the elongated grains responsible for an average toughness of only 14.2 MPa $m^{1/2}$, a value lower than the fracture toughness of coarse grained iron below the ductile to brittle transition. In the case of the pearlitic steel the direction of lowest fracture toughness exhibited brittle fracture along the severely deformed and aligned microstructure resulting in an average toughness of 4 MPa $m^{1/2}$ after strong pre-deformation by HPT. The direction of relative low fracture toughness promoted an exceptional enhancement in toughness in the other testing directions. The extrinsic toughening mechanisms

were identified to be crack deflection and delamination induced toughening. An enhancement in the toughness by a factor of 3 regarding iron and a factor of even 10 in the pearlitic steel after the strongest pre-deformation, both with respect to the crack plane orientation of highest toughness, was found.

In contrast to the bcc examples pure nickel showed a less pronounced anisotropy of the fracture toughness and simultaneously a good combination of fracture toughness and strength. In two testing directions an isotropic fracture behavior was found, whereas the third testing direction exhibited a crack deflection mainly caused by the aligned microstructure and texture. The large fracture toughness and the less pronounced anisotropy are a result of ductile fracture type compared to the brittle intergranular fracture of bcc iron.

This work clarified that fracture toughness enhancement in SPD processed metals may have extrinsic causes, such as an aligned deformation structure, and cannot simply be referred to a reduction in grain size focusing on bcc metals. Therefore fracture toughness measurements need to be conducted in all major crack propagation directions to obtain a full picture of the effect of grain refinement on this material property in SPD processed materials.

Bibliography

[1] R.Z. Valiev, R.K. Islamgaliev, I.V. Alexandrov, Prog. Mat. Sci. 45 (2000) 103-189.

[2] R.Z. Valiev, T.G. Langdon, Prog. Mat. Sci. 51 (2006) 881-981.

[3] A.P. Zhilyaev, T.G. Langdon, Prog. Mat. Sci. 53 (2008) 893-979.

[4] C.C. Koch, Scripta Mater. 49 (2003) 657-662.

[5] Y. Wang, M. Chen, F. Zhou, E. Ma, Nature 419 (2002) 912-915.

[6] I. Sabirov, Y. Estrin, M.R. Barnett, I. Timokhina, P.D. Hodgson, Acta Mater. 56 (2008) 2223-2230.

[7] I. Sabirov, O. Kolednik, R.Z. Valiev, R. Pippan, Acta Mater. 53 (2005) 4919-4930.

[8] M. Faleschini, H. Kreuzer, D. Kiener, R. Pippan, J. Nuclear Mater. 367-370 (2007) 800-805.

[9] F. Wetscher, R. Stock, R. Pippan, Mater. Sci. Eng. A 445-446 (2007) 237-243.

[10] A. Hohenwarter, R. Pippan, *Proceedings of the Hael Mughrabi Honorary Symposium at 2008 TMS Annual Meeting, Warrendale, 183-188.*

[11] W. Lojkowski, M. Djahanbakhsh, G. Bürkle, S. Gierlotka, W. Zielinski and H.-J. Fecht, Mater. Sci. Eng. A 303 (2001) 197-208.

[12] J.W. Ringsberg, M. Loo-Morrey, B.L. Josefson, A. Kapoor and J.H. Beynon, Inter. J. Fatigue 22 (2000) 205-215.

[13] R.Z. Valiev, I.V. Alexandrov, Y.T. Zhu, T.C. Lowe, J. Mater. Res. 17 (2002) 5-8.

[14] M.A. Meyers, A. Mishra, D.J. Benson, Prog. Mater. Sci. 51 (2006) 427-556.

[15] M. Furukawa, Z. Horita, M. Nemoto, T.G. Langdon, Mater. Sci. Eng. A 324 (2002) 82-89.

[16] H.W. Höppel, M. Kautz, C. Xu, M. Murashkin, T.G. Langdon, R.Z. Valiev, H. Mughrabi, Int. J. Fatigue 28 (2006) 1001-1010.

[17] H. Mughrabi, H.W. Höppel, Int. J. Fatigue (2009) *Article in press.*

[18] S. Wurster, R. Pippan, Scripta Mater. 60 (2009) 1083-1087.

[19] G. Herzer, Scripta Metall. Mater. 33 (1995) 1741-1756.

[20] Y.T. Zhu, T.C. Lowe, T.G. Langdon, Scripta Mater. 51 (2004) 825-830.

[21] R.Z. Valiev, Y. Estrin, Z. Horita, T.G. Langdon, M.J. Zehetbauer, Y.T. Zhu, JOM 58(4) (2006), 33-39.

[22] T. Hebesberger, H.P. Stüwe, A. Vorhauer, F. Wetscher, R. Pippan, Acta Mater. 53 (2005) 393-402.

[23] R.B. Figueiredo, T.G. Langdon, Int. J. Mat. Res. (Formerly Z. Metallkunde) 100 (2009) 1638-1646.

[24] M. Hafok, R. Pippan, Phil. Mag. 88 No.12 (2008) 1857-1877.

[25] J.T. Wang, Mater. Sci. Forum 503-504 (2006) 363-370.

[26] Y. Saito, H. Utsunomiya, N. Tsuji, T. Sakai, Acta Mater. 47 (1999) 579-583.

[27] V.M. Segal, Mater. Sci. Eng. A 197 (1995) 157-164.

[28] P.W. Bridgman, J. Apll. Phys. 14 (1943) 273-283.

[29] Q. Wei, H.T. Zhang, B.E. Schuster, K.T. Ramesh, R.Z. Valiev, L.J. Kecskes, R.J. Dowding, L. Magness, K. Cho, Acta Mater. 54 (2006) 4079-4089.

[30] C. Rentenberger, T. Waitz, H.P. Karnthaler, Mater. Sci. Eng. A 462 (2007) 283-288.

[31] H. Utsunomiya, K. Hatsuda, T. Sakai, Y. Saito, Mater. Sci. Eng. A 372 (2004) 199-206.

[32] J.C. Lee, H.K. Seok, J.Y. Suh, Acta Mater. 50 (2002) 4005-4019.

[33] G.J. Raab, R.Z. Valiev, T.C. Lowe, Y.T. Zhu, Mater. Sci. Eng. A 382 (2004) 30-34.

[34] K. Edalati, Z. Horita, J. Mater. Sci. (2010) *Article in press.*

[35] S. Mizunuma, Mater. Sci. Forum 503-504 (2006) 185-190.

[36] R.Pippan, S, Scheriau, A. Hohenwarter, M. Hafok, Mater. Sci. Forum 584-586 (2008) 16-21.

[37] M. Hafok, R. Pippan, Scripta Mater. 56 (2007) 757-760.

[38] A. Vorhauer, S. Kleber, R. Pippan, Mater. Sci. Eng. A 410-411 (2005) 281-284.

[39] A. Bachmaier, A. Hohenwarter, R. Pippan, Scripta Mater. 61 (2009) 1016-1019.

[40] A. Bachmaier, M. Hafok, R. Pippan, Mater. Trans. 51 (2010) 8-13.

[41] F. Wetscher, A. Vorhauer, R. Pippan, Mater. Sci. Eng. A 410-411 (2005) 213-216.

[42] M.J. Zehetbauer, H.P. Stüwe, A. Vorhauer, E. Schafler, J. Kohout, Adv. Eng. Mater. 5 (2003) 330-337.

[43] A. Vorhauer, R. Pippan, Metall. Mater. Trans. A 39 (2008) 417-429.

[44] M.S. Ryszkowska, T. Wejrzanowski, Z. Pakiela, K.J. Kurzydlowski, Mater. Sci. Eng. A 369 (2004) 151-156.

[45] A. Vorhauer, R. Pippan, Scripta Mater. 51 (2004) 921-925.

[46] C. Xu, Z. Horita, T.G. Langdon, Acta Mater. 56 (2008) 5168-5176.

[47] F. Wetscher, A. Vorhauer, R. Stock, R. Pippan, Mater. Sci. Eng. A 387-389 (2004) 809-816.

[48] Y. Ivanisenko, W. Lojkowski, R.Z. Valiev, H.J. Fecht, Acta Mater. 51 (2003) 5555-5570.

[49] J.D. Emburry, R.M. Fisher, Acta Met. 14 (1966) 147-159.

[50] G. Langford, Met. Trans. A 8 (1977) 861-875.

[51] ASTM E399, Annual Book of ASTM Standards, 1990

[52] ASTM E1820, Annual Book of ASTM Standards, 2008

[53] A.V. Panin, A.A. Panina, Y.F. Ivanov, Mater. Sci. Eng. A 486 (2008) 267-272.

[54] D. Jia, K.T. Ramesh, E. Ma, Acta Mater. 51 (2003) 3495-3509.

[55] R. Pippan, Eng. Frac. Mech. 44 (1993) 821-829.

[56] R.W. Hertzberg: *Deformation and Fracture Mechanics of Engineering Materials*, 4^{th} edition, John Wiley and Sons Inc., New York, 1996.

[57] R. Song, D. Ponge, D. Raabe, Acta Mater. 53 (2005) 4881-4892.

[58] T. Inoue, F. Yin, Y. Kimura, K. Tsuzaki, S. Ochiai, Metall. Mater. Trans. A 41 (2010) 341-355.

[59] S. Kalyanam, A.J. Beaudoin, R.H. Dodds, F. Barlat, Eng. Frac. Mech. 76 (2009) 2174-2191.

[60] W. Guo, H. Dong, M. Lu, X. Zhao, Int. J. Press. Vess. Pip. 79 (2002) 403-412.

[61] K.S. Kumar, S. Suresh, M.F. Chisholm, J.A. Horton, P. Wang, Acta Mater. 51 (2003) 387-405.

[62] M. Srinivas, G. Malakondaiha, R.W. Armstrong, P.R. Rao, Acta Metall. Mater. 39 (1991) 807-816.

[63] M. Srinivas, G. Malakondaiah, P.R. Rao, Acta Metall. Mater. 41 (1993) 1301-1312.

[64] T.L. Anderson: *Fracture Mechanics - Fundamentals and Applications*, 2^{nd} edition, CRC Press Inc., 1995.

[65] M.Tanaka, E. Tarleton, S.G. Roberts, Acta Mater. 56 (2008) 5123-5129.

[66] J.H. Chen, Q. Wang, G.Z. Wang, Z. Li, Acta Mater. 51 (2003) 1841-1855.

[67] S. Scheriau, *Severe Plastic deformation of ferritic and austenitic steels*, Phd-thesis, University of Leoben.

[68] F. Wetscher, R. Pippan, Phil. Mag. 86 (2006) 5867-5883.

[69] A. Latapie, D. Farkas, Phys. Rev. B 69 (2004) 134110-1-134110-9.

[70] D. Farkas, B. Hyde, Nano Letters 5(12) (2005) 2403-2407.

[71] S.L. Frederiksen, K.W. Jacobsen, J. Schiotz, Acta Mater. 52 (2004) 5019-5029.

[72] D. Chen, Mat. Sci. Eng. A 190 (1995) 193-198.

[73] S. Scheriau, *Korngrößeneinfluss auf die Orientierungsänderung bei der plastischen Verformung*, Diploma-thesis, University of Leoben.

5
List of appended papers

Paper A
A. Hohenwarter, A. Bachmaier, B. Gludovatz, S. Scheriau and R. Pippan
Technical parameters affecting grain refinement by high pressure torsion
International Journal of Materials Research (2009/12) 1653-1661

Paper B
A. Hohenwarter, R. Stock and R. Pippan
Severe plastic deformation of a bainitic rail steel
Material Science Forum 584-86 (2008) 655-660

Paper C
A. Hohenwarter and R. Pippan
Anisotropic fracture behavior of ultrafine-grained iron
Material Science and Engineering 527A (2010) 2649-2656

Paper D
A. Hohenwarter, A. Taylor, R.Stock and R. Pippan
Effect of large shear deformations on the fracture behavior of a fully pearlitic steel
Submitted for publication in Metallurgical and Materials Transactions A

Paper E
A. Hohenwarter, C. Kammerhofer and R. Pippan
The ductile to brittle transition of ultrafine-grained Armco iron: an experimental study
Accepted for publication in Journal of Materials Science

Remark

In the appended papers, myself, Anton Hohenwarter, performed all experiments, the data analyses and the composition of the publications with the following exceptions:

- In **paper D** A. Taylor performed the TEM investigations.
- In **paper E** C. Kammerhofer carried out the experiments in the framework of his diploma thesis.
- My supervisor, R. Pippan, participated in all the papers by giving the basic ideas for the publications and with helpful discussions during their preparation.

A

Technical parameters affecting grain refinement by high pressure torsion

A. Hohenwarter[a,b], A. Bachmaier[a], B. Gludovatz[a,b], S. Scheriau[a,b] and R. Pippan[a,b]

[a]Erich Schmid Institute of Materials Science, Austrian Academy of Sciences, A-8700 Leoben, Austria
[b]CD-Laboratory for Local Analysis of Deformation and Fracture, A-8700 Leoben, Austria

Abstract

High pressure torsion is a well known and widespread processing technique for severe plastic deformation. The aim of high pressure torsion and other comparable techniques is to obtain ultrafine-grained or even nanocrystalline materials with enhanced mechanical and physical properties compared with their coarse-grained counterparts. Generally this refinement process is strongly influenced by processing parameters such as temperature or accumulated strain, but can also simply be affected by the entire experimental setup. Therefore, the benefits and limitations of the process with regard to grain refinement, homogeneity and specimen size, underlined with experimental results using different tools, will be discussed.

A.1 Introduction

Torsion tests are commonly used in materials science when information about the stress-strain behaviour of a material at high strains is required which cannot be achieved by common means, such as the classical tensile test. This is because, for example, ductile materials generally fail due to a void initiation and coalescence process. This failure process is governed by the hydrostatic tensile stress component, ultimately leading to a limited fracture strain. The same is also true for brittle materials where the failure process is different. In a normal torsion test the fracture strain can be increased due to the absence of the hydrostatic tensile stress component. Bridgman showed that in a torsion test the fracture strain can be further increased by applying hydrostatic pressure [1], as the aforementioned failure process is inhibited. This basic principal was picked up again in Russia by Valiev [2,3] in the late 1980s and is today known as high pressure torsion (HPT). As for all severe plastic deformation (SPD) techniques, HPT is capable of producing ultrafine-grained (UFG) and nanocrystalline (NC) metals by imposing very high strains on coarse grained starting materials, leading to a strong but not well understood grain refinement process. The materials exhibit enhanced mechanical and physical properties due to their submicro- or nanocrystalline microstructure. The grain refinement process is strongly dependent on processing parameters , such as the imposed strain, the strain rate, the processing temperature and applied pressure, but is also dependent on the composition and purity of the processed material. These processing factors and the resulting mechanical properties of this young material class have been actively discussed in the literature in the recent years, summarised in [2, 4–6]. The principal benefit of HPT is the superimposed hydrostatic pressure which allows higher strains compared to other SPD techniques such as equal channel angular pressing (ECAP). This fact can lead to finer microstructures [7] or permit SPD of brittle or hard metals which are impossible or difficult to process by other SPD techniques [8, 9]. Additionally, other attractive application areas for HPT have come up in recent years, including powder consolidation [10, 11] and the production of supersaturated solid solutions [12]. Although there are many publications dealing with materials processed by HPT, published predominantly in the last 5 years, there are still discrepancies concerning basic technical issues. Therefore, in this paper some of these technical aspects are discussed and possibly clarified, as previously presented at the 4th International Conference on Nanomaterials [13] in an abbreviated form. Here we focus on addressing engineering aspects, notably the anvil design and the sample size rather than classical processing parameters, e.g. processing temperature or accumulated strain. This paper will begin with the different basic HPT processes and the resulting problems concerning mechanical processing will be discussed. Afterwards some technical problems, which could lead to the misinterpretation of results of HPT experiments, will be analysed. In the second part of the work some principal considerations for an upscaling of HPT samples are presented and underlined with an experimental study.

A.2 An overview of HPT equipment

A.2.1 The idealised HPT process

In the idealised HPT process the deformation procedure can be considered as a simple shear process where the shear strain can be evaluated, when no change in thickness is taken into account, as:

$$\gamma = \frac{2\pi r}{h} n \tag{A.1}$$

Here r is the radius, t the thickness of the specimen and n the number of revolutions. Normally criteria for equivalent strains are used to make the strain comparable to other deformation processes, for example a simple tensile test or rolling. A quite common criterion for the estimation of an equivalent strain, based on the equivalence of deformation energy, is the von Mises equivalent strain [14]:

$$\epsilon_{\mathrm{vM}} = \frac{\gamma}{\sqrt{3}} \tag{A.2}$$

In the idealised version of HPT, as shown in Figure A.1a, a disc shaped specimen is deformed between two anvils rotating with respect to another under an applied pressure. In the idealised unconstrained version, when the thickness of the disc is very small compared to the diameter, the stress state can be solved analytically. However, this idealised unconstrained version is technically difficult to implement as, for instance, there would be an ongoing decrease in the sample thickness. This is illustrated in the Fig. 1a at the bottom, showing the crossection of a Cu specimen rotated for 5 revolutions. On account of the ongoing decrease in thickness, the sample‘s edge becomes very thin and the shape is poorly defined. The strong thinning of the specimen can lead to contact between the rotating anvils which results in additional friction. This makes it difficult to use the applied torque for the estimation of the flow stress and it can destroy the tool. Furthermore a complex and inhomogeneous pressure distribution would develop in this case depending on the radius, the thickness to diameter ratio, t/d, of the sample, friction and flow stress. For that reason constrained versions of HPT have been in use in recent years. An idealised constrained HPT setup is shown in Figure A.1b. In this setup the specimen would deform under torsional straining and under hydrostatic pressure without any geometry change if there was no friction at the outer cylinder wall. Because friction is unavoidable no homogeneous shear deformation process can occur. Additionally, no dimensional tolerances are allowed. In the case that the anvil has a somewhat smaller diameter than the inner cylinder, which must be a fact in order to assemble the setup, material could flow out into the space between anvils and the outer cylinder. As an example this is indicated in Figure A.1b again with the cross-section of a Cu-sample subjected to one revolution showing an increase of the sample‘s thickness at the edge of the sample. This loss of material leads to unintentional friction and so to higher required torques for torsional straining.

A.2.2 Real HPT

The drawbacks mentioned and problems with the HPT types as discussed before are nowadays overcome with a setup as illustrated in Figure A.1c, also termed quasi-constrained HPT.

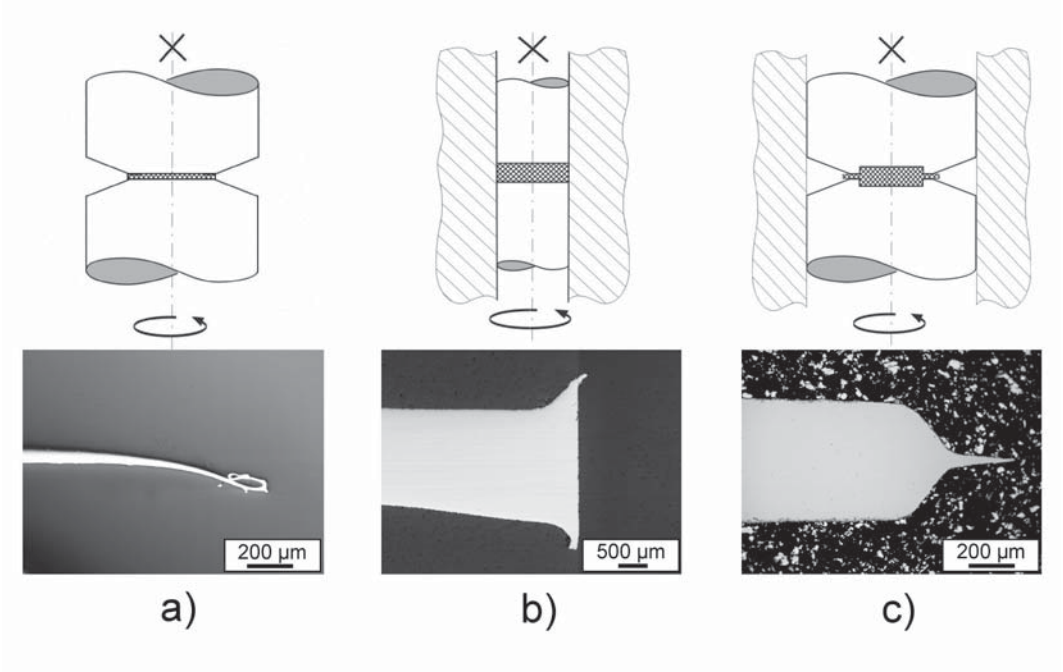

Figure A.1 Schematic illustrations of types of HPT and associated examples of cross-sections of samples produced with the different experimental setups at the bottom: (a) idealised unconstrained HPT, (b) idealised fully constrained HPT, (c) quasi-constrained HPT, a practical version.

Here both anvils have a cylindrical cavity. This cavity enables a central positioning of the specimen, which is important for accurate torsional straining. The sum of the depths of these cavities must be less than the sample thickness and furthermore some height loss of the sample during straining must be included. This amount of compression deformation is usually in the range of 5-10 % and is most of the time neglectable compared to the high imposed shear strains. Besides accurate positioning of the specimen, the cavity primarily allows hydrostatic pressure. When the specimen is loaded a certain amount of material flows out into the gap between the anvils, this material then becomes confined in this zone due to friction. This constraint leads to a backpressure and induces a hydrostatic pressure in the processing zone. This material also prevents the anvils from touching and so no failure of the anvils during the processing occurs. A cross-section of an Fe sample subjected to 5 rotations produced with this setup is shown in Figure A.1c at the bottom showing a very defined shape in contrast to the aforementioned specimens. However, this realistic HPT setup has some technical difficulties and limitations too, which can

cause misinterpretation of results.

A.3 Technical factors affecting HPT results

A.3.1 The HPT setup

In torsion the shear strain should increase linearly with the radius. For single phase materials after straining at room temperature in the range of ϵ_{vM}=16-32 a saturation of hardness, as a consequence of reaching a minimum grain size, evolves. Therefore, with increasing number of rotations the zone of homogeneous hardness/microstructure should increase towards smaller radii. Despite this, a small undeformed or less deformed area should still be present at small radii, even after many revolutions. In the literature one can find contradictory results. Some reports showed a uniform microstructure [15] whereas more recent studies found that the linear increase of the shear strain is well fulfilled or in other words that there is no deformation in the very centre of the disc [16, 17]. Possible reasons for these contradictory opinions can be found in deviations of the real HPT setup from the ideal one. Firstly, before loading and during shear deformation of the sample an additional compressive deformation occurs, which also affects the centre of the specimen. A stronger effect comes from a small parallel shift of the rotation axis of the anvils, enhancing deformation in the centre. These deviations make the deformation more complex and can lead to the result of a fully homogeneous specimen after deformation. Regarding our experiences using an outer guide, as illustrated in Figure A.1c, holding the anvils centred leads to strict rotational straining and a hardness gradient in the middle of the specimen, as explained in [16], even after many rotations (15-20 rotations). Generally these technical factors are not of great interest for samples subjected to very large strains, however it must be of great interest for the modelling of the HPT deformation process, for instance for strain gradient plasticity modelling [18].

A.3.2 The applied pressure

In the literature there are different opinions about the influence of the applied pressure on HPT results, especially on the resulting grain size. Some reports show a distinctive influence of the pressure [19], whereas others found no influence [9]. This particular question will not be discussed here, but rather the technical significance of the pressure for the HPT straining process. In order to start an experiment the cavity of the HPT anvils must be fully filled with the specimen material. Thus the penny shaped specimen, as indicated in Figure A.2a, must deform fully plastically and flow into the small slit between the two anvils.

For that a pressure at least equivalent to the yield strength of the material is necessary. Furthermore, the anvil and the sample surfaces are sandblasted in order to create a distinctive surface micro-roughness. Through this combined with the pressure sufficiently high friction forces for the rotational straining can develop. As

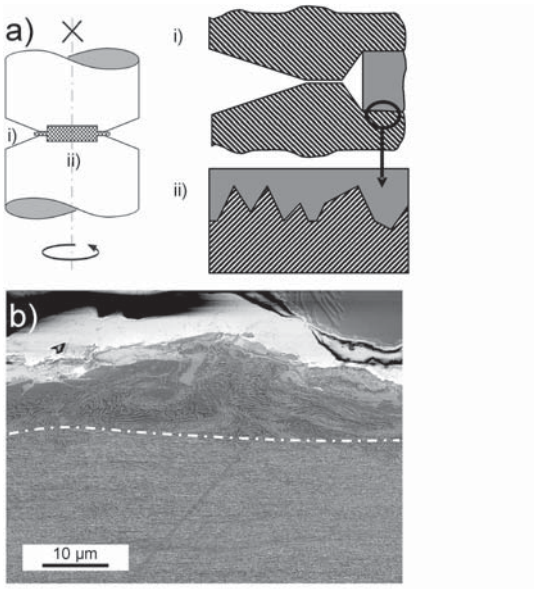

Figure A.2 Compressive pre-deformation of samples for HPT: (a) configuration of the anvils and specimen before deformation, showing the areas of interest, (i) schematic drawing of the shape of the cavity which must be filled and the specimen before deformation; (ii) micro-asperities on the anvils' surface which must be filled to induce friction, (b) micrograph of such an asperity on the sample after deformation, with an undeformed pearlitic structure (lamellae are visible), attached to the shear deformed area underneath with no visible structure.

a rule of thumb [20] the minimum pressure for the plastic deformation of the metal's surface and the following filling of these asperities is at least three times the yield stress of the undeformed sample material. This pressure leads to a plastic flow of the sample material into the micro-asperities and an excellent fitting between sample and anvil for the subsequent rotational straining. This fact is illustrated schematically in Figure A.2a. Figure A.2b shows a real example of such an asperity at the edge of a deformed steel sample. In the upper part of the picture an almost undeformed microstructure consisting of a lamellar structure is visible. In the lower part of the picture a strong shear deformation occurred in the interior of the sample. The upper boundary for the possible pressure is 3 times the yield stress of the anvils, which, in the case of a modern high speed tool steel, is in the range of 8-9 GPa. Since nowadays most anvils posses a cavity, which acts as a notch, the maximum possible processing pressure is somewhat smaller. Between these boundary conditions for the pressure, increasing pressure can lead to higher maximum degrees of deformation when hard deformable materials are considered. This will be discussed here for a pearlitic steel, as a representative hard deformable metal. In Figure A.3 the torque recorded during deformation as a function of number of rotations for different pressures is plotted for this steel and pure iron. The strain rate was 0.2 rotations/min. Experimental details concerning the HPT equipment and the in-situ torque measurement technique can

be found elsewhere [21]. One characteristic of the pearlitic steel is that it hardens significantly in the deformation range investigated, which is equivalent to an ongoing increase in torque. The measured torque is used as an indicator for the maximum degree of deformation and as an indicator for a possible sliding of the specimen. For this steel in the investigated deformation range, up to one rotation, a levelling out or even a decrease in torque can be attributed to relative sliding between sample and anvil. This can be asserted, since on the sample itself an initially drawn line cannot be found after the experiment is stopped right at the point of maximum achievable torque. The drawn line vanishes because of relative sliding between anvil and sample. Naturally the HPT experiment could be continued, however the measured torque originates from the relative sliding between sample and anvil and not from shear deformation of the sample. Further revolutions would not increase the degree of deformation.

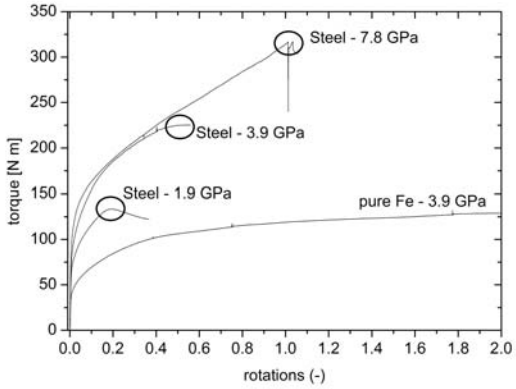

Figure A.3 Comparison of the measured torque of a pearlitic steel for different applied pressures as a function of the number of rotations: higher processing pressures generally lead to higher degrees of deformation.

In contrast to this, a typical one phase material, here pure iron, shows a saturation of torque or shear flow stress after ∼2 rotations. This is on account of reaching a lower limit of achievable grain refinement and not because of any sliding effects. The lines drawn on the sample surface are clearly visible after the experiment. Regarding the pearlitic steel an increase in the pressure from 1.9 GPa to 3.9 GPa lifts the maximum degree of deformation from ∼0.2 to ∼0.4 rotations, followed by a decrease or a plateau in the torque. This means a maximum degree of deformation is reached, since the friction is too low for further deformation. Processing at the highest pressure leads to the highest strain of ϵ_{vM} ∼16 which corresponds to one rotation. After about one rotation an abrupt decrease in the torque can be seen, which is fairly similar to a stick-slip event. Examining such a specimen also reveals a shiny sample surface and often small deformations of the anvil. The hardness of the sample reaches the hardness of the anvil, which is about 60-62 HRC. Therefore, an

upper boundary for the deformation of metals by HPT can be seen in the resulting strength of the processed metal. When the grain refinement process leads to the same or even to a higher strength of the processed metal compared to the tool then deformation of the tool can set in.

To summarise, for difficult to deform materials the increase in the processing pressure can lead to significantly higher strains and so to a more pronounced grain refinement. However, the success of the experiment or the upper limit of the fragmentation in such cases is also dependent on the anvil material. Assuming the maximum possible hardness of the HPT processed metal is higher than of the HPT tool then this lower limit of grain refinement cannot be reached. The same phenomenon has also been found by our group for other difficult to deform metals, such as tungsten and tungsten alloys. An improvement here can be exclusively achieved by harder anvils, for instance hard metals, or an increase in the processing temperature. However a higher temperature generally leads to a larger minimum grain or structure size and usually also causes a decrease in the strength of the tools.

A.4 Upscaling of HPT and limitations of the sample size

A.4.1 Technical aspects

The major disadvantage of HPT has always been the very small sample size, which made this method unattractive for a lot of tests and applications. Thus in recent years there has been a strong desire to increase the size of HPT samples, as shown in [22, 23]. From the engineering point of view there is no limit to the sample size as long some technical aspects are kept in mind. For torsional straining a minimum pressure is needed in order to obtain sufficient frictional force such that no relative sliding between the anvil and specimen surface occurs. As a rough estimate the pressure must be 3 times higher than the yield stress of the material. The maximum achievable pressure is determined by the hardness of the anvils. The second aspect which must be taken into account is the torque necessary to deform the specimen. Since the required torque for deformation scales with the cube of the sample diameter, stronger motors for the HPT equipment are required as the diameter of the specimen is increased. Simultaneously the anvil diameter must also increase in order to withstand the higher torques if the anvil material remains the same. Since the friction zone between the anvils, where material flows out, also becomes larger, a further increase in torque must be expected. In addition to that the accuracy of the torsional axis becomes more difficult with larger piston diameters. The requests for upscaling of HPT in our group led to a machine with a maximum nominal loading capacity of 4000 kN, whereas our standard device had a maximum capacity of 400 kN. This increase in the loading capacity allowed for an increase in the sample diameter, formerly in the range of 8 - 14 mm, to 30 - 40 mm by keeping the maximum pressure almost constant. For the same reason anvils with larger diameters were also needed to withstand the higher torques. Here the diameter was increased from 40 to 150 mm. Additionally a strong motor, with a maximum driving

torque of 13 kN m, was required to enable the torsional straining of the sample under fully plastic flow. Finally it should also be noted that the rotational speed must be decreased in order to reduce the heating of the specimen. This heating arises firstly from the strong plastic deformation and secondly from friction in the area where material flows out between the anvils. This aspect becomes more prominent when the sample size, and so the volume of the sample, is strongly increased.

A.4.2 The homogeneity of deformation

An important question from the materials science point of view is if a pronounced homogeneity of the specimen in large areas can be reached after a certain saturation strain. This query generally refers to a certain region or radius of the specimen because samples used to have a large diameter in respect to a small thickness. However, when the sample size is also increased in height the homogeneity along the thickness, so to speak the axial homogeneity, of the specimen becomes an issue as well. For instance in the work of Sakai et al. [23] samples were produced with diameters of about 10 mm and thicknesses of about 9 mm. Here a strong localisation of the deformation in the middle plane of the specimen could be seen on the micrographs. For some applications or studies this inhomogeneity is not a problem, for instance when tensile specimens are produced from the middle plane of the HPT disc. For other tests or subsequent heat treatments a strong microstructural gradient along the height of the specimen can be a limiting factor. Therefore, when HPT samples are upscaled and a strong homogeneity is requested, this homogeneity must be not only along the radius, but also across the thickness of an investigated sample. For this a study into the homogeneity problem is presented next. Armco-iron was used, which is a typical single phase bcc metal and shows a minimum grain size of about 200 nm after equivalent strains, ϵ_{vM} of ~ 16 after HPT at room temperature. For this experiment 3 different samples with diameters of 8 and 30 mm and thicknesses of 0.6 mm, 3.5 and 5.4 were produced. This results in thickness to diameter ratios, t/d, of 1/13, 1/9 and 1/6, respectively. Here the thicknesses are measured after deformation and represent average values measured at different positions along the specimen diameter. This was done because the specimens develop a slight elliptical shape due to the elastic deformation of the tool. The samples were pre-deformed in order to fill the cavity of the anvils, then recrystallised at 800 °C for one hour. They were then deformed by HPT at room temperature up to ten rotations at a nominal pressure of 2.8 GPa. The deformation speed was 0.2 rotations/min for the small sample and 0.07 rotations/min for the larger ones (30 mm diameter). In order to study the homogeneity of the resulting microstructure, hardness measurements were performed along the middle plane and across the thickness of the specimens at specific radii, as indicated in Figure A.4a schematically. For each data point 3 indents were made at equivalent positions and averaged. The measurements were performed with a Vickers indenter and a load of 200 gf.

Radial homogeneity in the saturation regime

The position of the hardness indents in the cross-section of the HPT sample is schematically drawn at the bottom of Figure A.4a for the radial hardness distribution as well as for the axial distribution, which will be discussed later. The graph shows the hardness along the middle plain of the specimens as a function of the normalised radius, r/R, for better comparison. It can be seen that for the 3 different specimens at a radius of about 0.2R, corresponding to radii of 0.8 for the 8 mm specimen and 3 mm for the 30 mm specimen, a fairly constant hardness level is reached which can be regarded as a maximum value. The difference in the saturation hardness between the smallest and the other specimens is apparently due to the slightly higher purity of the 8 mm rod in contrast to the 30 mm rod starting material. As said before, the onset of saturation is about at 0.2R. This position corresponds to different equivalent strains for the different specimens. In the case of the "large" specimen (t/d=1/6) this position corresponds to an equivalent strain of ~ 20, for the "medium" specimen (t/d=1/9) it corresponds to a strain of ~ 30 and for the "small" specimen (t/d=1/13) the equivalent strain is about 50. Although the different specimens underwent totally different degrees of deformation they reach a "saturation" level almost at the same geometrical position. For very small radii, roughly less than 0.1R a decrease in hardness can still be seen which is also expected for low strains. The hardness plots in Figure A.4a show that hardness saturation is achieved in the central plane of the samples independent of the geometry. This is achieved as long as the local strain is sufficient to fully refine the microstructure. However, this pronounced homogeneity cannot be assumed for the hardness across the thickness, as excessive specimen heights could potentially lead to a geometrical localisation of the deformation. As a consequence, hardness measurements across the thickness of the discs were also performed.

Axial homogeneity in the saturation regime

The height profiles were measured at radii of 3 mm, 7.5 mm and 13.5 mm for the medium and large specimens and at radii of 0.8, 2 and 3.6 mm for the smallest specimen. In all cases the radii correspond to positions of 0.2R, 0.5R and 0.9R. This was done in order to make a comparison of the different specimen diameters. In Figure A.4b-d the hardness distributions of the investigated specimens along the thickness coordinate starting from the middle plane (coordinate=0) heading to both outer planes are shown (± 2.5 mm, ± 1.5 mm, ± 0.2 mm).

A decrease in hardness towards to the edges of the specimens can be seen immediately, especially in the case of the large sample (t/d$\sim$1/6), Figure A.4b. Here the maximum difference of hardness between the middle of the specimen and the edge is about 70 HV. In case of the medium specimen (t/d$\sim$1/9), Figure A.4c, the decline is already less pronounced, the difference makes $\sim$40 HV. For the smallest specimen, Figure A.4d, (t/d$\sim$1/13), the maximum change is the smallest, the maximum difference makes $\sim$25 HV. It should be noted that in absolute numbers the

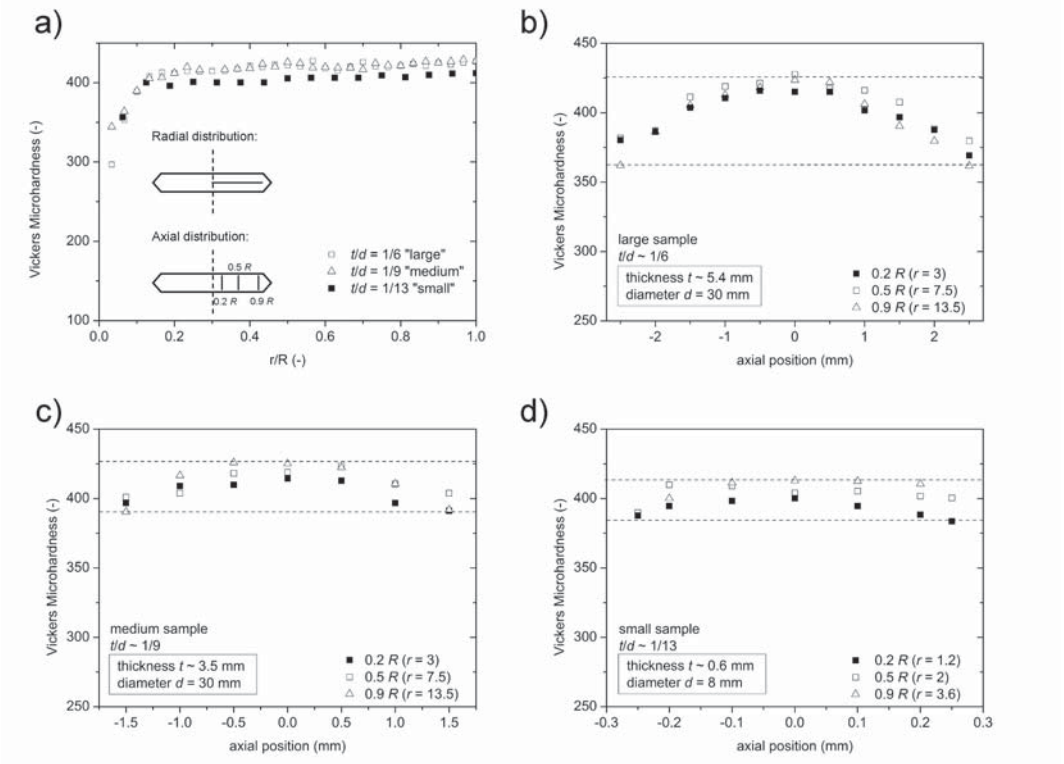

Figure A.4 Hardness distributions of pure iron: (a) comparison of the radial hardness distribution for different sample sizes, (b-d) hardness distributions of the investigated samples across the thickness at different radii.

"large" sample shows the largest area of homogeneous hardness, Figure A.4b, which spans about 2 mm. However when the homogeneity throughout the whole specimen is considered the "small" specimen shows the lowest decrease in hardness. This indicates that with decreasing thickness to diameter ratio, t/d, the absolute decrease in hardness becomes smaller. One can conclude that if a strong homogeneity across the whole thickness of a specimen is required the thickness to diameter ratio should be taken into account. According to this study this ratio should be smaller than $\sim$1/13. Additionally, a minimum strain for saturation must be achieved. The next question is why such hardness variations occur even in the case of very small sample ratios (t/d$\sim$1/13), which was deformed far beyond a saturation level for small radii. The radial hardness distribution, Figure A.5a, and the axial distribution at a radius of 8 mm, Figure A.5b, of the pearlitic steel is presented.

As mentioned before this steel shows no saturation in the processable deformation range and as such is suitable for homogeneity studies excluding a maximum attainable hardness level. On account of a larger sample, see Figure A.5b, up to three rotations are possible. However the maximum strain at the highest radius was in the study discussed before and here the same. One can see in Figure A.5a that up to

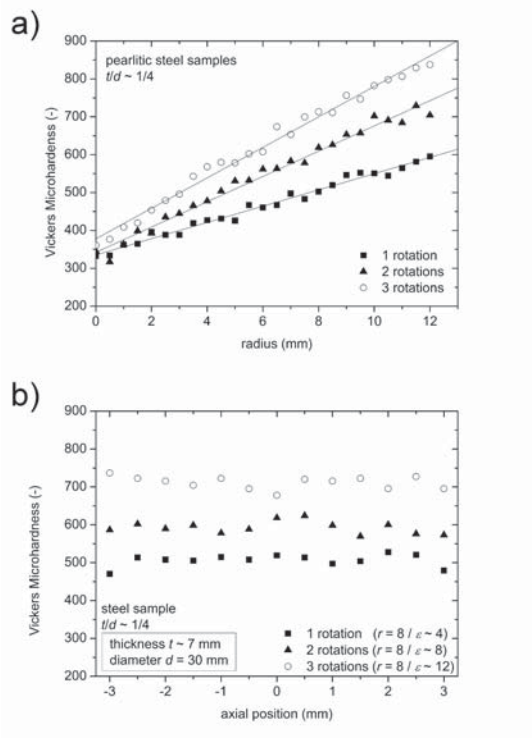

Figure A.5 Evolution of the hardness of a pearlitic steel as a function of number of rotations: (a) linear increase in hardness along the radius, (b) fairly constant axial hardness distribution for small radii.

three rotations, which is, in the case of the steel, the maximum applicable strain, a linear increase in hardness is present. This indicates that a hardness saturation level is not reached. In Figure A.5b the axial distribution of the hardness for the radial centre of the specimen (r=8 mm) is shown. It shows that for one to three rotations a fairly homogeneous hardness evolves along the axial position. This occurs despite the fact that the thickness to diameter ratio, t/d, is very extreme in these specimens (t/d=1/4). In contrast to this, at higher radii, not shown here, a strong decline in hardness from the middle plane towards the margins of the specimen is measured, very similar to the iron results presented previously. This indicates that the reason for these axial inhomogeneities regarding the iron results is not metallurgical. This can be asserted as a process such as recrystallisation would not enable this pronounced homogeneity at a fixed radius with varying strain while still causing strong deviations from homogeneity at higher radii. Therefore, other reasons, for example unexpected friction zones, must be responsible for an inhomogeneous axial hardness distribution, even if the t/d ratio is very small. For that reason metallographic cross-sections of the iron samples were taken to further investigate this. As an example the largest investigated iron sample with a t/d ratio of ∼1/6 is demonstrated in Figure A.6a.

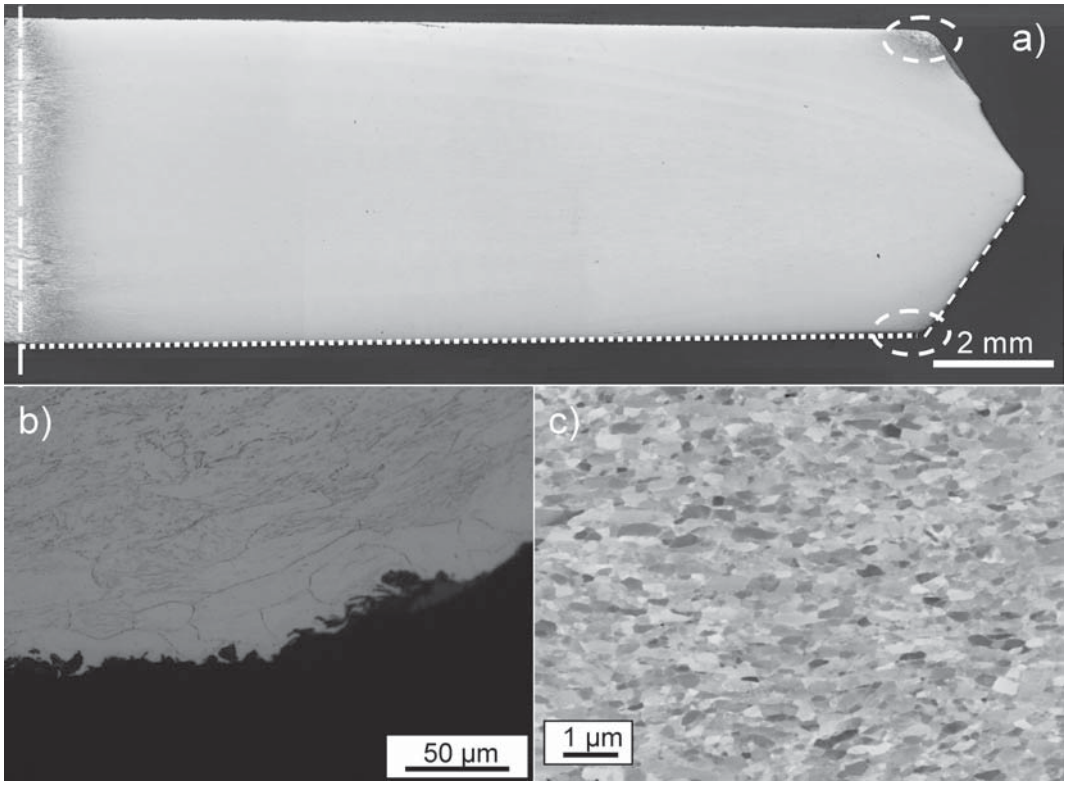

Figure A.6 Micrographs of the largest HPT sample investigated: (a) cross-section along the radius, (b) edge zones of the specimen showing a undeformed recrystallised structure, (c) severely deformed microstructure of iron taken at the same radius as in (b) but in the middle plane.

This sample was grain boundary etched after polishing in order to reveal possible less-deformed regions. On the left side of the picture the former rotation axis is indicated with a dashed line. In this section a less deformed region is clearly visible. This is to be expected as the strain experienced by the sample close to the rotation axis is insufficient to cause strong grain refinement. In the centre and also at the edge region of the specimen no etching can be seen due to the strong grain refinement. However at the maximum radius of 15 mm etched regions are visible revealing a grain structure at the top and the bottom corners. These regions undergo less or even no deformation and can be called dead zones. In Figure A.6b such a dead zone is demonstrated at higher magnifications, where the recrystallised starting structure is clearly visible. In contrast to this in Figure A.6c one can see the ultrafine-grained microstructure taken at the same radius but from the middle plane. This implies that in the corner of the edge regions less or even no shear deformation takes place. These regions seem to develop automatically when anvils for quasi constrained HPT, which have a depression, are used. Normally the flat surfaces of the anvils' depressions pressurise the sample and generate sufficient frictional force, essential for the

rotational straining of the specimen (this area corresponds to the dotted line on the specimen in Figure A.6a). At the slants of the depression friction is undesirable so that the specimen can deform unimpededly. The slants of an anvil correspond to the inclined areas of the specimen in the edge region, indicated with another dashed line in Figure A.6a on the right hand side. The transition from the area where friction is required to areas where friction would impede the deformation is continuous and does not change abruptly. Therefore, in the corners of the sample the material becomes constrained against deformation, resulting in an undeformed region, and on a larger scale a less deformed region, spanning from the edges of the specimen along the margins to the centre of the specimen, which is less deformed again. In other words, these dead zones constrain the deformation of the whole sample and their size controls the axial area of homogenous hardness. Similar results and tendencies regarding the sample size and hardness distribution have already been obtained in our group with other metals, for example copper and an austenitic steel. Based on these results a different geometry of the anvils' cavities was designed in order to try to achieve a better axial hardness homogeneity. A corresponding specimen after deformation is shown in Figure A.7a.

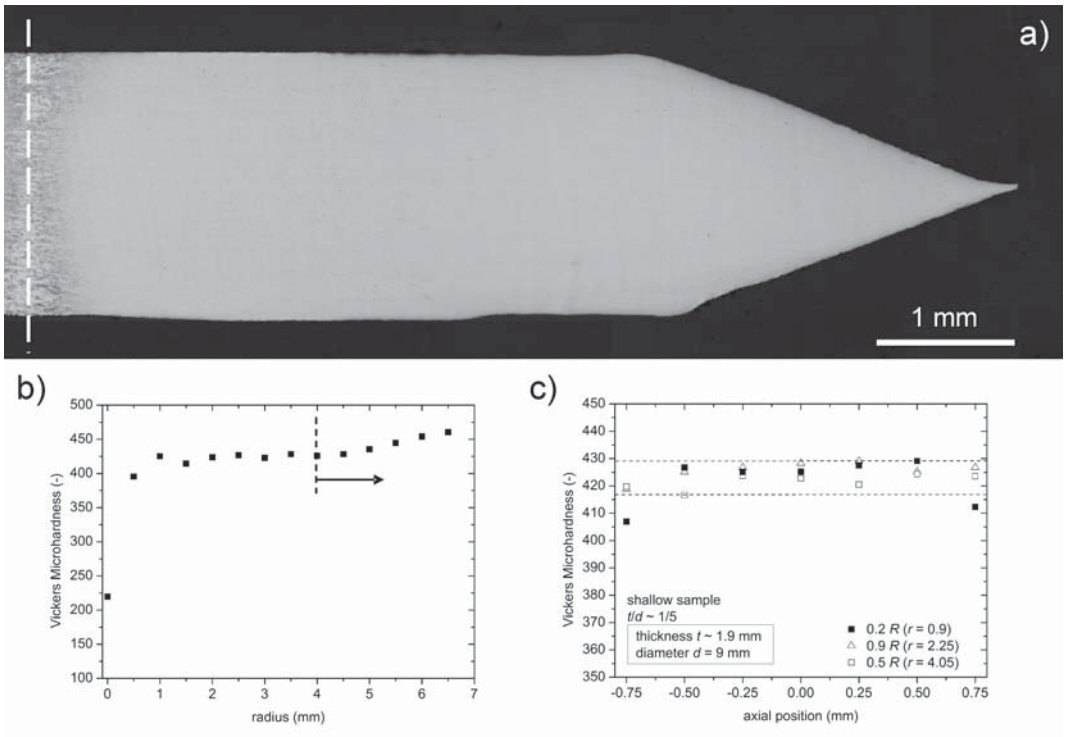

Figure A.7 Results from an iron specimen with a modified sample geometry: (a) cross-section of the specimen, showing a very smooth gradient of the specimens shape at the edge, (b) radial distribution of the hardness, (c) axial distribution of the hardness of this sample.

The iron sample was again deformed up to ten rotations at a nominal pressure of 2.8 GPa. In contrast to the sample presented before the edge region here has a fairly smooth shape. The angle between the flat depression and the inclined edge is about 20°. The samples before had an angle of about 50°. Such a sample has no real transition from an area where friction is needed to an area where friction constrains the deformation as explained before. Since the transition from the area of constant height to the area with decreasing height is very shallow the volume elements in the edge area also perform a similar shear deformation as volume elements in areas of constant height. For that reason also the smooth edge region of the sample is sandblasted since a shear deformation in this region is intended. Therefore, no dead zones can be found in this specimen. As a consequence a very homogeneous hardness distribution can be achieved with just small variations of the absolute values, as presented in Figure A.7c, even though an extreme t/d-ratio of 1/5 was chosen. The stronger decline of hardness at the margins (axial position=0.75 mm) for the smallest radius (r=0.9) is due to insufficient applied strain. This is observable on the left hand side of Figure A.7a, where the coarse grained centre of the specimen is visible.

Another surprising aspect of this specimen can be seen when the radial hardness distribution of the specimen is analysed, Figure A.7b. As usual a constant hardness level is reached at small radii. However here at radii larger than 4.5, which corresponds to the end of constant specimen height, an increase in the hardness is visible and indicated with an arrow in Figure A.7b. This further increase can be associated with the geometry of the sample. In this type of sample in the edge region the height decreases constantly towards zero for the maximum radius. Thus regarding the equation for the shear strain, Section 2.1, the strain and the strain rate increase dramatically in this area. Since all studies presented previously showed that the maximum hardness after reaching the saturation regime is fairly independent of the radius and strain, only a certain strain rate sensitivity remains to be responsible for the higher hardness, as also found in [24]. The strain rate changes here from about 0.03 s^{-1} at a radius of 4.5 mm to 0.8 s^{-1} at a radius of 6.4 mm. This strain rate sensitivity seems to influence the axial homogeneity positively, especially in the saturation regime. The same effect could be achieved using a specimen consisting of an inner and an outer ring made out of different metals. If the outer ring had a higher strain rate sensitivity or exhibited a saturation at higher strains, the outer ring would stabilise the axial homogeneity of the inner ring.

A.5 Summary

In this paper important engineering aspects and requirements of HPT processing, were discussed. Special focus was set on the feasibility of upscaling the process to larger homogeneous samples. It was shown that fairly homogeneous ultrafine-grained samples of Armco iron can be produced through HPT if firstly a material-dependent saturation strain is reached and secondly if distinctive geometrical ratios are taken into account:

- In order to obtain a quite homogeneous ultrafine-grained microstructure in the majority of a specimen the ratio of the thickness, t, of the sample to the diameter d, t/d, should not exceed a certain limit, which for Armco iron here was about 1/13 or smaller. For larger ratios the region of pronounced homogeneity can at least span several millimetres, which can be suitable for a range of tests or even applications.

- Another strategy to obtain a pronounced axial homogeneity is to take samples and corresponding anvils with a very shallow edge region. Here undeformed or less deformed regions can be avoided, which are a principal reason for the axial inhomogeneities. Furthermore, very high strain rates, resulting in a further increase in hardness, can be reached, which stabilise the homogeneity at smaller radii. A similar effect on the homogeneity can be expected performing the deformation process at elevated temperatures because the strain rate sensitivity increases and so a stronger homogeneity can be assumed. Another technical advantage of the smooth edge region is that the anvil is less prone to fail through elevated stresses in contrast to the classical anvil design.

Nevertheless, only the influence of the geometry was studied here. In future such investigations should be extended to other pure metals and alloys, which could show other tendencies regarding the homogeneity on account of physical factors such as the recovery and recrystallisation behaviour.

Bibliography to paper A

[1] P.W. Bridgman: J. Appl. Phys. 14 (1943) 273-283.

[2] R.Z. Valiev, R.K. Islamgaliev, I.V. Alexandrov: Prog. Mater. Sci. 45 (2000) 103-189.

[3] T.G. Langdon: Mater. Sci. Eng. A (503) (2009) 6-9.

[4] R.Z. Valiev, T.G. Langdon: Prog. Mater. Sci. 51 (2006) 881-981.

[5] A.P. Zhilyaev, T.G. Langdon: Prog. Mater. Sci. 53 (2008) 893-979.

[6] M. A. Meyers, A. Mishra, D.J. Benson: Prog. Mater. Sci. 51 (2006) 427-556.

[7] A.P. Zhilyaev, B.K. Kim, J.A. Szpunar, M.D. Bar, T.G. Langdon: Mater. Sci. Eng. A 391 (2005) 377-389.

[8] M. Faleschini, H. Kreuzer, D. Kiener, R. Pippan: J. Nuclear Mater. (2007) 367-370.

[9] F. Wetscher, A. Vorhauer, R. Stock, R. Pippan: Mater. Sci. Eng. A 387 (2004) 809-816.

[10] T. Tokunaga, K, Kaneko, Z. Horita: Mater. Sci. Eng. A 490 (2008) 300-304.

[11] Z. Lee, F. Zhou, R.Z. Valiev, E.J. Lavernia, S.R. Nutt : Scripta Mater. 51 (2004) 209-214.

[12] X. Sauvage, P. Jessner, F. Vurpillot, R. Pippan: Scripta Mater. 58 (2008) 1125-1128.

[13] R. Pippan, S. Scheriau, A. Hohenwarter, M. Hafok: Mater. Sci. Forum 584-586 (2008) 16-21.

[14] H.P. Stwe: Adv. Eng. Mater. 5 (2003) 291-295.

[15] A.P. Zhilyaev, G.V. Nurislamova, B.K. Kim, M.D. Kim, M.D. Bar, J.S. Szpunar, T.G. Langdon: Acta Mater. 51 (2003) 753-765.

[16] A. Vorhauer, R. Pippan: Scripta Mater. 51 (2004) 921-925.

[17] C. Xu, A.P. Zhilyaev, Z. Horita, T.G. Langdon: Mater. Sci. Forum 584-586 (2008) 3-8.

[18] Y. Estrin, A. Molotnikov, C.H.J. Davies, R. Lapovok: J. Mech. Phys. Solids 56 (2008) 1186-1202.

[19] M.J. Zehetbauer, H.P. Stwe, A. Vorhauer, E. Schafler, J. Kohout: Adv. Eng. Mater. 5 (2003) 330-337.

[20] F.P. Bowden, D. Tabor: Friction and lubrication of solids, Clarendon Press, Oxford (1954).

[21] F. Wetscher, A. Vorhauer, R. Pippan: Mater. Sci. Eng. A 410-411 (2005) 213-216.

[22] Y. Harai, Y. Ito, Z. Horita: Scripta Mater. 58 (2008) 469-472.

[23] G. Sakai, K. Nakamura, Z. Horita, T.G. Langdon: Mater. Sci. Eng. A 406 (2005) 268-273.

[24] A. Vorhauer, R. Pippan : Metall. Mater. Trans A (2008), volume 39, 417-429.

B

Severe plastic deformation of a bainitic rail steel

A. Hohenwarter[a,b], R. Stock[c] and R. Pippan[a,b]

[a]Erich Schmid Institute of Materials Science, Austrian Academy of Sciences, A-8700 Leoben, Austria
[b]CD-Laboratory for Local Analysis of Deformation and Fracture, A-8700 Leoben, Austria
[c]Voestalpine Schienen GMBH, Kerpelystr. 199, A-Leoben 8700, Austria

Abstract

Severe Plastic Deformation (SPD) is known to be an effective method of producing nanocrystalline materials, for instance by High Pressure Torsion (HPT) and Equal Channel Angular Pressing (ECAP). These techniques are also capable of reproducing microstructures which arise naturally when high pressure and friction is involved, for example in wheel-rail contact problems. The resulting deformation layers build the origin point for fatigue cracks. For that reason the knowledge of the mechanical properties of these deformation layers are of vital importance. In the framework of this study a baintic rail steel quality was deformed by HPT up to distinctive equivalent strains at a nominal pressure of 6 GPa up to a final equivalent strain of 16. Afterwards the evolution of the resulting microstructure was investigated by scanning electron microscopy, by microhardness measurements and X-ray diffraction. The bainitic structure showed a strong alignment and fragmentation into the shear direction with increasing strain, which was accompanied by an increase in hardness as well. X-ray diffraction measurements showed that the amount of retained austenite decreases dramatically after small amounts of strain, indicating that retained

austenite cannot be stabilized by high pressures. Torque measurements during deformation showed after strong hardening at the beginning, a saturation behavior for higher strains, whereas for instance pearlitic rail steel qualities show further hardening.

B.1 Introduction

Nowadays railway systems are gradually more and more subjected to higher train speeds and larger axle loads. The wheel-rail contact causes high contact forces, with a high hydrostatic pressure component and on account of various kinds of slippage between rail and wheel a certain amount of plastic deformation takes place. Therefore distinctive surface modifications arise, which can result in a strong refinement of the microstructure or even in a transformation into a nanocrystalline structure [1]. These surface modifications frequently build the origin of rail defects, such as headchecks [2]. For that reason the microstructure and the mechanical properties of such deformation layers are of interest. In the last decades a variety of studies have shown that severe plastic deformation (SPD) is capable of producing materials with remarkable physical and mechanical properties due to a strong grain refinement [3,4]. Among this techniques High Pressure Torsion (HPT) represents a simple and effective method which allows one to produce reproducible and well defined samples. In this study HPT is used to deform rail steels in order to investigate the resulting microstructure as a function of strain structurally and mechanically. In contrast to samples extracted from a rail these samples have a well defined deformation history. The aim of this study is to characterize the changes of the microstructure of carbide-free bainitic rail steels due to HPT and compare the results with former works dealing with classical pearlitic rail steel qualities, which were subjected to HPT.

B.2 Experimental

In the framework of this study two different carbide-free bainitic steels denominated as quality 1 and quality 2 were investigated. The samples had a diameter of 8 mm and a thickness t of approximately 0.8 mm. The primary material was subjected to HPT at a nominal pressure of 6 GPa at room temperature with a constant rotation speed of 0.2 rotations per minute. The samples were deformed up to equivalent strains of 1, 2, 4, 8 and 16 referring to a radius of 3 mm. The von Mises strain ϵ_{vM} was calculated according to the following formula

$$\epsilon_{\mathrm{vM}} = \frac{2\pi r n}{t_{\mathrm{m}}\sqrt{3}}. \tag{B.1}$$

Here r is the radius, t_m is the average thickness calculated of the thicknesses before and after deformation and n is the number of rotations. Since the degree of

deformation is a function of the radius there is a strong need to refer any kind of investigation to a special position as shown in former studies [5]. For that reason all studies refer to a radius of 3 mm looking into the radial direction as shown in Figure B.1.

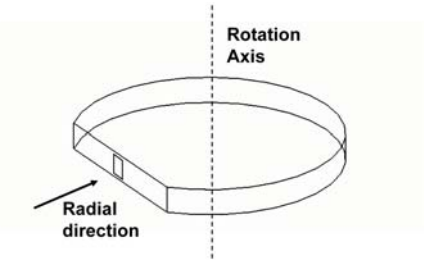

Figure B.1 Schematic sketch of the HPT-sample indicating the direction of investigation.

The rectangle shows the position of all following investigations. The evolution of the resulting microstructures were investigated with a scanning electron microscope (SEM) LEO 1525 using a secondary electron detector. Moreover the SEM is equipped with an TSL-EBSD system, which was used to obtain phase information. For the SEM studies the samples were ground, polished and finally etched with picric acid. Mechanical changes in hardness due to highly imposed strains were measured with a micro hardness equipment from Buehler with a testing load of 1 kg. At least 3 indentations were made at a radius of 3mm, respectively. In order to follow the hardening behavior of the material during SPD in-situ torque measurements were performed as presented for instance in [6]. Finally retained austenite X-ray measurements were made on a Seifert PTS 3000, using Mo-radiation with a wavelength of 0.07093165 nm.

B.3 Microstructure of the starting material

In Figure B.2 the starting material of quality 1 is compared in a SEM image and an EBSD map. An overview of the production process and the benefits of such named carbide-free bainitic steels is given in [7]. The EBSD phase map, Figure B.2b, shows regions of bcc-iron indicated in light grey and regions of fcc iron indicated in dark grey. In comparison with the SEM image it can be seen that the laths of bainitic ferrite are separated and interrupted by retained austenite (fcc). Additionally in the EBSD phase map black regions are visible, which could not be indexed by the EBSD system. These regions are already transformed into martensite either due to the preparation technique or on account of the production process. Regarding the SEM image it can be seen that regions which are more strongly etched are bainitic sheaves (bcc) and regions which are elevated or slighter etched are austenitic (fcc) or already transformed into martensite.

The metallographic constituents of the second alloy, quality 2, are the same, however the bainitic sheaf structure is generally finer. Since this is the only difference

the structure of quality 2 is not discussed more in detail.

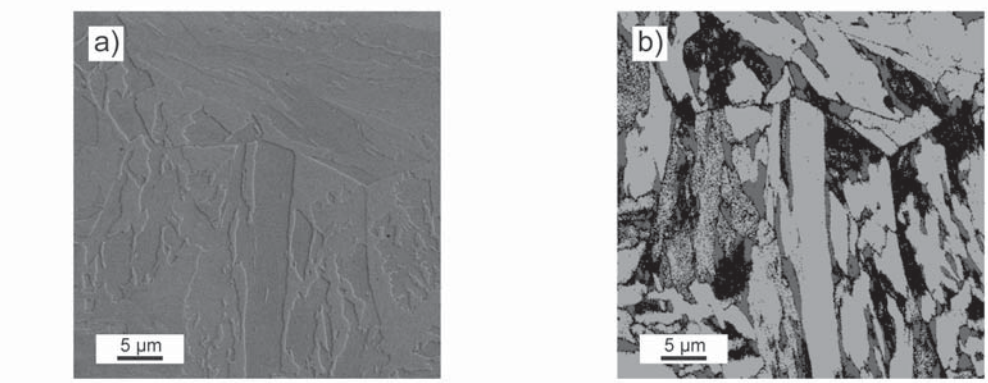

Figure B.2 Comparison between a SEM image (a) and an EBSD phase map (b) taken from the same area showing retained austenite embedded into bainitic sheaves. In the EBSD phase map retained austenite regions (fcc) are dark grey, bainitic sheaves (bcc) are light grey and martensitic regions are black.

B.4 Microstructural changes due to High Pressure Torsion

All images are taken from the radial direction at a radius of 3mm as depicted in Figure B.1. Generally it can be seen that with increasing strain an alignment and fragmentation of the microstructure takes place. At small strains, as shown here in Figure B.3b corresponding to an equivalent strain of 2, an alignment into the shear direction emerges. (The shear direction is parallel to the longitudinal sides of the pictures). At higher strains, Figure B.3c, a full alignment into the shear direction is reached and furthermore a fragmentation of the bainitic sheaves is already visible at this low magnifications. However larger strains as shown in Figure B.3d do not seem to lead to a further refinement of the structure.

Another microstructural aspect is presented in Figure B.4, which shows X-ray scans regarding the retained austenite content. The dotted lines beneath the individual peaks represent fcc peaks, the thick lines bcc iron peaks. Figure B.4a shows the profile of the undeformed carbide-free steel (quality 1). The calculated austenite content was approximately 16 percent. After an equivalent strain of ϵ_{vM} =1 the entire austenite has transformed into martensite (Figure B.4b).

B.5 Mechanical measurements

In Figure B.5a the measured torque during HPT-deformation as a function of the applied strain is plotted. In order to compare the hardening behavior of carbide-free rail steels with other materials the pure metal Armco-iron and as a representative for pearlitic rail steels a R260 (S900A) sample were deformed.

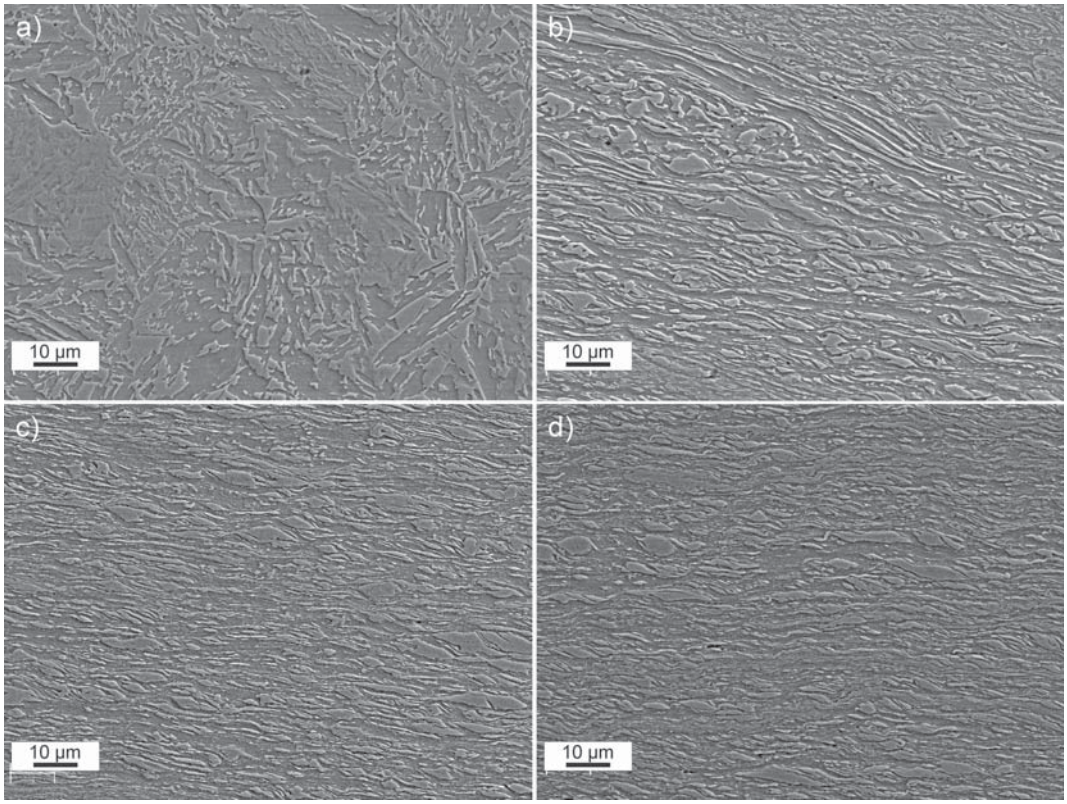

Figure B.3 SEM-images showing the microstructural evolution of a carbide-free bainitic steel (quality 1) as a function of strain. A strong alignment and refinement of the structure with increasing strain is visible.

It should be noted that the samples were not all deformed at the same nominal pressure. Armco iron was deformed at a nominal force of 25 tons, the carbide-free bainitic steels at 32 tons and the pearlitic steel R260 (S900A) at 40 tons. The effect of different pressures is that the friction force arising from the burr between the anvils is different, however this should not have an effect on the shape of the curve, i.e. the hardening behavior. It only affects the absolute value of torque. As visible in Figure B.5a at the beginning of the deformation process all samples pass through a strong hardening region, since there is a strong increase of the torque. Microstructurally, there is a heavy refinement of the structure. In the case of a pure metal (Armco-iron) after a certain amount of strain a saturation of strain hardening takes place. This means that there is no additional increase of torque with increasing strain. As shown in previous studies [6] this can be related to a steady state flow of the material, where no further refinement of the microstructure occurs. In contrast to this behavior the pearlitic steel shows a continuing hardening. This can be attributed to an ongoing process of fragmentation of the pearlitic structure [8]. This signifies principally that the cementite lamellae or in other words the carbides are more and more elongated and ruptured into smaller fragments. The hardening behavior of the carbide-free

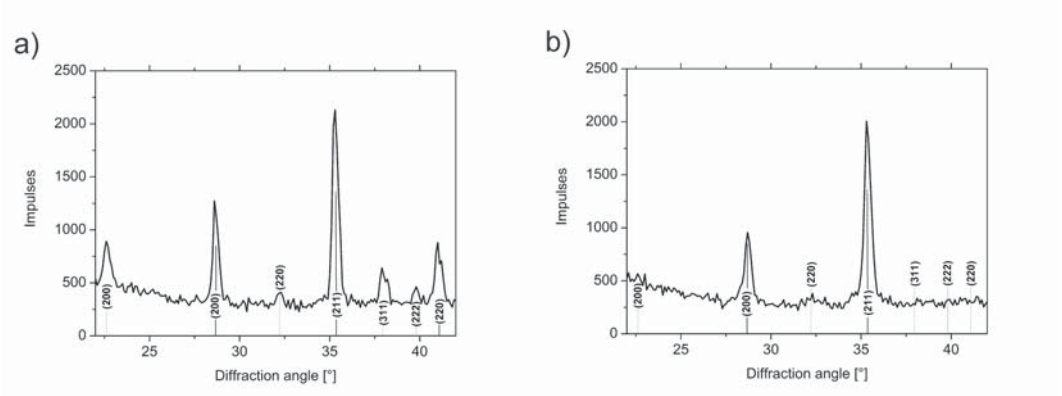

Figure B.4 X-ray diffraction scan comparing the austenite content of the starting material before deformation (a) and after an equivalent strain of 1 (b).

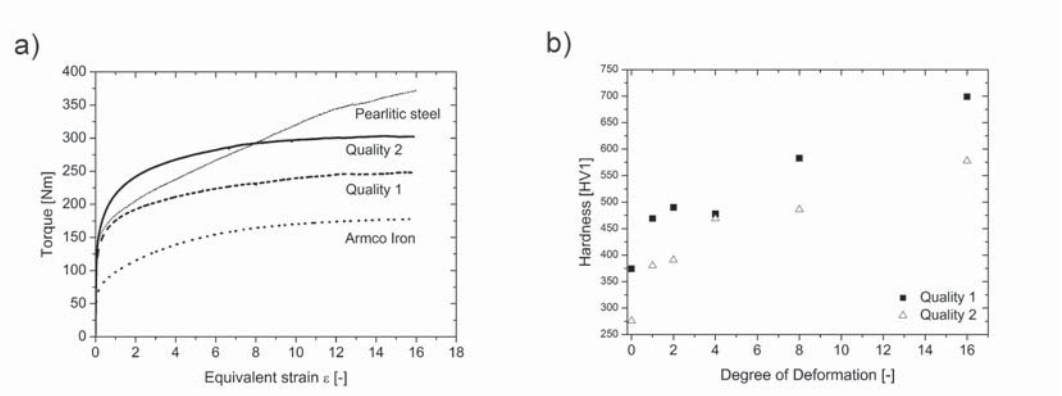

Figure B.5 (a) In-situ torque measurements of different rail steels and a pure metal for comparison. (b) Changes in microhardness due to severe plastic deformation.

qualities lies between Armco and the pearlitic steel. Comparable to a pure metal a strong hardening appears at the beginning which passes into a saturated torque region after strains of about 8. The carbide-free bainitic steel quality 2 has a higher saturation torque than quality 1 due to a higher refinement which has its origin in the finer starting material. However, considering the microhardness, Figure B.5b, there is a further hardening, though, where in both cases an increase in hardness of a approximate factor of 2.5 was found.

B.6 Concluding remarks

Possible microstructural reasons for differences in the hardening behavior at large strains between the pearlitic and the carbide free bainitic steel are shown in Figure B.6. Figures B.6a and b show the microstructure of the pearlitic steel quality R260 at measured strains of 8 and 16, respectively. It can be seen that between strains

of 8 and 16 additional refinement and fragmentation of the pearlitic structure still occurs, therefore there is also still an increase of measured torque during the HPT experiment. In contrast to this in the case of the carbide-free steels, here shown again for quality 1, no further changes in the structure are obvious between an equivalent strain of 8 (Figure B.6c) and 16 (Figure B.6d). In both cases martensitic pools are embedded into an iron matrix. The martensitic structure could not be resolved in the micrographs, however the X-ray measurements showed that the retained austenite is already transformed into martensite after equivalent strains of 1.

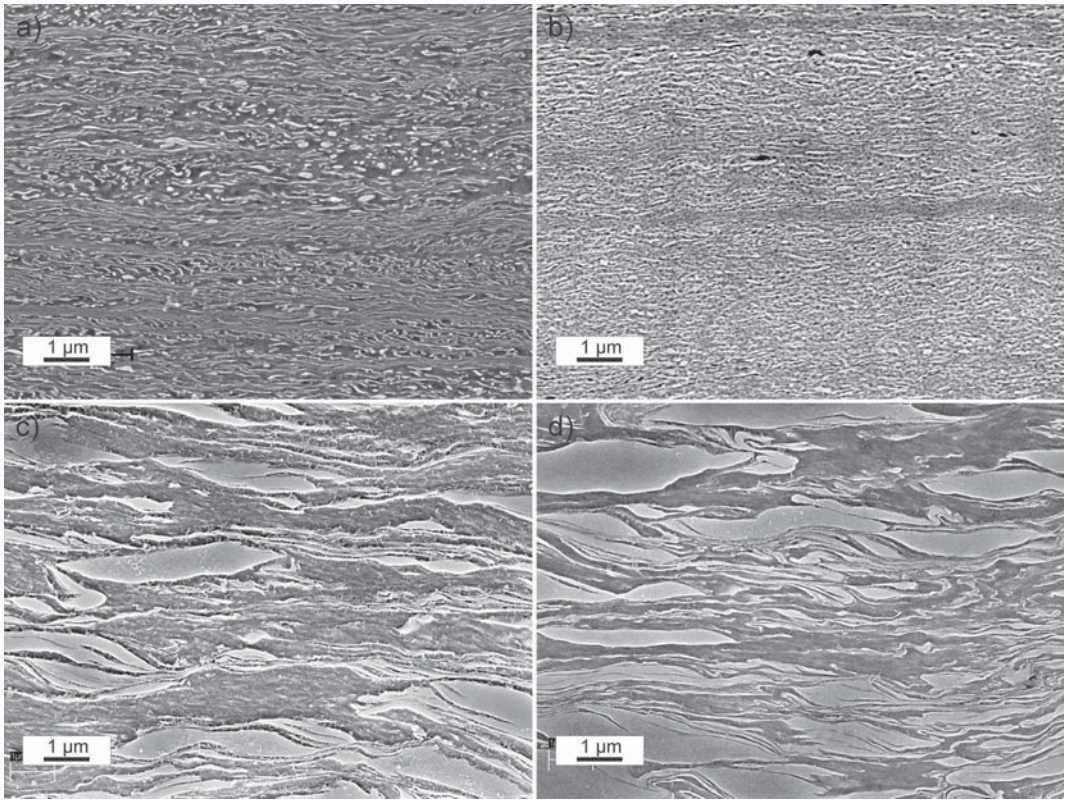

Figure B.6 Comparison of the microstructure of a pearlitic (a,b) and a carbide-free bainitic rail steel quality (c,d) at high strains of $\epsilon_{\mathrm{vM}} = 8$ and $\epsilon_{\mathrm{vM}} = 16$, taken at the same magnification

In the micrographs it seems that these martensitic pools flow within the bcc-iron matrix. This is supported by the fact that the torque-measurements show a hardening behavior which is typical for single phase materials as shown, for example by iron. That means that the deformation is mainly controlled by the bcc-matrix. Taking this fact into account there is no further fragmentation of the martensitic pools and the microstructure remains fairly coarse. However in both cases the microstructure is fully aligned into the shear direction. The microstructural features of the carbide-free rail steels remain in the dimension of microns whereas in the case of the pearlitic quality a nanocrystalline composite emerges. This difference could

have a strong effect on the anisotropy of mechanical features like tensile strength and fracture toughness.

Bibliography to paper B

[1] W. Lojkowski, M. Djahanbakhsh, G. Brkle et al.: Mater. Sci. Eng. A Vol. 303 (2001), p. 197-208.

[2] J.H. Beynon, J.E. Garnham, K.J. Sawley: Wear Vol. 192 (1996), p. 94-111.

[3] R. Z. Valiev, R.K. Isamgliev, I.V. Alexandrov: Prog. Mater. Sci. 45 (2000), p.103-189.

[4] M.A. Meyers, A. Mishra, D.J. Benson: Prog. Mater. Sci. 51 (2006), p. 427-556.

[5] A. Vorhauer, R. Pippan: Scr. Mater. Vol. 51 (2004), p. 921-925.

[6] F. Wetscher, A. Vorhauer, R. Pippan: Mater. Sci. Eng. A Vol. 410 (2005) 213-216.

[7] H.K.D.H. Badeshia: Bainite in Steels, Transformations, Microstructure and Properties (IOM Communications LTD, England 2001).

[8] F. Wetscher, A. Vorhauer, R. Stock, R. Pippan: Mater. Sci. Eng. A Vol. 387-389 (2004), p.809 - 816.

C

Anisotropic fracture behavior of ultrafine-grained iron

A. Hohenwarter[a,b] and R. Pippan[a,b]

[a]Erich Schmid Institute of Materials Science, Austrian Academy of Sciences, A-8700 Leoben, Austria
[b]CD-Laboratory for Local Analysis of Deformation and Fracture, A-8700 Leoben, Austria

Abstract

Fracture toughness measurements with ultrafine-grained bcc iron produced by High Pressure Torsion (HPT) are reported. The measurements were performed with respect to three different crack plane orientations, which showed pronounced differences in fracture toughness as well as in the appearance of the fracture surfaces. The mechanical anisotropy was found to be a result of the elongated and aligned submicrocrystalline microstructure. This causes intergranular fracture for the crack plane orientation of lowest toughness, simultaneously favoring a higher fracture toughness for the other specimen orientations. Since this mechanical anisotropy led to one crack plane orientation with a limited fracture toughness, a strategy for increasing the fracture toughness of this orientation is also presented.

C.1 Introduction

Different severe plastic deformation (SPD) techniques are nowadays widespread for the production of ultrafine-grained (UFG) and nanocrystalline (NC) metals. In the last years the benefits of this material class, such as the enhanced strength, have been published in a vast number of publications and summarized in various overview articles [1–3]. Although grain refinement through SPD generally leads to an increase in strength and hardness, the deformation behavior is often deteriorated due to a strongly diminished dislocation storage ability and mobility associated with grain sizes typically smaller than 1 μm. For that reason the ductility of this material class and strategies for improving the ductility are currently of great interest [4–6].

Besides investigating the ductility with tensile tests, measuring for example the total or uniform elongation, the fracture toughness of a material can provide a more general insight into the deformation and fracture behavior of a bulk material. Since fracture toughness gives information about the damage tolerance of a material it is of great concern for different structural applications, such as in the aviation industry. Due to the small material quantities and dimensions obtained by most SPD processes, especially in the case of HPT, it is often difficult to conduct fracture toughness tests with reference to general standards, such as the ASTM standards. The compliance with such standards is of great importance, especially when the validity of the measurements is based on fulfilling small scale yielding conditions. This would finally also allow a better fracture behaviour comparison of SPD materials with conventional alloys available on the market. Due to the restricted sample dimensions of SPD-processed materials there are only few references in the literature dealing with specific fracture values, such as the plain strain fracture toughness K_{IC} or the J-Integral, see, e.g. [7–9]. A significant increase in the size of HPT samples, as reported in [10], motivated to extend material testing of HPT-deformed materials to fracture toughness experiments. The increase in thickness of the HPT samples also allows the influence of the crack plane orientation on the fracture toughness of HPT-processed materials to be studied.

The aim of this paper is to give new insights into the mechanical properties of UFG iron as a representative for bcc metals. This paper covers the fracture behavior of UFG iron as a function of different crack plane orientations and also presents a method for improving the fracture toughness in the crack plane orientation of lowest toughness.

C.2 Experimental

The composition of ARMCO-iron used in this study is 0.009 wt% C, 0.060 wt% Mn, 0.009 wt% P, 0.007 wt% S and the balance Fe. For the investigations HPT discs of ARMCO-iron with a diameter of 30 mm and a thickness of 9 mm were machined from a rod and annealed at 800 °C for one hour. The samples were then subjected to HPT at room temperature at a nominal pressure of 2.8 GPa up to 10

revolutions, which is equivalent to a von Mises strain, ϵ_{vM}, of ∼80 at a radius of 15 mm. Compact-tension (CT) specimens were then machined from the HPT disc with different crack plane orientations. The specimen orientations and positions of the single specimens in the HPT disc are illustrated in Figure C.1. The specimen denomination is named after the expected crack propagation direction where the different directions are parallel to the chosen coordinate system, as displayed in Figure C.1. The axes are denoted as the tangential direction (TD), radial direction (RD), axial direction (AD), which results in a tangential (TO), radial (RO) and axial (AO) specimen orientation.

Specimens with a tangential and axial orientation were taken from different disc radii, approximately 13, 10 and 7 mm, which is also illustrated for specimens with a tangential orientation in Figure C.1. These radii refer to the middle of each specimen, respectively. For the radial specimen orientation the crack tip was situated at a radius of 10.5 mm.

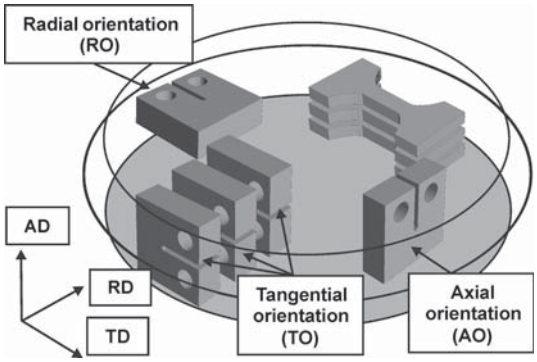

Figure C.1 Schematic representation of the specimens for fracture toughness and tensile tests and their orientation in the HPT disc. The denominations of the specimens is given after the desired crack propagation direction parallel to the chosen coordinate system: the radial orientation (RO), the axial orientation (AO) and the tangential specimen orientation (TO) were investigated.

The geometry of the specimens, the measurement procedure and the calculation of the fracture toughness was based on the requirements and recommendations of the ASTM standard E-399. The specimens had a width, W, of 5.2 mm, an initial crack length, a, of ∼2.6 mm and a thickness, B, of 2.6 mm. The fatigue pre-crack was introduced under cyclic compression loading [11].

Additionally, 3 tensile tests were conducted. The tensile specimens had a gauge length of 2.5 mm that was parallel to the tangential direction, see Figure C.1, and a cross-section of approximately 0.75 mm^2. The specimens were taken along the axial direction from +1, 0 and -1 mm with reference to the middle plane of the former HPT disc (Figure C.1). The middle of the specimen gauge corresponds to a radius of 10 mm in the HPT sample. Both the fracture toughness and tensile

tests were conducted on a testing machine from Kammrath and Weiss at a constant cross-head speed of 2.5 μm/s. For the fracture tests, the specimen displacement was recorded with a strain gauge named DD1 from Hottinger Baldwin Messtechnik (HBM). The microstructure and the fracture surfaces were characterized with a Zeiss 1525 scanning electron microscope (SEM). Micro-hardness measurements in the middle plane of the HPT disc along the radius were also performed to confirm the homogeneity of hardness after HPT processing. The measurements were performed with a Vickers indenter and a load of 200 gf. For each data point 3 indents were made at equivalent geometrical positions and averaged.

C.3 Results

C.3.1 Microstructure

In Figure C.2a a SEM-image taken with back scatter electron (BSE) contrast of the typical saturation microstructure of SPD-iron, looking into the radial direction, is presented.

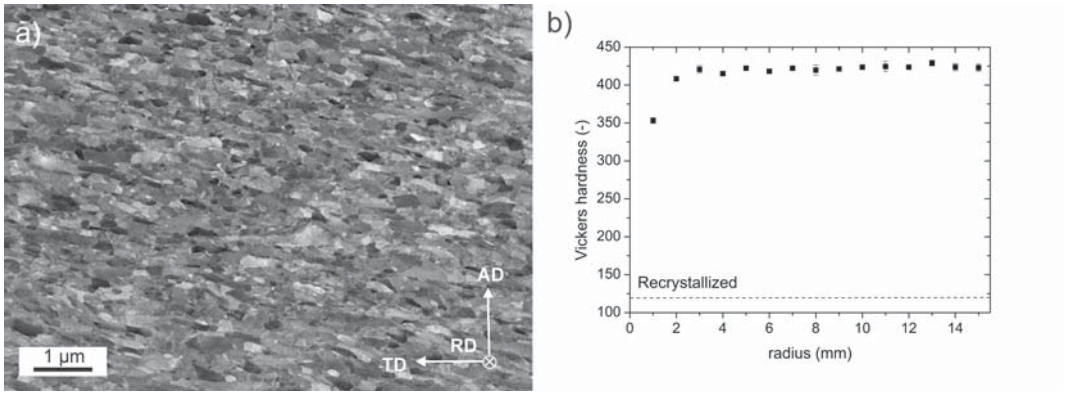

Figure C.2 Features of the investigated material. (a) Typical ultrafine-grained microstructure of iron looking in the radial direction, note the $\sim 10^{\circ}$ inclination of elongated grains to the tangential direction. (b) Hardness plot along the radius of the HPT disc in the middle plane of the disc, showing a pronounced homogeneity of the hardness. The standard deviation as an error bar is only visible for deviations larger than the symbol.

Various features of UFG iron have already been discussed in other references [12–14], however, some features are crucial for the findings presented here and thus some of them are presented and discussed already again here. After reaching a saturation strain, which for iron deformed at room temperature is after an equivalent von Mises strain, ϵ_{vM}, of $\sim$16, a minimum mean grain size of about 200 nm evolves and the grains exhibit an elongated structure with an aspect ratio of $\sim$4 at room temperature, referring to measurements in reference [13]. A steady state in grain size is reached at which larger deformation strains do not lead to a further

grain refinement. Another feature typical of the radial viewing direction is that the microstructure is not fully aligned along the tangential shear direction, which is parallel to the long margins of Figure C.2a, but shows an inclination of about 10° with respect to the tangential direction.

The aforementioned saturation strain is also significant for reaching a pronounced homogeneity within the HPT disc, which is important for the later tensile and CT-specimen extraction. In this work, hardness measurements along the middle plane of the HPT disc after deformation, presented in Figure C.2b, were performed to evaluate the microstructural homogeneity throughout the HPT disc. The occurrence and requirements for a homogenous microstructure in HPT discs have been discussed in [15,16]. In Figure C.2b the plateau of hardness starts at a radius of approximately 3 mm, which corresponds to an equivalent strain, ϵ_{vM}, of 16 after 10 rotations. At larger radii a homogenous hardness of about 420 HV is reached, indicating a fairly constant grain size in this area. The reason for the homogeneity is again the occurrence of a lower limit of grain refinement after reaching a saturation strain. The hardness of the recrystallized material prior to deformation is indicated with a dashed line. The value of 120 HV corresponds to a starting grain size of $\sim$60 μm.

C.3.2 Tensile tests

In order to give a full overview on the fracture behavior of UFG bcc iron, tensile tests studying the deformation behavior under uniaxial tension were performed in addition to the fracture toughness testing. The average ultimate tensile strength (UTS) of the three measurements was found to be 1616 MPa with a standard deviation of 12 MPa.

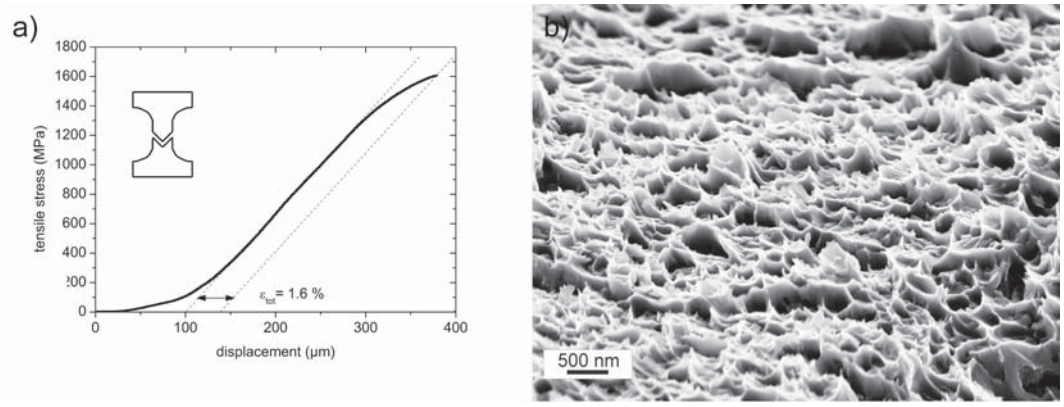

Figure C.3 Deformation behavior under uniaxial tension. (a) Representative stress-displacement curve of ultrafine-grained iron. (b) Fracture appearance of the tensile specimen showing a dimpled fracture surface.

In Figure C.3a the stress-displacement curve* of a HPT-deformed iron tensile specimen taken from the middle plane is presented. Although the ultimate tensile strength is fairly high with a value of 1610 MPa, the material has a diminished ductility with a total elongation to fracture of about 1.6 % as calculated from the gauge length and the measured displacement to failure. An inspection of the fracture surfaces shows that macroscopically the specimen fails through shear fracture under about 45° along two conjugate directions parallel to the directions of maximum shear stress under uniaxial tension. Microscopically, the fracture surface exhibits a shallow dimple structure, as presented in a SEM micrograph (Figure C.3b)

The deformation behavior of UFG iron has also been studied in [17–19]. Similar to our findings Panin et al. [19] found an elongated grain structure after subjecting the material to ECAP via route A, which can be compared with monotonic HPT deformation. The aligned microstructure combined with the strongly reduced work hardening capacity due to the SPD process favored a strong shear localization in the direction of maximum shear stress under uniaxial tension. The shear bands were either parallel to each other or were located along conjugate directions of maximum tangential stress. The second case was also found in this study and displayed in Figure C.3a in the schematic drawing. Due to the prevailing localized deformation through shear band formation and crack propagation in the shear bands, the ductility of UFG iron is generally low under uniaxial tension. Simultaneously, on the microscopical level, see Figure C.3b, microductile fracture occurs.

C.3.3 Fracture toughness measurements

A requirement for the fracture toughness measurements was that the crack tip for the different orientations be within an area of constant mechanical properties in all following fracture experiments. This was evaluated, as presented before but not mentioned explicitly, for the radial direction with hardness measurements along the radius of the disc that showed a plateau in hardness starting from a radius of 3 mm. The tensile tests showed for all 3 tensile tests, taken from different axial positions, a fairly uniform strength with a low standard deviation. That indicates also homogeneity of the mechanical properties through the thickness of the HPT specimen in the investigated area. This confirms that the crack tips considering the different CT-specimen orientations are in an area of a homogenous microstructure.

Figure C.4a presents the results of the fracture toughness measurements for the different specimen orientations. For each data point three measurements were performed and averaged. The error bars indicate the standard deviation and the number in the brackets gives the average value of the fracture toughness. Detailed information of the results is given in Table C.1. In the case of the tangential specimen orientation the measurements were performed at different radii of the HPT disc, namely R ∼13, 10 and 7 mm. As Figure C.4a shows, the fracture toughness remains

* The different slope at the beginning of the elastic regime of the stress-displacement curve is due to an unsatisfactory alignment of the dog-bone specimen at the beginning of the test and not because of a different hardening behavior

fairly constant for the different radii ranging from average values of 15.1±2.4 MPa $m^{1/2}$ for a radius of 13 mm to 13.6 ±1.6 MPa $m^{1/2}$ at a radius of 7 mm for samples deformed to the saturation stage. An inspection of the cracked samples showed that the cracks in these specimens deflected about 10° with respect to the expected Mode I propagation direction.

For the axial specimen orientation only a single specimen was tested at every radius since the tangential oriented specimens showed no distinctive radial dependency of the fracture toughness. Here a fracture toughness with a mean value of 36.2±6.2 MPa $m^{1/2}$ was measured. Specimens with an axial orientation showed that the crack propagated almost perpendicular to the expected Mode I propagation direction. This is simultaneously the same crack propagation direction as for the tangential oriented specimens. Since for a real Mode I crack propagation the fracture load would be even higher the measured values can be regarded as a lower bound.

For the radial specimen orientation the largest fracture toughness was determined with a mean value of 49±4.8 MPa $m^{1/2}$, however this value is no longer valid according to the ASTM E-399 standard because of insufficient specimen dimensions in relation to the measured fracture toughness. Depite that it can be seen as an estimate as a lower limit for the fracture toughness, which reflects the enormous difference in the fracture behavior and toughness compared to the tangential and axial specimen orientation.

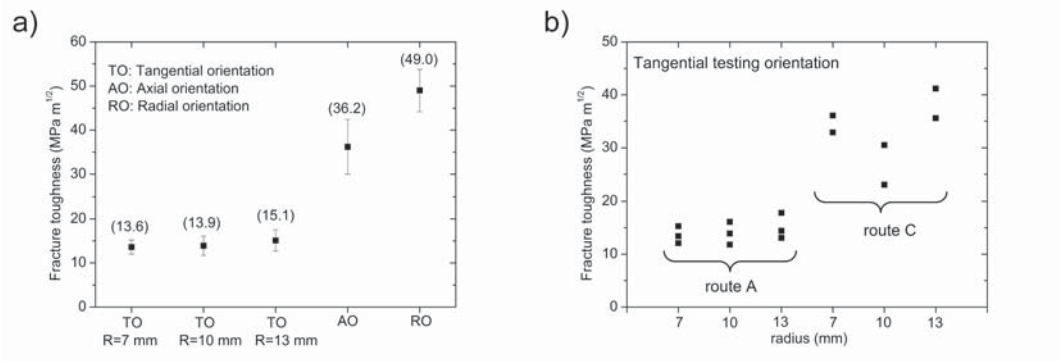

Figure C.4 Summary of the fracture toughness measurements. (a) Results for the tangential orientation (TO) where specimens were taken from different radii and results for the axial (AO) and radial orientation (RO). (b) Comparison of the toughness between route A and route C showing a marked increase in toughness for processing by route C.

In a further set of experiments 2 specimens each from different extraction radii with a tangential specimen orientation were tested, however, they were pre-deformed differently. The HPT specimen was also monotonically deformed up to 10 rotations but additionally subjected to a further deformation step in which the specimen was rotated for a third of a full rotation in the opposite direction with respect to the

Table C.1 Summary of the results of the fracture toughness tests

Specimen	R [mm]	$\frac{Pmax}{Pmin}$	K_{IC} [MPa $m^{1/2}$]	Specimen	R[mm]	$\frac{Pmax}{Pmin}$	K_{IC} [MPa $m^{1/2}$]
Tangential	13	1	17.8	Axial	13	1	41.8
Orientation		1	14.4	Orientation	10	1.19	29.5
		1	13.1		7	1.58	37.4
Tangential	10	1	16.1	Radial	10.5	1.23	44.3
Orientation		1.09	11.8	Orientation	10.5	1.08	53.9
		1	13.9		10.5	1.21	48.8
Tangential	7	1	13.4	Tangential	13	1.42	41.2
Orientation		1	12.1	Orientation	10	1.29	30.5
		1	15.3	Route C	7	1.29	36.1
					13	1.29	35.6
					10	1	23.0
					7	1	32.9

R, radius of specimen extraction;P_{max}/P_Q ratio of maximal force P_{max} and the calculated value P_Q using the 5% secant deviation procedure according to ASTM E-399.

former rotation direction. This type of deformation path will be called Route C†. The classic HPT deformation in one direction for 10 rotations will be denoted as Route A. Similar cyclic deformation concepts were investigated for example in [20, 21].

In Figure C.4b a comparison of the fracture toughness results for route A and route C is presented. For both deformation routes the individual data points are displayed, further information is given in Table C.1 again. A marked increase in the fracture toughness was found for processing by route C. Considering that there was no influence from the specimen position on the fracture toughness found and taking the average value of all measurements for the different deformation routes into account an improvement from 14.2±1.9 MPa $m^{1/2}$ for route A to 33.2±6.2 MPa $m^{1/2}$ for route C was found.

C.3.4 Fractography

In Figure C.5a a representative fracture surface for a specimen with a tangential crack orientation is presented at low magnification. The dashed line indicates the transition from the fatigue pre-crack to the overload fracture surface for better visualization. The fracture appearance is brittle, no significant indicators for plastic deformation during fracture, for example dimple formation, can be found. Only some steps and ledges, indicated with arrows, can be found. In a more detailed micrograph, Figure C.5b, a granular structure is visible, which originates from the submicrocrystalline grain structure, indicating intercrystalline fracture.

† These denominations are given on the basis of the denominations for different Equal Channel Angular Pressing (ECAP) routes. However regarding ECAP every single deformation step delivers the same nominal amount of strain, which is not the case here.

The microscopic fracture appearance for the axial specimen orientation is the same as for the tangential orientation except the deviation between the expected and observed macroscopic crack propagation direction. Further fractographs are therefore not shown but brittle intercrystalline fracture occurred. The crack, as mentioned before, propagated almost perpendicular to the expected Mode-I crack propagation direction. The resulting crack propagation direction is the same as for specimens with a tangential specimen orientation, which showed intercrystalline fracture.

A completely different type of fracture morphology was found for specimens tested with a radial orientation. Figure C.5c shows the fracture surface for the radial orientation at low magnifications. The fracture surface shows delaminations, which are parallel to the radial direction and start from the fatigue pre-crack. Further features can be found at higher magnifications, Figure C.5d. The fracture appearance is ductile revealing a submicrocrystalline dimple structure.

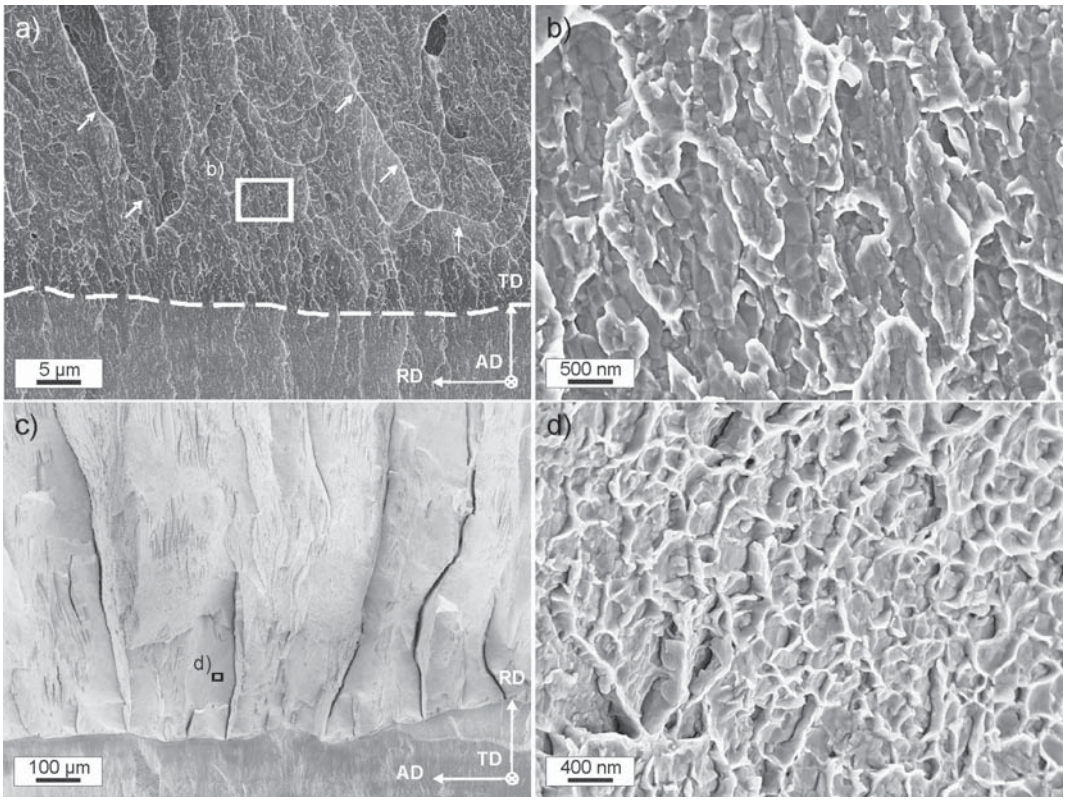

Figure C.5 Fractographs of representative fracture surfaces of specimens with tangential (a and b) and radial specimen (c and d) orientations. (a) Overview revealing brittle fracture appearance with almost no plastic deformation (Dashed line indicates the transition from the fatigue pre-crack to the overload fracture surface). (b) Detailed view displaying grain boundary fracture. (c) Overview of the fracture surface of the radial specimen orientation, displaying various material delaminations. (d) Ductile fracture appearance and dimple structure visible at high magnifications.

C.4 Discussion

C.4.1 Anisotropy of the fracture toughness

Tangential specimen orientation

Regarding the tangential specimen orientation, where the specimens were taken from different radii, no distinctive dependency of the fracture toughness on the position of extraction from the HPT disc was found, see Figure C.4a. This is consistent with the hardness showing a pronounced homogeneity throughout the disc once a steady state in grain refinement is reached. Both mechanical values prove that HPT can produce mechanically homogenous materials.

An inspection of the specimens after fracture showed that the crack emanating from the notch propagates not strictly in a Mode I manner, but under an inclination of about 10° to the expected Mode I direction, illustrated in the schematic CT-specimen in Figure C.6a.

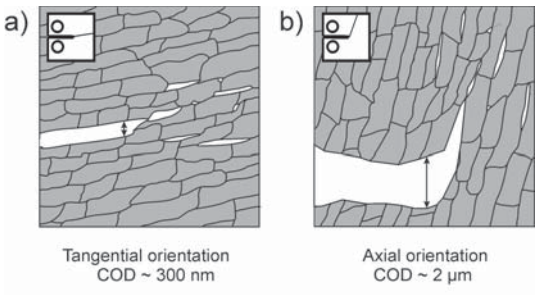

Figure C.6 Schematic comparison of the fracture processes in SPD iron regarding two different crack propagation directions. (a) The tangential specimen orientation, showing intercrystalline fracture and possible nanovoid and nanocrack formation ahead of the crack tip. (b) Axial specimen orientation showing the same fracture process but with additional crack deflection into the direction of lower crack resistance.

The crack propagation direction is therefore macroscopically the same as the grain alignment of the grains on the microscopic level, Figure C.2a. Additionally in Figure C.5b the granular fracture appearance in this testing direction is visible, however no distinctive features for trans- or intercrystalline fracture can be seen. The fact that the crack follows the aligned and inclined microstructure leads to the conclusion that intercrystalline fracture occurs.

Experimental findings on intercrystalline fracture of UFG bcc iron have not yet been reported in the literature. The deformation behavior of UFG iron has only been experimentally assessed by uniaxial tensile or compression testing [17–19]. These studies showed that, as in the present experiment UFG iron fails through shear band formation and localization under uniaxial loading. These experiments do not regard the same stress state as in a fracture mechanics experiment, notably having a large amount of tensile triaxiality ahead of the crack tip, and are therefore not comparable to these fracture experiments.

However, atomistic simulations dealing with the deformation behavior of bcc metals are available. These show a similar picture to our experimental findings, although they exist only for grain sizes in the nanometer-regime [22–24]. Latapie et al. [24] found in their investigations that the fracture process was characterized by the formation of nanovoids and cracks ahead of the crack tip. They coalesce with the main crack with increasing loading and build an intercrystalline crack path.

A further insight into the present intercrystalline fracture process can be obtained by considering the crack tip opening displacement *(CTOD)* [25]:

$$CTOD = m\frac{K^2}{\sigma_{\mathrm{y}}E} \tag{C.1}$$

By inserting for SPD-iron a yield strength, σ_{y}, of 1400 MPa, derived from the hardness, an average fracture toughness, $\mathrm{K_{IC}}$, for the tangential specimen orientation of 14.2 $\mathrm{MPam^{1/2}}$ and a typical factor, m, of 0.5 for plane strain conditions a *CTOD* of about 340 nm can be calculated. This critical *CTOD* is larger than the mean grain size of about 200 nm. In contrast to this result the fractograph in Figure C.7a, displaying the transition from fatigue pre-crack to the overload fracture, suggests that the critical *CTOD* is not larger than the grain size as the transition area is very smooth and no stretched zone can be found. Thus additional toughening mechanisms have to contribute in order to realize the calculated *CTOD* and the relatively large mean fracture toughness of 14.2 MPa $\mathrm{m^{1/2}}$ despite the apparently brittle intercrystalline fracture.

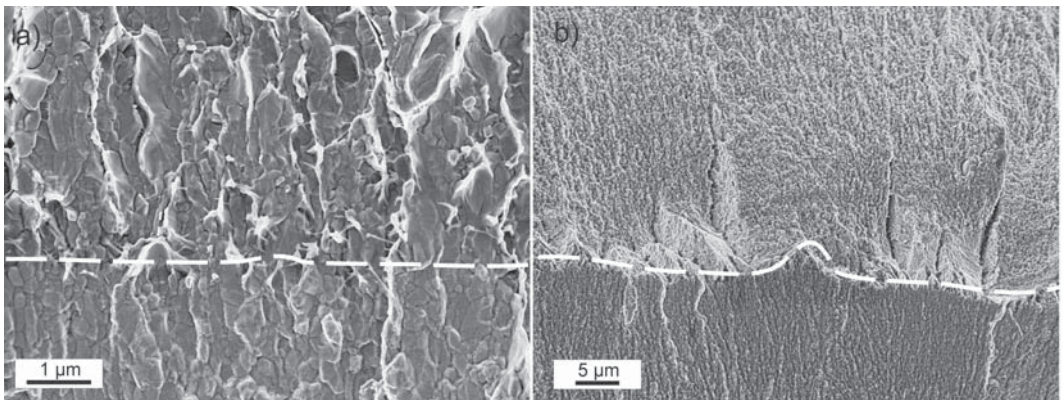

Figure C.7 Detailed fractographs displaying the transition from the fatigue pre-crack to the overload fracture for (a) the tangential specimen orientation. (b) Fractograph of a specimen with a radial specimen orientation, loaded with a $\mathrm{K_{max}}$ of 43 $\mathrm{MPam^{1/2}}$ leading to the first delaminations and finally, fractured through cyclic loading. In both cases the dashed line separates the fatigue pre-crack surface from the residual fracture surface.

One contribution to the fracture toughness and hence to the calculated *CTOD* can be found in Figure C.5a. There a certain step structure, indicated with arrows, is visible. These steps and ledges emerge during the fracture process when the crack

front is located on slightly different planes or heights. The remaining bridges between the different crack planes shear off plastically during the ongoing crack propagation and form finally these steps. These shear processes contribute to the critical *CTOD* and so to the fracture toughness.

A further contribution can be inferred from Figure C.7a. It shows that cleavage fracture is also the dominant crack propagation mechanism acting in the formation of the fatigue pre-crack, which is located in the lower part of the picture. Generally plastification of the crack tip is essential for the formation of the fatigue pre-crack [26]. Since this plastification leads to intercrystalline fracture plastic deformation must also be involved in the intercrystalline cleaving process of the overload fracture. This plastic deformation also contributes to the fracture toughness.

The plastic deformation of the individual grains could also provoke voids ahead of the crack tip, as in the classical case for ductile coarse-grained materials. In contrast to the aforementioned simulations the nanovoid formation can be associated with dislocation activity due to the larger grain size. The voids could lead to the formation of nanocracks and microcracks through convergence along grain boundaries, which coalesce in the vicinity of the crack tip with neighbor grains and finally with the main crack. This proposed fracture process is also schematically depicted in Figure C.6a. The opening of the nano and microcracks contributes to the opening of the crack and gives an additional contribution to the fracture toughness and the critical *CTOD*.

Axial specimen orientation

An increase in the fracture toughness was found for the axial specimen orientation, see Figure C.4a. For the axial orientation the crack propagated macroscopically almost perpendicular to the expected Mode I propagation direction, as illustrated in Figure C.6b in the schematic CT specimen. This strong deviation in crack path leads to the Mode I driving force being approximately halved from its maximum value, corresponding to the straight path [27] valid for a shortly strong kinked pre-crack. This leads to the apparent fracture toughness enhancement compared to the tangential specimen orientation. The measured global toughness must therefore be a lower bound to the true Mode I crack propagation resistance as otherwise the crack would not deflect.

The microstructural reason for the crack deflection can be found in the low fracture toughness of the tangential specimen orientation. It is evident that a Mode I propagation would require either a transcrystalline crack path or a more tortuous intercrystalline crack path, both on account of the elongated grains almost perpendicular to the fatigue pre-crack (Figure C.6b). Both crack paths seem to have a higher fracture resistance. The low fracture resistance of the tangential specimen orientation favors the crack deflection into the direction of the aligned microstructure, again shown in Figure C.6b. The critical *CTOD* for this specimen orientation is about 2.2 μm and therefore much larger than the grain size. In order to realize such a large critical *CTOD*, besides the aforementioned possible microcrack forma-

tion, a plastic shearing at the crack tip must also take place. Table C.1 shows that some measurements showed a large P_{max}/P_Q, which can be related to such large plastic deformation at the crack tip. It may be that some subcritical crack extension enhances this effect, which might be induced by a degree of R-curve behavior of the fracture toughness for this crack propagation direction.

Radial specimen orientation

A further increase of the fracture toughness was found for specimens with a radial specimen orientation, Figure C.4a. In comparison to the tangential orientation an increase by a factor of about 3 was found with a value of 49 ± 4.8 MPa $m^{1/2}$ and a *CTOD* of ∼ 4 μm. The toughening mechanism here can be explained with the features visible on the fracture surface, Figure C.5c and d.

In the case of plain strain conditions the stress state ahead of the crack tip exhibits a pronounced tensile triaxiality. The toughness of materials can be increased through reducing the triaxiality by relaxing one of the normal stresses [28, 29]. As presented in Figure C.5c delaminations can be found on the fracture surface. Delaminations, formed during the fracture process, Figure C.5c, act as internally free surfaces, which reduce the effective thickness of the sample to the distance between two neighbouring delaminations. Regarding the coordinate system in Figure C.5c, the tensile stress component in the axial direction of the HPT sample becomes zero and a plain stress state is generated locally leading to reduced triaxiality and a higher fracture toughness.

The formation of the delaminations was further investigated with the following procedure. A sample was loaded with a K_{max} of 43 MPa $m^{1/2}$, which is about 90% of the evaluated fracture toughness, then unloaded and finally fractured through cyclic loading. In the fractograph, Figure C.7b, the fatigue fracture surface due to pre-cracking is the lower half while the upper part is from final fatigue fracturing. In the middle of the micrograph delaminations can be found, which originate from the monotonic loading step up to a K_{max} of 43 MPa $m^{1/2}$. The appearance of the delaminations show that they are initiated already at lower stress intensities and hence can contribute to an increase in toughness.

A comparison of the coordinate systems in Figure C.5a and c shows that the crack plane of the delaminations and the crack plane of the tangential specimen orientation is the same. In both cases it is normal to the axial direction (AD). Thus the occurrence of the delaminations is promoted by the low fracture toughness of the tangential specimen orientation which is highly sensitive to inclusions as fracture initiation sites or grain boundary cleavage. The high toughness in the radial specimen orientation is therefore a result of the low fracture toughness of the tangential specimen orientation.

Compared with the tangential specimen orientation the fracture appearance also changes on the micro-scale, as presented in Figure C.5d. In contrast to the tangential specimen orientation, a ductile shallow dimple structure with dimples somewhat larger than the grain size can be found. These submicrocrystalline dimples arise

since a plain stress state prevails locally after the formation of delaminations facilitating plastic deformation of volume elements between neighbouring delaminations. The loss of the triaxiality allows local shear deformation. The fracture process is therefore similar to that seen under uniaxial tensile deformation. In both cases the final fracture occurs due to shear localization. However, in a tensile specimen the shear localization causes relatively macroscopic brittle fracture behavior whereas in a fracture toughness sample the shear deformation of the volume elements between delaminations induces the high measured toughness regarding this sample orientation.

C.4.2 A method for improving the fracture toughness

HPT processing by route C increased the fracture toughness for the tangential specimen orientation, see Figure C.4b. Based on a comparison of the fracture surfaces of a specimen processed by route A, Figure C.8a, and route C, Figure C.8b, an explanation for the toughening can be given.

As can be seen the two fracture surfaces differ significantly in their morphology. In Figure C.8b a more tortuous crack path is visible. Additionally a stretched zone and plastic deformation in the form of dimples prior to brittle fracture can be found, which leads to the higher measured values. The microstructural reason for the enhanced toughness, which can be related to the stronger blunting of the crack tip, can be partly derived from an earlier work devoted to cyclic HPT [30] in which ARMCO-iron was cyclically and monotonically deformed. In contrast, in the present work only one further cycle into the reverse deformation direction was performed. The degree of deformation corresponds to equivalent strains ϵ_{vM}, of $\sim$1.2 and $\sim$2.2 for the radii 7 and 13, respectively.

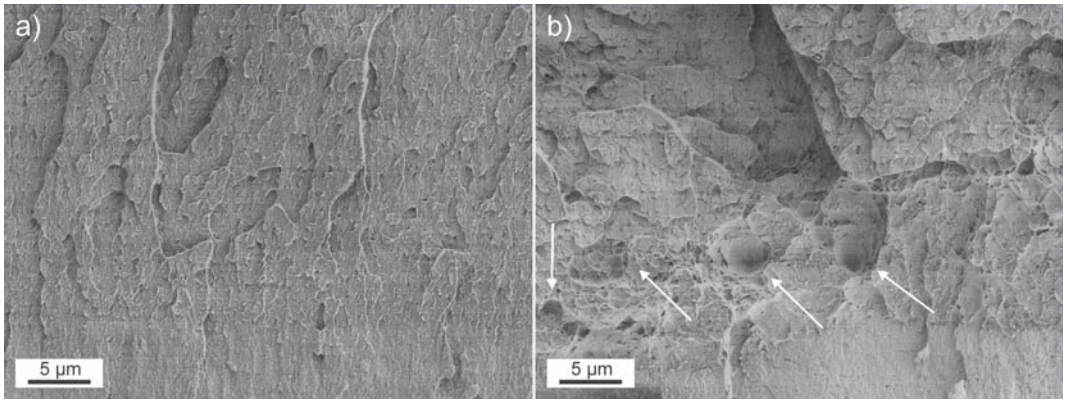

Figure C.8 Comparison of fracture surfaces of specimens with a tangential specimen orientation. (a) monotonic deformed up to 10 revolutions (route A). (b) monotonic deformed up to 10 revolutions + deformed in the reverse deformation direction for 0.3 rotations (route C). A stretched zone and dimples indicated with arrows are visible.

Since it is known that monotonic deformation leads to a preferred alignment of the grain structure, it can be assumed that reverse deformation leads to a realignment of the microstructure into the opposite direction. Since only one cycle was applied, one can assume that no full realignment of the microstructure at a given radius is achieved. Rather an inhomogeneous microstructure consisting of aligned elongated grains, equiaxed grains and again aligned elongated grains, which are already fully aligned into the other deformation direction, will be present.

These considerations are consistent with the fracture surface in Figure C.8b having a much rougher fracture surface as a fracture surface for monotonic HPT-deformed material, Figure C.8a. The mixture of different grain shapes seems to allow a stronger blunting of the crack tip, whereas the stronger plastification is realized by the equiaxed grains, having still a larger potential for plastic deformation, in contrast to the fully aligned grains.

C.5 Conclusions and summary

Within this paper the fracture behavior of a bcc model material, here ARMCO-iron, after being subjected to HPT at room temperature was studied with respect to 3 different crack plane orientations. Based on the results of this study the following new findings can be summarized:

1. The specimen orientation was experimentally found to have a strong effect on the measured fracture toughness. The mechanical anisotropy was reflected by the fracture surface, ranging from brittle to ductile fracture appearances.

2. The pronounced mechanical anisotropy was related to the elongated and aligned grain structure obtained by the HPT deformation process favoring an intercrystalline crack path. This crack path enables the delamination-induced toughening mechanism for the radial specimen orientation and the crack deflection-induced toughening for the axial crack plane orientation.

3. A method for improving the fracture toughness of the most brittle orientation was presented. Through a further sample deformation step a marked increase of the measured fracture toughness was achieved.

These findings show that with an understanding of the toughness anisotropy an unexpectedly good combination of high strength and simultaneously high fracture toughness can be achieved in UFG iron.

Bibliography to paper C

[1] R.Z. Valiev, R.K. Islamgaliev, I.V. Alexandrov, Prog. Mater. Sci. 45 (2000) 103-189.

[2] R.Z. Valiev, T.G. Langdon, Prog. Mater. Sci. 51 (2006) 881-981.

[3] A.P. Zhilyaev, T.G. Langdon, Prog. Mater. Sci. 53 (2008) 893-979.

[4] Y. H. Zhao, et al. Scripta Mater. 59 (2008) 627-630.

[5] I. Sabirov, Y. Estrin, M.R. Barnett, I. Timokhina, P.D. Hodgson, Acta Mater. 56 (2008) 2223-2230.

[6] M. Hockauf, L.W. Meyer, B. Zillmann, M. Hietschold, S. Schulze, L. Krger, Mater. Sci. Eng. A 503 (2009) 167-171.

[7] I. Sabirov, O. Kolednik, R.Z. Valiev, R. Pippan, Acta Mater. 53 (2005) 4919-4930.

[8] F. Wetscher, R. Stock, R. Pippan, Mater. Sci. Eng. A 445-446 (2007) 237-243.

[9] M. Faleschini, H. Kreuzer, D. Kiener, R. Pippan, J. Nuc. Mater. 367-370 (2007) 800-805.

[10] R. Pippan, S. Scheriau, A. Hohenwarter, M. Hafok, Mater. Sci. Forum 584-586 (2008) 16-21.

[11] S. Suresh, Eng. Frac. Mech. 21 (1985) 453-463.

[12] R.Z. Valiev, Y.V. Ivanisenko, E.F. Rauch, B. Baudelet, Acta Mater. 44 (1996) 4705-4712.

[13] A. Vorhauer, R. Pippan, Metall. Mater. Trans. A 39 (2008) 417-429.

[14] F. Wetscher, A. Vorhauer, R. Stock, R. Pippan, Mater. Sci. Eng. A 387-389 (2004) 809-816.

[15] A. Vorhauer, R. Pippan, Scripta Mater. 51 (2004) 921-925.

[16] C. Xu, Z. Horita, T.G. Langdon, Acta Mater. 56 (2008) 5168-5176.

[17] D. Jia, K.T. Ramesh, E. Ma, Acta Mater. 51 (2003) 3495-3509.

[18] M.S. Ryszkowska, T. Wejrzanowski, Z. Pakiela, K.J. Kurzydlowski, Mater. Sci. Eng. A 369 (2004) 151-156.

[19] A.V. Panin, A.A. Panina, Y.F. Ivanov, Mater. Sci. Eng. A 486 (2008) 267-272.

[20] F. Wetscher, B. Tian, R. Stock, R. Pippan, Mater. Sci. Forum 503-504 (2006) 455-460.

[21] M. Kawasaki, T.G. Langdon, Mater. Sci. Eng. A 498 (2008) 341-348.

[22] S.L. Frederiksen, K.W. Jacobsen, J. Schiotz, Acta Mater. 52 (2004) 5019-5029.

[23] D. Farkas, B. Hyde, Nano letters 5 (2005) 2403-2407.

[24] A. Latapie, D. Farkas, Phys. Rev. 69 (2004) 134110-1 - 134110-9.

[25] T. L. Anderson, Fracture Mechanics, CRC Press, Boston, 1991.

[26] R. Pippan, Eng. Frac. Mech. 31 (1988) 715-718.

[27] R. Pippan, Eng. Frac. Mech. 44 (1993) 821-829.

[28] R.W. Hertzberg, Deformation And Fracture Mechanics Of Engineering Materials, 4th ed., John Wiley & Sons Inc., New York , 1996.

[29] R. Song, D. Ponge, D. Raabe, Acta Mater. 53 (2005) 4881-4892.

[30] F. Wetscher, R. Pippan, Phil. Mag. 86 (2006) 5867-5883.

D

Effect of large shear deformations on the fracture behavior of a fully pearlitic steel

A. Hohenwarter[a,b], A. Taylor[a], R.Stock[c] and R. Pippan[a,b]

[a]Erich Schmid Institute of Materials Science, Austrian Academy of Sciences, A-8700 Leoben, Austria
[b]CD-Laboratory for Local Analysis of Deformation and Fracture, A-8700 Leoben, Austria
[c]voestalpine Schienen GmbH, A-8700 Leoben, Austria

Abstract

High Pressure Torsion (HPT) has been used for investigating the influence of pre-deformation on the fracture toughness of a fully pearlitic rail steel. The use of HPT enables one to investigate changes in fracture toughness as a function of pre-deformation over a wide range of strain while simultaneously studying the influence of the crack plane orientation on the fracture toughness. With increasing pre-strain, besides a strong increase in hardness, a pronounced anisotropy in the fracture toughness was found. Both the increase in hardness and the anisotropic fracture behavior can be attributed to the shear deformation process leading to an anisotropic composite structure on the nanometer-scale.

D.1 Introduction

Motivated by the exceptional mechanical and physical properties of ultrafine grained and nanocrystalline materials, Severe Plastic Deformation (SPD) has gained great scientific interest especially in the last years as a route to produce such materials [1–4]. Although this route requires great technical efforts to be taken to synthesize such metals, these materials can also occur unintentionally in different fields, for instance during machining [5], wire drawing [6] and on the surface of rails [7,8]. In the last example, the material changes are promoted during rail-wheel contact due to the loading conditions, which can be characterized by high contact forces and large shear stresses. These contact characteristics lead to strong plastic deformations of the rail surface and often form the initiation point of RCF (Roll Cycle Fatigue) related crack like defects such as head-checks and squats [9, 10]. In general, rail steels are tested regarding their RCF behavior through Two-Disc Roller tests [11,12]. These tests are capable of ranking materials by their crack formation tendency but cannot provide information about the local fracture properties of the strongly plastically deformed surface layers. Classical testing methods for evaluating the fracture properties are not applicable since the thin deformation layers do not meet the basic requirements for further testing. However, the mechanical, in particular the fracture properties of these strongly deformed surface layers would be of great interest in understanding damage development in such materials while also being helpful in future material design strategies.

In this work, High Pressure Torsion (HPT) was used to deform a fully pearlitic rail steel to well-defined degrees of deformation in order to simulate comparable microstructural conditions as also found in rails in service. Then, the fracture toughness of the steel in different crack propagation directions was tested to get an insight into the local fracture properties of a representative rail steel subjected to very large shear deformation strains.

D.2 Experimental

The composition of the pearlitic steel, used in this study, classified as R260 (S900A), is 0.76 wt% C, 0.35 wt% Si, 1 wt% Mn, 0.014 wt% S, 0.017 wt% P and Fe in balance. The material, in the shape of a rail, was provided by voestalpine Schienen GmbH, Leoben, Austria. For the investigations HPT-discs of the pearlitic steel with a diameter of 26 mm and a thickness of 8 mm, were machined from a rod extracted from the rail head along the rolling direction. In order to reduce damage to the HPT anvils the actual samples were embedded in an iron ring, which resulted in a disc diameter of 30 mm. The samples were HPT-deformed at room temperature under a nominal pressure of 5.6 GPa for 1, 2 and 3 revolutions. Compact tension (CT) specimens with three different crack plane orientations were prepared according to ASTM E-399 as shown in Figure D.1. The crack plane orientations of the individual specimens can be described with the chosen coordinate system. For orientation A the

crack propagation direction is parallel to the tangential direction and for orientation B parallel to the axial direction. For orientation C the expected crack extension is parallel to the radial direction.

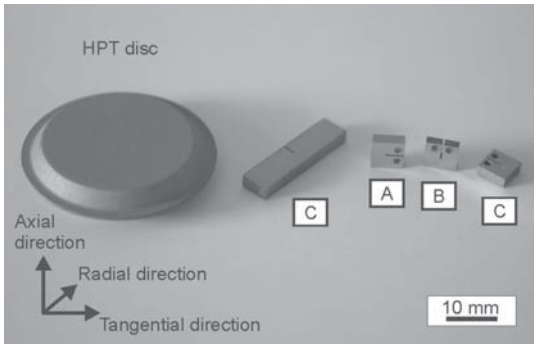

Figure D.1 Representation of the HPT disc, the coordinate system and the differently oriented specimens extracted from the HPT disc.

The degree of pre-deformation of the individual samples was related to the equivalent von Mises strain:

$$\epsilon_{\mathrm{vM}} = \frac{2\pi r n}{t_{\mathrm{m}}\sqrt{3}}. \tag{D.1}$$

Here r is the radius, t the thickness of the HPT disc and n the number of rotations. The CT-specimens had a width, W, of 5.2 mm, an initial crack length, a, of ∼2.6 mm and a thickness, B, of ∼2 mm. Additionally, for orientation C, single edge notched bend (SENB) specimens were produced. The specimens had a width, W, of 6 mm, an initial crack length, a, of ∼3 mm and a thickness, B, of 3 mm. In all specimens a fatigue pre-crack was introduced under cyclic compression-compression loading with stress intensities ranging from 20-40 MPa $\mathrm{m}^{1/2}$, depending on the material hardness. The fracture tests of the CT-specimens were performed on a testing machine from Kammrath and Weiss at a constant cross-head speed of 2.5 μm/s. The tests with the SENB-specimens were done on a Zwick 1382 at the same cross-head speed. Here a potential drop method was used to measure a possible stable crack extension.

The microstructure and the fracture surfaces were characterized with a Zeiss 1525 scanning electron microscope (SEM), further investigations we carried out with a Transmission Electron Microscope (TEM, Philips CM12). Additionally microhardness measurements of the pre-deformed HPT discs along the radius were performed to measure the hardness as a function of applied strain after HPT processing. For each data point 3 indents were made at equivalent geometrical positions and averaged. The measurements were performed with a Vickers indenter and a load of 1000 gf.

D.3 Results

D.3.1 Evolution of the microstructure

In Figure D.2a-d the evolution of the microstructure of the investigated steel looking into the radial direction for distinctive equivalent strains is presented. In Figure D.2a the undeformed pearlitic starting structure consisting of the cementite lamellae embedded in the ferritic matrix is shown. The lamellae are parallel within one pearlitic colony and change their local orientation in neighboring colonies, the lamella spacing is about 200 nm.

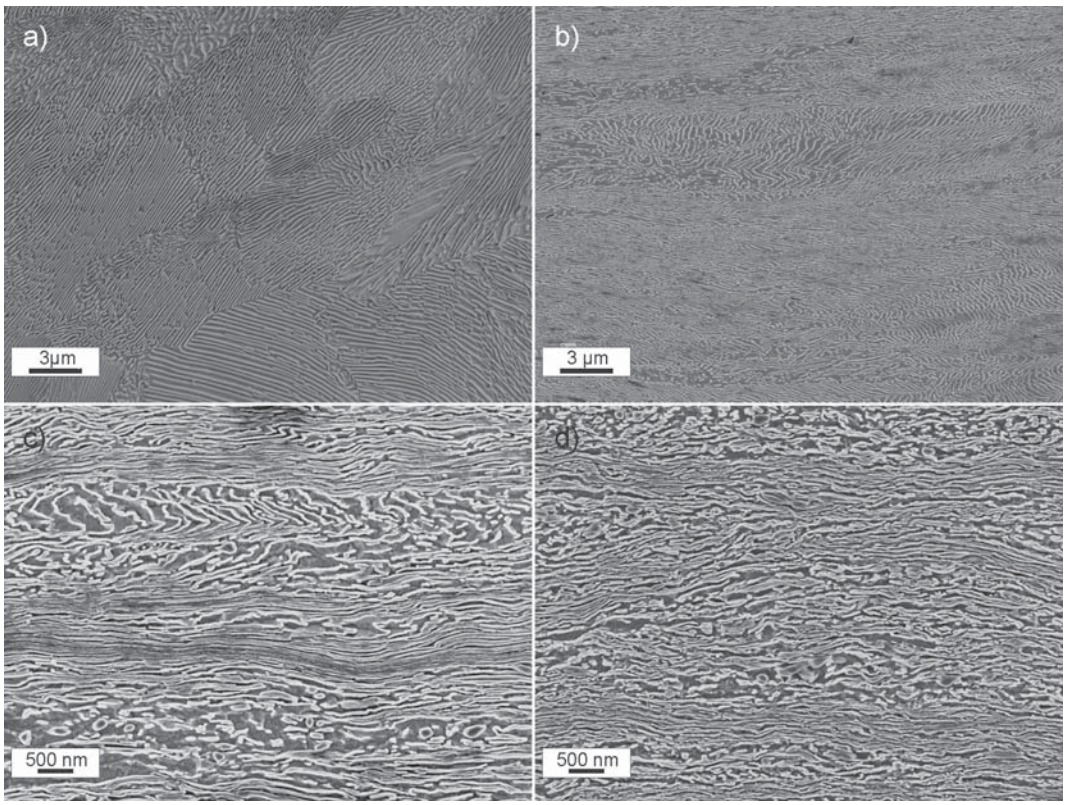

Figure D.2 SEM-micrographs of the investigated material R260 taken at different equivalent strains (a-d) looking into the radial direction. (a) Undeformed starting material, (b) ϵ_{vM}=4, (c) ϵ_{vM}=8, (d) ϵ_{vM}=16.

With increasing strain the lamellae align into the shear direction, which is parallel to the horizontal direction of all micrographs and the lamella spacing is decreased. From the beginning more favorably aligned colonies show a stronger alignment than others, see Figure D.2b. At higher strains, Figure D.2c, the microstructure is almost fully aligned, in only some areas the pearlitic structure is still unaligned. As can also be seen in Figure D.2c the unfavorably aligned lamellae become heavily bent and broken. Finally, at the highest strain investigated with the SEM, $\epsilon_{vM}\sim$16, the

entire pearlitic structure is aligned in the shear direction and the lamellar structure is partly broken up into individual carbides.
In Figure D.3a and b the microstructure after a strain of $\epsilon_{\mathrm{vM}}\sim16$ is presented again with transmission electron microscope (TEM) micrographs using bright field contrast.

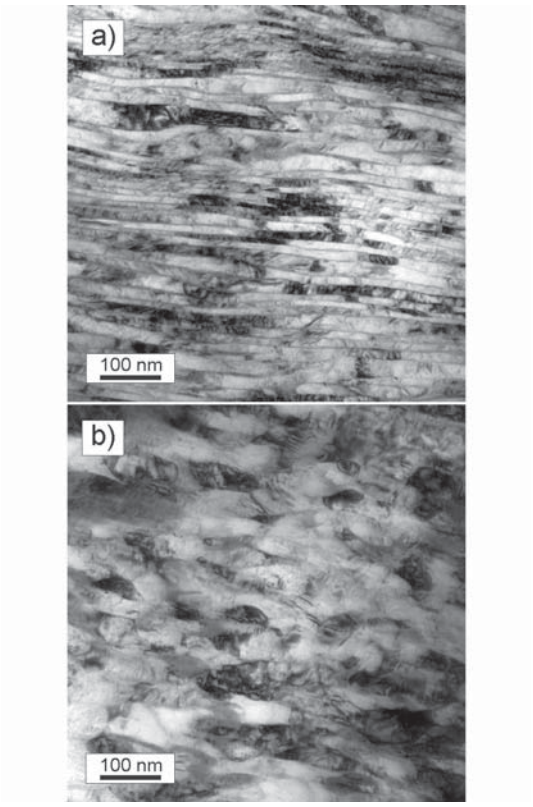

Figure D.3 TEM-micrographs of a sample after straining to ϵ_{vM}=16. (a) Area in which the lamellae are still unbroken and well aligned with an approximate spacing of about 10-15 nm. (b) Region in which the lamellar structure is disrupted and the cementite layers are broken.

In Figure D.3a the lamellar structure is still clearly visible. Here the small lamella spacing of 10-15 nm is more clearly visible than with the Nital-etched SEM specimen in Figure D.2d. However, Figure D.2d also shows there are microstructural regions where the lamellar structure is already broken up into smaller fragments. This description in the lamellar structure can also be seen in the TEM, Figure D.3b. Here the size of the grains is increased in comparison with the grains in the lamellar structure and moves to a more equiaxed structure.

D.3.2 Changes in the hardness

The previously described changes in the microstruture are also reflected in changes of the hardness. In Figure D.4a, the hardness as a function of equivalent strain is plotted. The hardness strongly increases from a value of 276 ±25 HV for the as-received material up to 771 ±10 HV after an equivalent strains of 16, which corresponds to a radius of ∼10.5 mm after 3 turns.

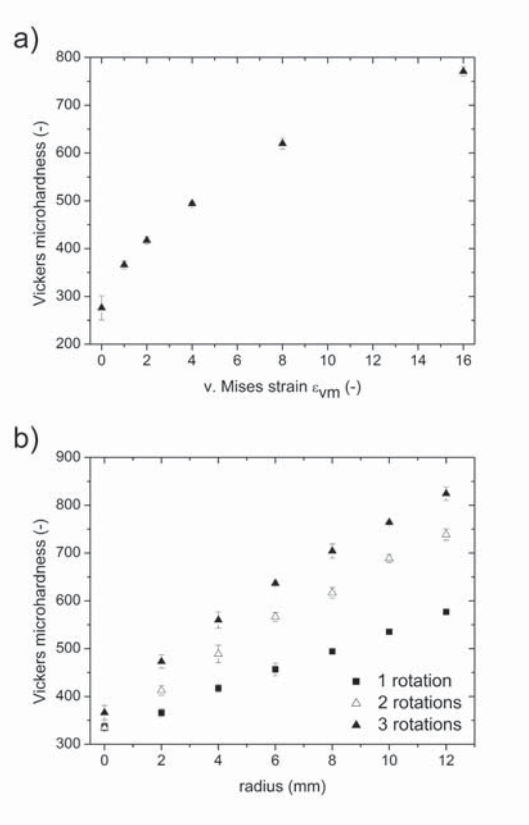

Figure D.4 Mechanical changes due to the shear deformation process. (a) Hardness as a function of applied strain. (b) Hardness along the radius for 1, 2 and 3 rotations of the HPT disc. The standard deviation as an error bar is only visible for deviations larger than the used symbols.

In Figure D.4b the hardness of the investigated material along the radius of the HPT disc is presented for various numbers of rotations. The hardness increases linearly with the radius and no saturation, as reported for pure metals [13, 14], takes place. The reason for the ongoing increase of the hardness is that in the investigated deformation range no saturation or steady state of the microstructure sets in. Due to this the fracture specimens extracted from the HPT discs will have a hardness gradient across the thickness with regard to orientation A and B and a hardness gradient along the crack propagation direction for orientation

C. However, since the deformation range investigated is very large in comparison with the strain or hardness gradient within a specimen, large differences in fracture toughness can be expected. In the following the specified degree of deformation of the specimens refers to the middle of each sample with reference to orientation A and B. Regarding orientation C the degree of deformation is constant along the crack front, but increasing along the crack extension direction. As one can see in Figure D.4b the hardness continues to increase from 10.5 mm, which corresponds to an equivalent strain of 16 after 3 rotations, to 12 mm. However the very edge of the sample could not be investigated with fracture toughness samples, because the specimens needed a minimum thickness of about 2 mm. Therefore the largest investigated strain with fracture toughness samples was about 17 regarding orientation A.

Changes in the fracture toughness

In Figure D.5 the fracture toughness as a function of pre-strain for the different specimen orientations is plotted.

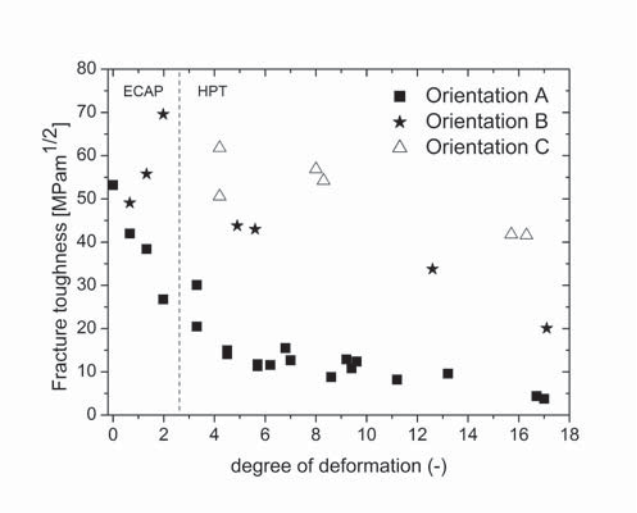

Figure D.5 Fracture toughness for different crack plane orientations as a function of deformation strain.

Additionally for the low strain regime (ϵ_{vM}=0-2.1) data points from reference [15] are incorporated. The data points were obtained with the same steel subjected to Equal Channel Angualar Pressing (ECAP) via Route A for 1, 2 and 3 passes, where one pass corresponds to an equivalent strain of 0.67. The ECAP Route A strain path is comparable to monotonic HPT. The specimens had the same crack plane orientation with respect to the material flow, however the denominations were reversed in reference [15]. Samples with orientation A show a strong decrease in toughness with respect to an initial toughness of the starting material of ∼53 MPa $m^{1/2}$ down to a value of about 4 MPa $m^{1/2}$ after equivalents strains of ∼17. The

largest decrease in the toughness is in the deformation range between 0 and 8, afterwards the fracture toughness decreases rather slowly with increasing strain.

In contrast to this, for orientation B a strong increase in toughness was reported for small strains [15]. For larger strains a decrease in the fracture toughness is again observed. However in this case the crack deflected about 90° with respect to the fatigue pre-crack. Therefore the values must be regarded as a lower bound for the real fracture toughness. Since the crack deflected for this crack plane orientation fewer experiments than for orientation A were performed.

Regarding orientation C, an average value of ∼56 MPa $m^{1/2}$ was determined for equivalent pre-deformation strains of 4. This value is only a lower bound for the real fracture toughness as the P_{max}/P_Q load-ratio during the test record was too large. This large ratio should also explain the large scatter in the two data points. With an increasing degree of pre-deformation the fracture toughness decreases again, however a fracture toughness of ∼42 MPa $m^{1/2}$ after ϵ_{vM}=16 was maintained. The fracture toughness in this orientation is approximately 10 times larger than that measured in orientation A for almost the same pre-deformation and hence hardness.

D.4 Discussion

D.4.1 Microstructure and hardness

The deformation behavior of fully pearlitic steels has been investigated by several groups. When compared to an older study related to HPT of the same pearlitic steel [16] the same deformation features were observed. For example, an alignment of the pearlitic colonies into the shear direction, a marked decrease in the lamellar spacing and a fragmentation of the lamellae at higher strains. The microstructural changes presented in Figure D.2a-d lead to the strong strain hardening. The hardening mechanisms acting in eutectoid steels have been extensively investigated in the past with eutectoid steels subjected to wire drawing [17, 18]. The strength is principally controlled by the interlamellar spacing, this restricts the dislocation glide length. Additionally, for large deformations, dispersion strengthening must also be taken into account when the lamellar structure becomes fragmented. Similar to previous studies on HPT of pearlitic steels, no dissolution of the carbides could be observed through SEM imaging [19–21]. This can be related to the fact that the maximum investigated strains were not large enough to induce a dissolution. The maximum nominal shear angle, γ, investigated in this study was about ∼28 (ϵ_{vM}∼16) while the largest nominal shear angle investigated in reference [19] was about 400. In this study, the HPT tools have anvils made from a high speed steel. The maximum strain hardening must be roughly limited by the strength of the anvil material. For that reason, more than three rotations of the pearlitic steel resulting in a hardness of the pearlitic steel comparable to the hardness of the anvils were not possible without plastic deformation or failure of the tool and thus no dissolution was observed.

D.4.2 Evolving anisotropy in the fracture toughness

Orientation A

In Figure D.5 the marked difference in the fracture behavior of the investigated steel regarding different testing directions was presented. This anisotropy and its evolution can be related to the fractographic features. In Figure D.6a the typical fracture surface of an undeformed pearlitic steel is shown. Typical for such a steel, pseudo-cleavage fracture is present, which can be explained by the shear-crack model proposed by Miller and Smith [22]. Since this fracture mechanism is strongly dependent on the local orientation of the pearlite colonies a tortuous crack evolves when a random orientation of the undeformed pearlite colonies is present in the undeformed state. With increasing pre-deformation in Figures D.2b-d a pronounced alignment of the pearlite colonies into the shear direction was found. This feature is reflected also on the fracture surface, see Figures D.6b-d. The fractographs show that the crack path becomes gradually less tortuous as the crack propagates along the aligned lamellar structure.

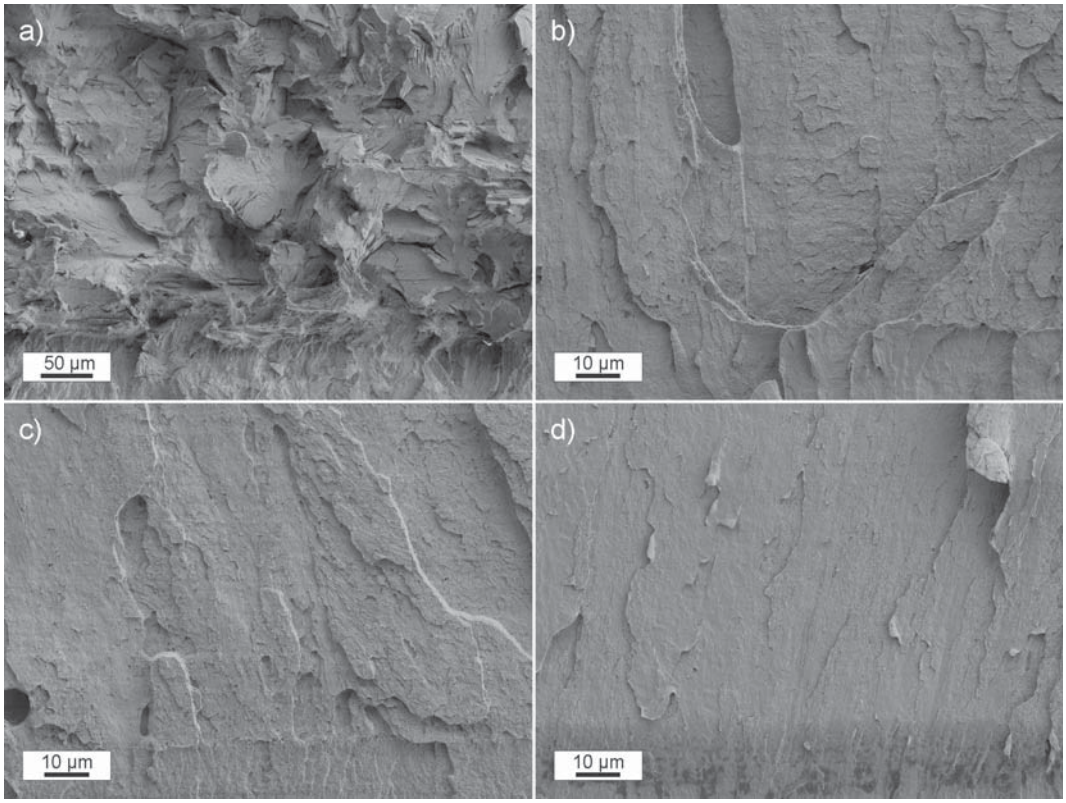

Figure D.6 Fractography of different strongly deformed specimens with orientation A. Undeformed specimen (a). Fracture surface corresponding to an equivalent strain ϵ_{vM} of ∼4 (b), (c) 8 (c) and 17 (d). Note the different magnification for (a) and (b-d). With increasing pre-deformation the crack path tortuosity decreases.

At lower strains, Figure D.6b, the crack intersects with less favorably aligned colonies and so a certain roughness is still present. At higher strains (Figure D.6d) almost all of the pearlite lamellae seem to be aligned and the crack surface becomes very smooth. Moreover, for low and intermediate strain levels (Figure D.6b and c) a stretched zone at the bottom of the fractographs is still noticeable whereas for the highest strained sample, Figure D.6d, the transition from the fatigue pre-crack to the overload fracture surface is not perceptible anymore, this also justifies the extremely low measured fracture toughness. Although the fracture behavior of classical pearlitic steels has been extensively discussed in the past, see e.g. [23, 24], the fracture process in the present strongly deformed state is possibly different and should be analyzed more in-depth.

To investigate the possible processes a series of fractographs of one of the highest strained specimens, $\epsilon_{\mathrm{vM}} \sim 17$, is presented. In Figure D.7a an overview fractograph is shown with details marked with squares. At low magnifications almost no evidence for a transition from a fatigue pre-crack to the overload fracture can be found. The fracture surface is fairly flat and only some steps and ledges can be found, which emerge during the fracture process whenever the crack-front is located locally on different heights.

At higher magnifications, the transition zone, Figure D.7b and c, becomes more explicit. In Figure D.7b and c in the lower part of the fractograph the fatigue fracture surface is recognizable, whereas in the upper part the overload fracture surface is demonstrated. The two micrographs represent the two different types of crack paths which can be found in the steel for high pre-deformations. In Figure D.7b the overload fracture is almost perfectly smooth and only very small steps are present for this crack propagation direction. This type of crack path can be associated with the aligned lamellar microstructure shown in Figure D.3a. The second more tortuous crack path is demonstrated in Figure D.7c. Besides very smooth areas where the crack propagates along the lamellar structure, the crack also intersects with a more or less rough area. In this case, it can be assumed that the crack propagates locally in a region where the lamellar structure is already fragmented into smaller pieces due to the shear deformation process. Microstructural examples of such fragmented structures were shown in the micrographs in Figure D.2d in a SEM-image and in Figure D.3b with a TEM image. However, since only a partial carbide fragmentation was found through microstructural investigations, the crack seems to run predominantly along the interfaces as illustrated in Figure D.7b.

In Figure D.7d the aforementioned steps are demonstrated at higher magnification. On the left side of the fractograph it can be seen that the heights of some ledges are in the range of some nanometers. Simultaneously, the lamella spacing for this material state is in the range of only 10 nanometers. Therefore it can be assumed that an individual step represents a layer of iron and the cementite phase. The crack propagates through the layers and delaminates at the iron-cementite interface. On the right side of the fractograph a much larger step is visible. These steps consist of many iron-cementite layers, as also can be seen from the fractograph in Figure D.7a at low magnifications.

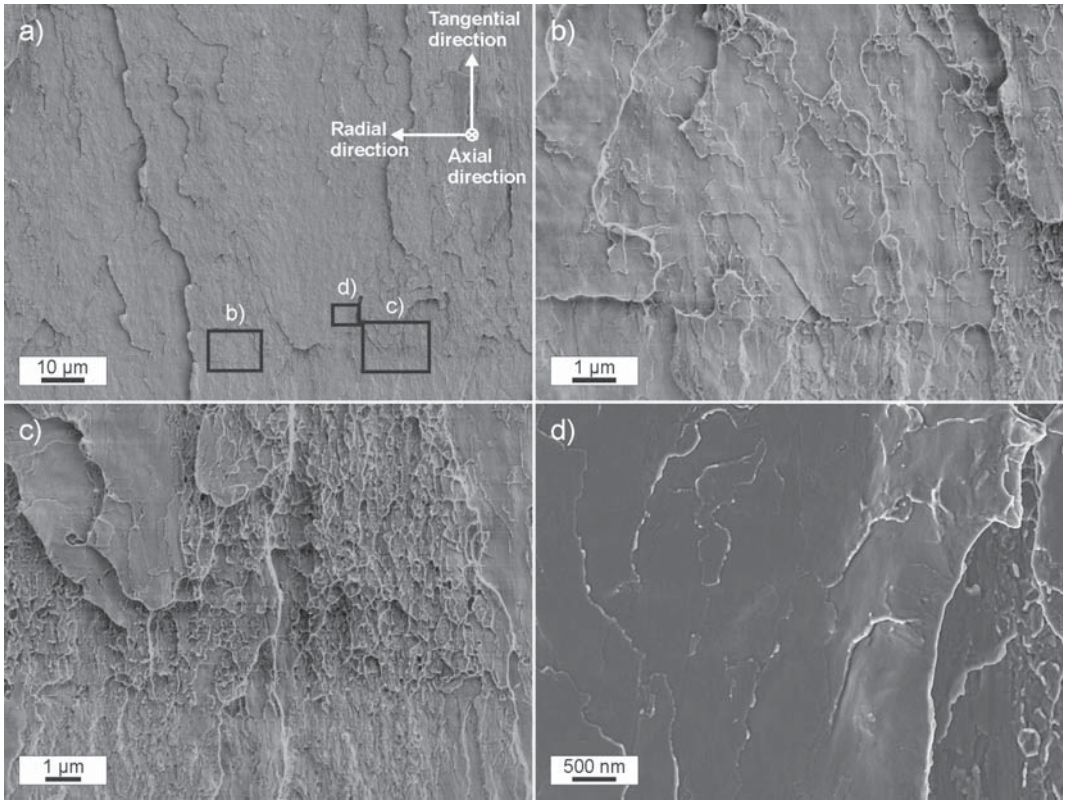

Figure D.7 Detailed fractographs presenting fracture features in the strongest deformed state with orientation A. (a) Overview with further details displayed in (b-d). (b) Smooth transition from the fatigue pre-crack to the overload fracture surface. (c) Rough transition from the fatigue pre-crack to the overload fracture surface. (d) Detailed view showing steps on the same size scale as the lamella spacing.

The very low fracture toughness in these most heavily deformed samples is determined by the energy to cleave the iron-cementite interface, another contribution is the bending and fracturing of the few ledges and the fracture energy of the somewhat more ductile regions. This interface cleavage dominated fracture process seems to lead to a fracture toughness only about 3-4 times larger than the Griffith toughness, $K_{Griffith}=(2\gamma_0 E)^{1/2}$, of iron, where γ_0 is the surface energy and E the Young's modulus.

Orientation B

For small strains, regarding SPD deformation, a large increase in fracture toughness was found for cracks along orientation B. At larger strains the fracture toughness begins to decrease. The micostructural reason for the increase in toughness for small strains can be seen in the evolving aligned pearlitic structure. For orientation B the aligned micostructure is perpendicular to the fatigue pre-crack. The essential tough-

ening mechanism is due to crack branching of the crack in front of the lamellae. For larger strains, the microstructural anisotropy promotes a high fracture resistance for global Mode I propagation and simultaneously for orientation A the fracture toughness becomes strongly deteriorated. For that reason the crack propagates almost perpendicular to the desired crack propagation direction. Although the fracture toughness decreases for stronger pre-deformations again, a larger fracture toughness as for orientation A can be found. This is because a short kinked pre-crack has a lower local Mode I driving force [25] in comparison with the straight crack path. This leads to the toughness improvement even for the deflected crack. For that reason a still remarkable fracture toughness of $\sim$20 MPa $m^{1/2}$ was determined for the strongest deformed specimen with orientation B. However these values are only a lower bound to the real Mode I fracture toughness, since for a real Mode I propagation the measured crack resistance would be even higher. On account of the crack deflection into the direction of lower fracture toughness, so to say into orientation A, the fracture surfaces show more or less the same features and therefore are not discussed again.

Orientation C

Generally, the fracture toughness of a material varies inversely with the yield strength or hardness of a metal or alloy. This is not the case when we consider orientation C. The strong improvement in the fracture toughness for orientation C can be attributed to the microstructural anisotropy caused by the HPT straining process. In Figure D.8a-c overview fractographs for specimens of orientation C with different amounts of pre-deformation are presented.

In Figure D.8a two delaminations dividing the crack front are visible. Such delaminations and the general positive effect on the fracture toughness are known in literature [26, 27]. Due to the stress relaxation in the thickness direction of the specimen, which is parallel to the horizontal direction of all fractographs, the stress triaxiality at the crack front is reduced. This stress component can also be called the through-thickness stress. This leads in turn to a reduction in the maximum tensile stresses and allows a further deformation prior to final fracture by pore formation and coalescence and shearing of the thin ligaments, as shown later in this section. Through this a higher fracture toughness can be achieved. With increasing strain, Figure D.8b and c, the number of delaminations increases and in Figure D.8c an almost uniform delamination spacing is established. On account of the increase in the number of delaminations the rise in the hardness with increasing strain is partly compensated and still a fracture toughness of about 42 MPa $m^{1/2}$ could be measured after equivalent strains $\epsilon_{vM}\sim$16. This is extraordinary for a material with a yield stress in excess of 3000 MPa, as can be inferred from the hardness values. The increase in the number of delaminations is partly a consequence of the enhanced microstructural alignment with increasing strain as previously explained. But another essential aspect controlling the delamination spacing is the distribution of the through thickness stress component. Next to a delamination the through-thickness

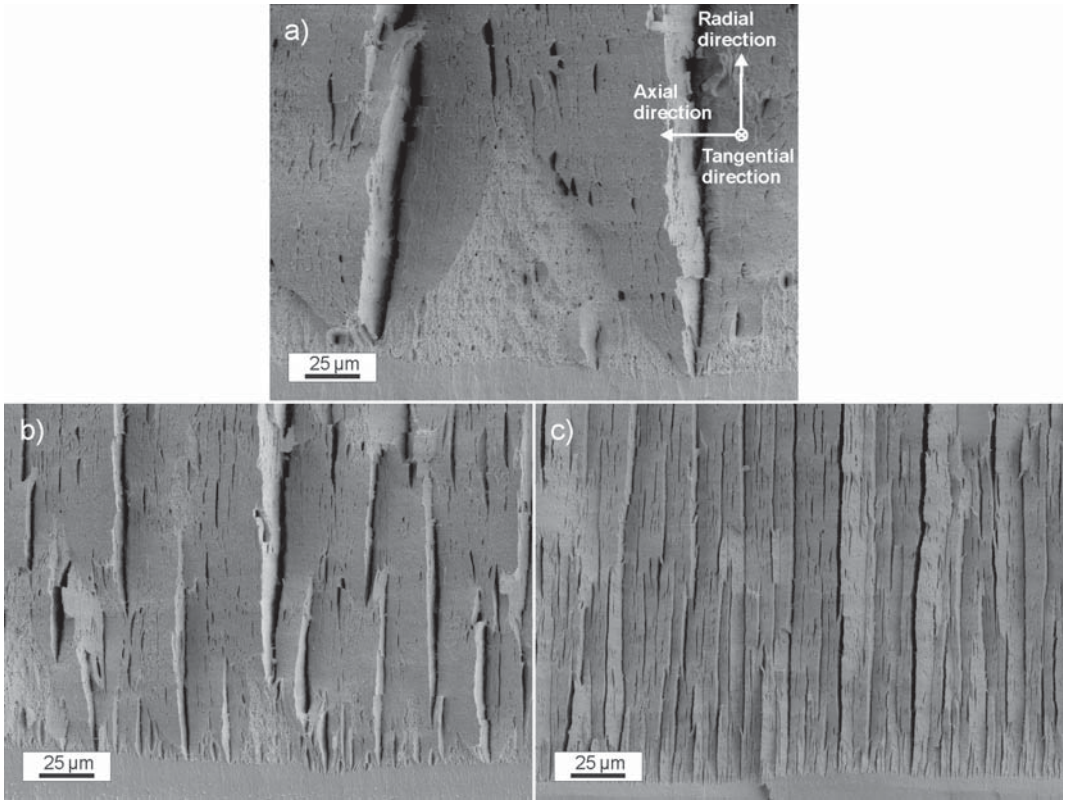

Figure D.8 Overview fractographs of specimens with orientation C with equivalent strains ϵ_{vM} of 4 (a), 8 (b) and 16 (c). With increasing pre-deformation the number of delaminations increases

stress component must be zero due to the free internal surface. However, this stress component can recover along the thickness. So not very far from the first delamination the stress level for the formation of the next delamination is reached and another delamination is found. For this stress value also a fracture toughness value can also be ascribed in the presence of existing flaws. In this case orientation A is the essential crack system since the delaminations and specimens with orientation A have the same crack opening direction. In both cases it is the axial direction, which can be further seen in a comparison of the coordinate systems in Figure D.7a and Figure D.8a. As shown before, the fracture toughness for orientation A deteriorates with increasing strain. Therefore the distance between the delaminations decreases since the critical stress or toughness level for cracking is reached at smaller distances along the thickness with increasing pre-strain of the sample.

In Figure D.9a again an overview fractograph of a specimen with an equivalent strain $\epsilon_{vM}\sim 8$ is presented, two details are shown in Figure D.9b and c. In Figure D.9b the inside of a material delamination is shown. Again a very fine step structure can be found. A closer look also shows that these structures correspond to the other side of the material delamination. This means that locally almost ideal brittle fracture

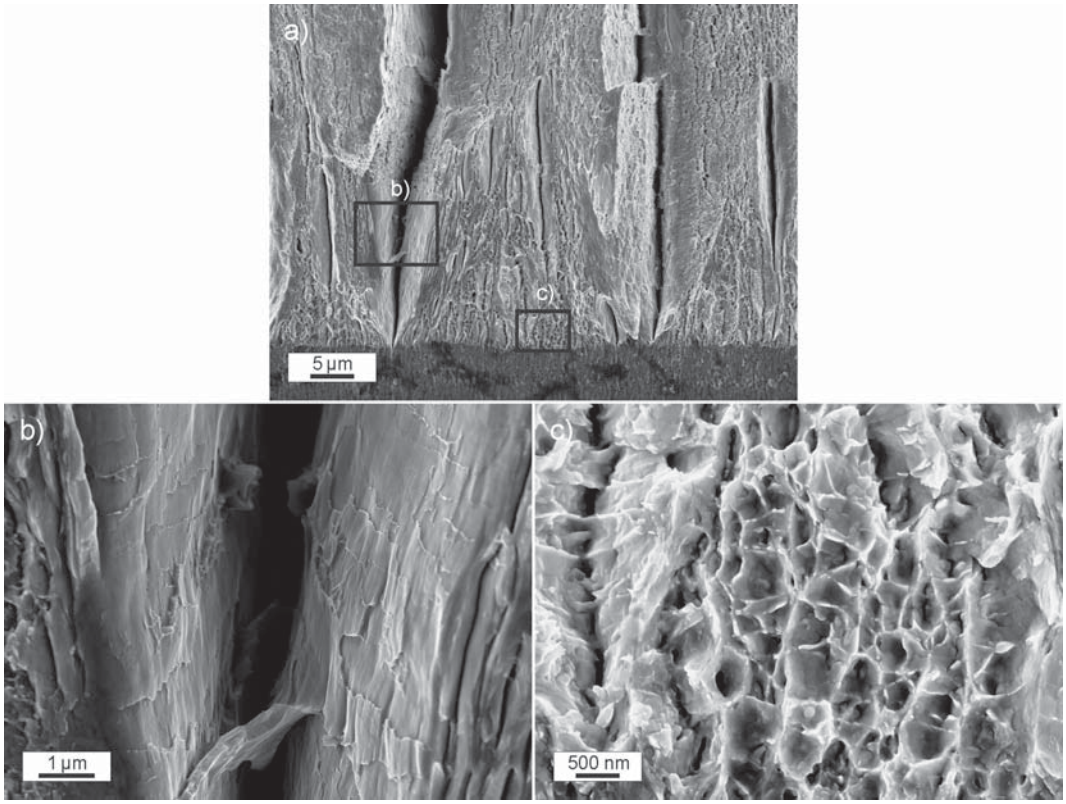

Figure D.9 Detailed fractographs presenting the fracture process in a shear deformed pearlitic steel with orientation C, shown with a specimen after an equivalent strain ϵ_{vM}= 8. (a) Overview with further details displayed in (b) and (c). (b) Delamination originating from fracture between iron-cementite interfaces. (c) Submicrocrystalline dimple structure situated between material delaminations.

occurs. These steps were already mentioned in Figure D.7d for orientation A and can be also found for this orientation. For both orientations the delamination at the iron-cementite interface is the essential fracture mechanism determining the fracture toughness of the material state. Additionally, the formation of the delaminations allows for the formation of a submicron dimple structure (Figure D.9c). The reason for this structure is that the occurrence of delaminations changes the stress state locally, which seems to allow the formation of voids instead of brittle fracture as for orientation A. To summarize, while fracture at the iron-cementite interface leads to a strong deterioration in the fracture toughness for orientation A, it is quite a beneficial effect for orientation C.

D.5 Summary and conclusions

In the framework of this study the fracture toughness of a fully pearlitic rail steel with respect to three different crack plane orientations and as a function of pre-strain in the range of ϵ_{vM}=0-17 has been investigated. The results clearly show that there is a strong effect of the crack plane orientation on the observed fracture toughness and on the acting fracture process. With increasing pre-strain the fracture toughness is strongly deteriorated for orientation A, while remains fairly acceptable for the other directions even when the hardness increases for all of the different testing orientations in the same manner.

Bibliography to paper D

[1] M.A. Meyers, A. Mishra and D.J. Benson: Prog. Mater. Sci., 2006, vol. 51, pp. 427-556.

[2] R. Z. Valiev, R.K. Islamgaliev and I.V. Alexandrov: Prog. Mater. Sci., 2000, vol. 45, pp. 103-189.

[3] R.Z. Valiev and T.G. Langdon: Prog. Mater. Sci., 2006, vol. 51, pp. 881-981.

[4] A.P. Zhilyaev and T.G. Langdon: Prog. Mater. Sci., 2008, vol. 53, pp. 893-979.

[5] A. Ramesh, S.N. Melkote, L.F. Allard, L. Riester and T.R. Watkins: Mater. Sci. Eng., 2005, vol.390A, pp. 88-97.

[6] K. Hono, M. Ohnuma, M. Murayama, S. Nishida, A. Yoshie and T. Takahashi: Scripta Mater., 2001, vol.44, pp. 977-983.

[7] W. Lojkowski, M. Djahanbakhsh, G. Brkle, S. Gierlotka, W. Zielinski and H.-J. Fecht: Mater. Sci. Eng., 2001, vol.303A, pp. 197-208.

[8] R. I. Carroll and J.H. Beynon: Wear, 2007, vol.262, pp. 1253-1266.

[9] D.F. Cannon and H. Pradier: Wear, 1996, vol.191, pp. 1-13.

[10] J.W. Ringsberg, M. Loo-Morrey, B.L. Josefson, A. Kapoor and J.H. Beynon: Inter. J. Fat., 2000, vol.22, pp. 205-215.

[11] M. Takikawa and Y. Iriya: Wear, 2008, vol.265, pp. 1300-308.

[12] P. Clayton and X. Su: Wear, 1996, vol.200, pp. 63-73.

[13] A. Vorhauer and R. Pippan: Scripta Mater., 2004, vol.51, pp. 921-925.

[14] C. Xu, A.P. Zhilyaev, Z. Horita and T.G. Langdon: Mater. Sci. Forum, 2008, vols.584-586, pp. 3-8.

[15] F. Wetscher, R. Stock and R. Pippan: Mater. Sci. Eng., 2007, vols.445-446A, pp. 237-243.

[16] F. Wetscher, A. Vorhauer, R. Stock and R. Pippan: Mater. Sci. Eng., 2004, vols.387-389A, pp. 809-816.

[17] J.D. Emburry and R.M. Fisher: Acta Met., 1966, vol.14, pp. 147-159.

[18] G. Langford: Metall. Trans. A, 1977, vol.8, pp. 861-875.

[19] Y. Ivanisenko, W. Lojkowski, R.Z. Valiev and H.-J. Fecht: Acta Mater., 2003, vol.51, pp. 5555-570.

[20] B.B. Straumal, A.A. Mazilkin, S.G. Protasova, S.V. Dobatkin, A.O. Rodin, B. Baretzky, D. Goll and G. Schtz: Mater. Sci. Eng., 2009, vol.503A, pp. 185-189.

[21] X. Sauvage, Y. Ivanisenko: J. Mater. Sci., 2007, vol.42, pp. 1615-1621.

[22] L.E. Miller and G.C. Smith: J.I.S.I., 1970, vol.208, pp. 998-1005.

[23] J.J. Lewandowski and A.W. Thompson: Metall. Trans. A, 1986, vol.17, pp. 1769-1786.

[24] D.J. Alexander and I.M. Bernstein: Metall. Trans. A, 1989, vol.20, pp. 2321-2335.

[25] R. Pippan: Eng. Frac. Mech., 1993, vol.44, pp. 821-829.

[26] R.W. Hertzberg: Deformation And Fracture Mechanics Of Engineering Materials, 4th ed., John Wiley & Sons Inc., New York, 1996, pp. 409-418.

[27] W. Guo, H. Dong, M. Lu, X. Zhao: Int. J. Press. Vessels Pip., 2002, vol.79, pp. 403-412.

E

The ductile to brittle transition of ultrafine-grained Armco iron: an experimental study

A. Hohenwarter[a,b], **C. Kammerhofer**[a,b] **and R. Pippan**[a,b]

[a]Erich Schmid Institute of Materials Science, Austrian Academy of Sciences, A-8700 Leoben, Austria
[b]CD-Laboratory for Local Analysis of Deformation and Fracture, A-8700 Leoben, Austria

Abstract

Fracture toughness measurements on bcc iron (Armco-iron) subjected to severe plastic deformation (SPD) were performed. Through high pressure torsion an ultrafine grain structure was obtained and with subsequent heat treatments the grain size was varied between 300 nm and 5 μm. The combination of SPD and individual heat treatments allows for a systematic study of the ductile to brittle transition (DBT) in the fracture behavior as a function of grain size. Additionally, the influence of different crack plane orientations was taken into account. The results show that the DBT moves for smaller grain sizes ($\leq$1 μm) to higher transition temperatures. Furthermore, large differences in the absolute toughness values for a given temperature for the different crack plane orientations and grain sizes were determined. The findings can be related to a change in the crack path from transcrystalline fracture for grain sizes larger than 1 μm to intercrystalline-dominated fracture for grain sizes smaller than 1 μm.

E.1 Introduction

Fatal disasters such as the Titanic's sinking or the Liberty ship incidents during World War II are nowadays known to have their physical origin in the ductile to brittle transition (DBT) of bcc-metals and the associated cleavage fracture in the low temperature regime. The micro-mechanisms of cleavage fracture and the connected transition in the fracture behavior from brittle to ductile fracture with increasing temperature have extensively been studied and different models have been proposed for the conditions under which cleavage fracture occurs, see, e.g. [1–3]. Contemporaneously in the last century various severe plastic deformation (SPD) techniques have been developed, which enable to production of ultrafine-grained (UFG) and nanocrystalline (NC) metals by imposing very large strains on coarse-grained starting materials. Due to the strong grain-refinement these materials posses mostly enhanced mechanical and physical properties compared to their coarse-grained counterparts [4–6].

The aforementioned ductile to brittle transition (DBT) of the fracture behavior and especially its transition temperature, primarily important in bcc metals with few exceptions, often plays an important role for a safe implementation of materials as can be seen from the examples mentioned earlier. For that reason such studies also have to be performed with UFG and NC metals in case they were considered for structural applications in future. Additionally, SPD in combination with subsequent heat-treatments allows the unique possibility to perform basic studies of the DBT-temperature (DBTT) by varying the grain size and thus the yield stress in a wide range and down to grain sizes, which have not been accessible with classical deformation techniques such as rolling and subsequent annealing up to now. In contrast to other techniques such as electrochemical deposition, the purity of the material is here solely given by the starting material and no remaining porosity, as to be considered for powder consolidation, has to be taken into account to be major factors influencing the fracture test results.

Within this paper a detailed study into the DBT depending on the grain size ranging from a few hundred nanometers up to classical grain sizes in the micrometer range will be presented. Additionally, the influence of the crack plane orientation on the fracture behavior was accounted for and discussed.

E.2 Experimental

The composition of ARMCO-iron used in this study is 0.009 wt% C, 0.060 wt% Mn, 0.009 wt% P, 0.007 wt% S and the balance Fe. The HPT discs had a diameter of 30 mm and a thickness of 9 mm and were annealed at 800 °C for one hour prior to HPT deformation. The discs were subjected to ten revolutions at room temperature at a nominal pressure of 2.8 GPa. Afterwards, Compact-tension (CT) specimens were extracted from the HPT disc with two different crack plane orientations. In Figure E.1 the HPT sample, the extracted specimens and the coordinate system used are

displayed with the radial, tangential and axial directions indicated. The difference between the tangential and the radial direction should be noted. RD is the direction heading into the center of the disc, whereas the tangential direction describes the tangential to the circumference of the disc at a particular radius. The specimens' orientation was named after the expected crack propagation direction according to the coordinate system (Figure E.1) resulting in a tangential and a radial specimen orientation.

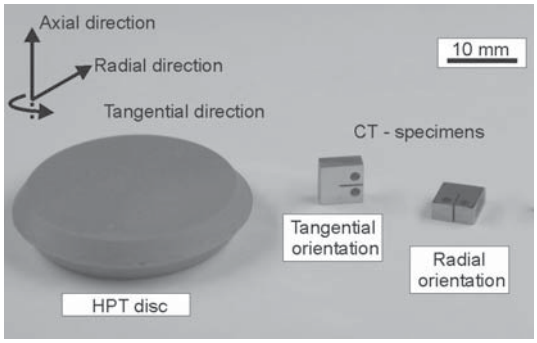

Figure E.1 Photograph presenting the fracture specimens with their different crack orientations machined from the HPT disc.

The geometry of the specimens as well as the calculation of the fracture toughness was based on the recommendations of the ASTM standard E-399. The specimens had a width, W, of 5.2 mm, an initial crack length, a, of ∼2.6 mm and a thickness, B, of ∼2.6 mm. The fatigue pre-crack was introduced under cyclic compression loading [7]. Along with the SPD-microstructure, different nominal grain sizes, such as 300 nm, 1 and 5 μm were investigated. The grain sizes were adjusted with individual heat-treatments. The heat-treatment conditions for the individual grain sizes and the resulting hardness values can be found in Table E.1. All specimens were taken from an area in the former HPT disc, where a saturation in grain-refinement has taken place and therefore a homogeneous hardness along the radius was achieved as shown in [8] with hardness measurements after comparable deformation conditions. The fracture toughness tests were performed on a testing machine from Zwick (Zwick 1382) at a cross-head speed of 400 μm/min. In order to adjust the individual temperatures the specimens were either tested in liquid nitrogen or for the interval between -196 °C and room-temperature in a cooling chamber and for higher temperatures in a heating chamber. The microstructure and the fracture surfaces were characterized with a Zeiss 1525 scanning electron microscope (SEM). Microhardness measurements were performed with a Vickers indenter and a load of 200 gf and 5 indents were averaged.

Table E.1 Summary of the heat-treatment conditions

Microstructure	Heat-treatment conditions	Hardness HV 0.2
SPD	-	423±2
300 nm	350 °C for 1 hour	328 ±3
1 μm	450 °C for 2 hours	212 ±4
5 μm	650 °C for 1 hour	117 ±4

E.3 Results

E.3.1 Microstructure

In Figure E.2 a series of SEM-images of the investigated microstructures, looking into the radial direction (RD), are presented, see also coordinate system in Figure E.2a, which is the same for all micrographs. In Figure E.2a the ultrafine-grained structure in the steady state of deformation is shown. In this context, the term steady state is used to describe the fact that a further increase in strain would not lead to an additional refinement of the microstructure, as shown for instance in [9, 10]. Typical for the radial observation direction an elongated grain structure can be observed. Additionally, a certain inclination of the structural elements with respect to the shear deformation direction, which is parallel to the long margins of Figure E.2a is present, which is simultaneously the tangential direction (TD). These microstructural findings are similar to other reports dealing with ultrafine-grained metals investigated in the same direction [11]. In Figure E.2b-d the heat-treated microstructures are shown with different nominal grain sizes of 300 nm (Figure E.2b), 1 μm (Figure E.2c) and 5 μm (Figure E.2d). As usual, the heat-treatments, which caused recrystallization, lead to an increase in grain size and thus a decrease in hardness, see Table E.1. However, as the micrographs show, also the aspect-ratio of the grain structure is changed. It seems that the elongated SPD microstructure changes to a more equiaxed structure for the 300 nm and larger grain sizes.

E.3.2 Fracture toughness results

General remark

In Figure E.3 and Figure E.4 a summary of all fracture tests for the tangential orientation as well as for the radial orientation is presented. Each data point corresponds to a single measurement. Small arrows next to data points are set to indicate that these specimens fractured in a ductile manner and did not meet small scale yielding conditions. For that reason, e.g. specimens with a mean grain size of 5 μm, see Figure E.3, show after an increase in the fracture toughness from -196°C to -100°C, an apparent drop in the fracture toughness at room temperature. In such a case the yield strength is already too small with respect to the restricted specimen dimensions so that small scale yielding conditions do not prevail anymore. These data points must be regarded as a lower bound for the real fracture toughness. In

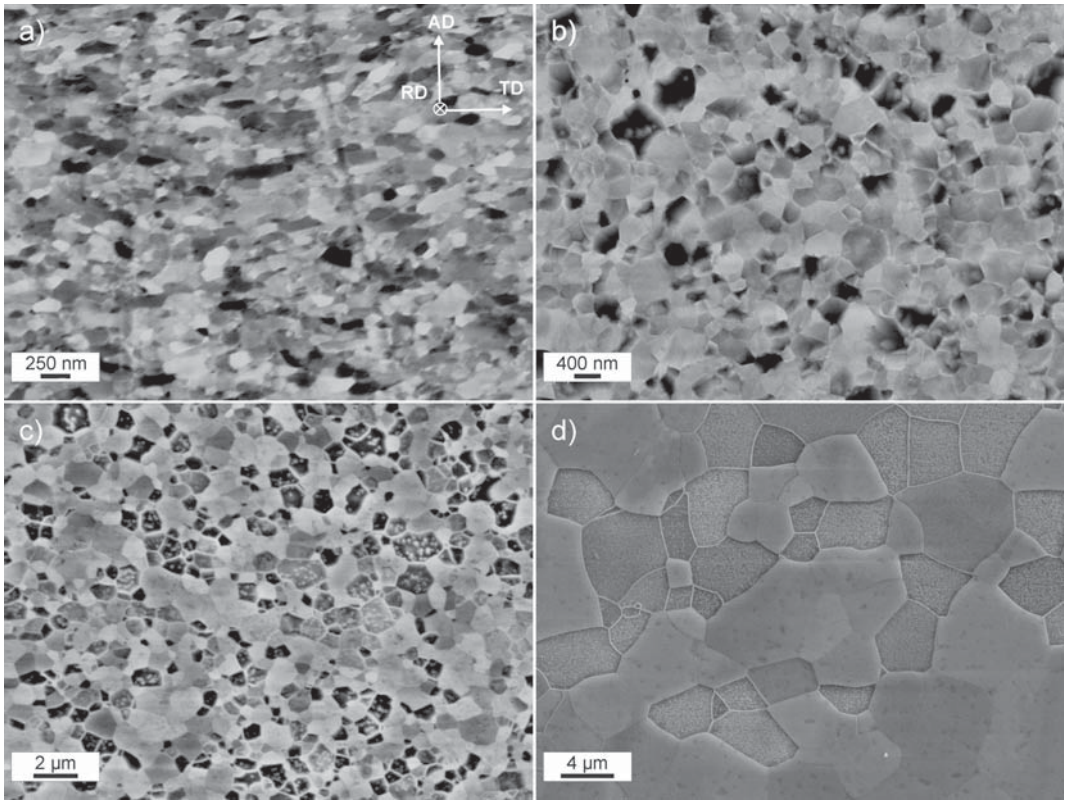

Figure E.2 Typical micrographs of the investigated microstructures looking into the radial direction of the HPT disc. (a) SPD microstructure showing an elongated microstructure aligned into the shear direction. Heat-treated microstructures with nominal grain-sizes of (b) 300 nm, (c) 1 μm and (d) 5 μm with an equiaxed grain structure.

reality, an increase of the fracture toughness compared to valid data points at lower testing temperatures is to be assumed. In such a case no further measurements were performed at higher temperatures. The scatter of the data points with regard to the possible inaccuracy of the measurement of the geometrical parameters of the specimens and the force was evaluated to be smaller than 1 MPa $m^{1/2}$ through uncertainty analyses.

Tangential orientation

As Figure E.3 shows, the SPD-microstructure has the lowest fracture toughness values along the entire temperature interval and of all studied microstructures. The fracture toughness is continuously increasing in the investigated temperature range from 5.5 MPa $m^{1/2}$ at -196 °C to 48.2 MPa $m^{1/2}$ at 200 °C. Regarding the 300 nm specimens in the lower temperature range (-196 °C to -70 °C) the toughness values are comparable to those of the SPD specimens. However, at ambient temperatures already a large difference compared to the SPD state was determined with an esti-

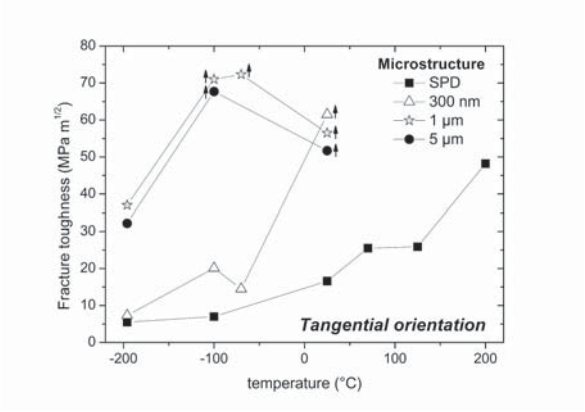

Figure E.3 Summary of the fracture toughness measurements for the tangential orientation. Arrows next to data points imply that the values must be regarded as lower bound values for the real fracture toughness.

mated value of 61.5 MPa $m^{1/2}$. As explained, the arrow indicates that the value is just a lower estimate of the real fracture toughness. For grain sizes of 1 μm and 5 μm at -196 °C a value approximately 4 times larger as for the submicrocrystalline states was measured, 37 MPa $m^{1/2}$ and 32.2 MPa $m^{1/2}$, respectively. For both material states the measurements become invalid at -100 °C. This indicates that the real fracture toughness is even higher and leads to the conclusion that the DBTT is lower for the submicrocrystalline material states, SPD microstructure and 300 nm grain size.

Radial orientation

Specimens with radial specimen orientation show a different picture in Figure E.4.

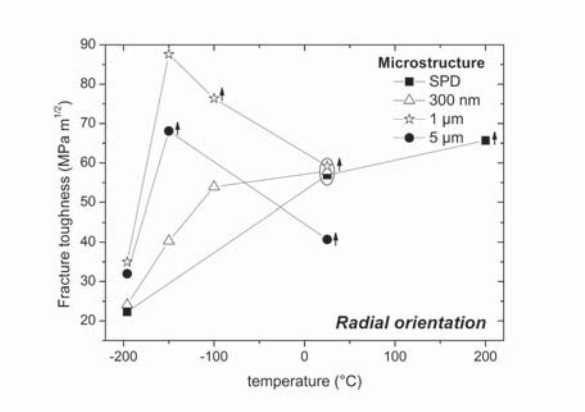

Figure E.4 Summary of the fracture toughness measurements for the radial specimen orientation. Arrows next to data points imply that the values must be regarded as lower bound values for the real fracture toughness.

The SPD and the 300 nm specimens have almost the same fracture toughness values at -196 °C and room temperature. However, at -196 °C the values are approximately 4 times larger than in the tangential specimen orientation. In contrast to this, the microcrystalline specimens have again a higher fracture toughness at -196 °C than the submicrocrystalline ones, but are comparable to the measurements of the tangential specimen orientation of the same grain size. At higher testing temperatures the values for the fracture toughness values again increase tremendously. Since the measurements become invalid before room temperature is reached it can be concluded that the DBTT is again lower for the microcrystalline states compared to the submicrocrystalline samples.

E.4 Discussion

E.4.1 Dependency of the DBTT on grain size

One of the major results of this experimental study is that the DBTT moves for the smaller grain sizes to higher temperatures, which is at first in contrast to other studies dealing with this topic see for instance [12, 13]. In the following section fractographs will be presented, which are helpful for the discussion of this point.

Fractography of the tangential orientation

In Figure E.5a-c the typical fracture surfaces of Fe-SPD tested at -196 °C (a) , 70 °C (b) and 200 °C (c) are presented. Also displayed is the used coordinate system, showing that in these specimens the crack propagation direction is in the tangential direction (TD) and the fracture surface is oriented looking into the axial direction (AD). At -196 °C a granular structure on the fracture surface is visible. Intercrystalline grain boundary fracture occurs, which leads to the rather low measured fracture toughness of about 5.5 MPa $m^{1/2}$ at cryogenic temperatures. The same fracture type was also found at room temperature and discussed in [14] more in detail. With increasing temperature grain boundary fracture still occurs, however also more plastification in the shape of steps and ledges, see Figure E.5b, which causes an increase in the fracture toughness, can also be found. Finally, at a testing temperature of 200 °C dimple fracture can be found, Figure E.5c. In Figure E.5c (inset picture) one of the dimples is magnified. Here it can be recognized that the dimple wall surrounds a cluster of grains, which form the nucleation point for void formation and growth.

In general, it could be assumed that the DBTT decreases with the grain size. This follows directly from the well known Yoffee-diagram. For a given grain size the effective yield stress, σ_y , for the onset of plastic deformation at the crack tip is compared with the brittle fracture stress, σ_b [15]. In this rather simple model, the fracture type depends on the stress level which is reached first behind the crack tip, either the effective yield stress, promoting ductile fracture, or the brittle fracture stress leading to brittle fracture. Whereas σ_y decreases strongly with increasing

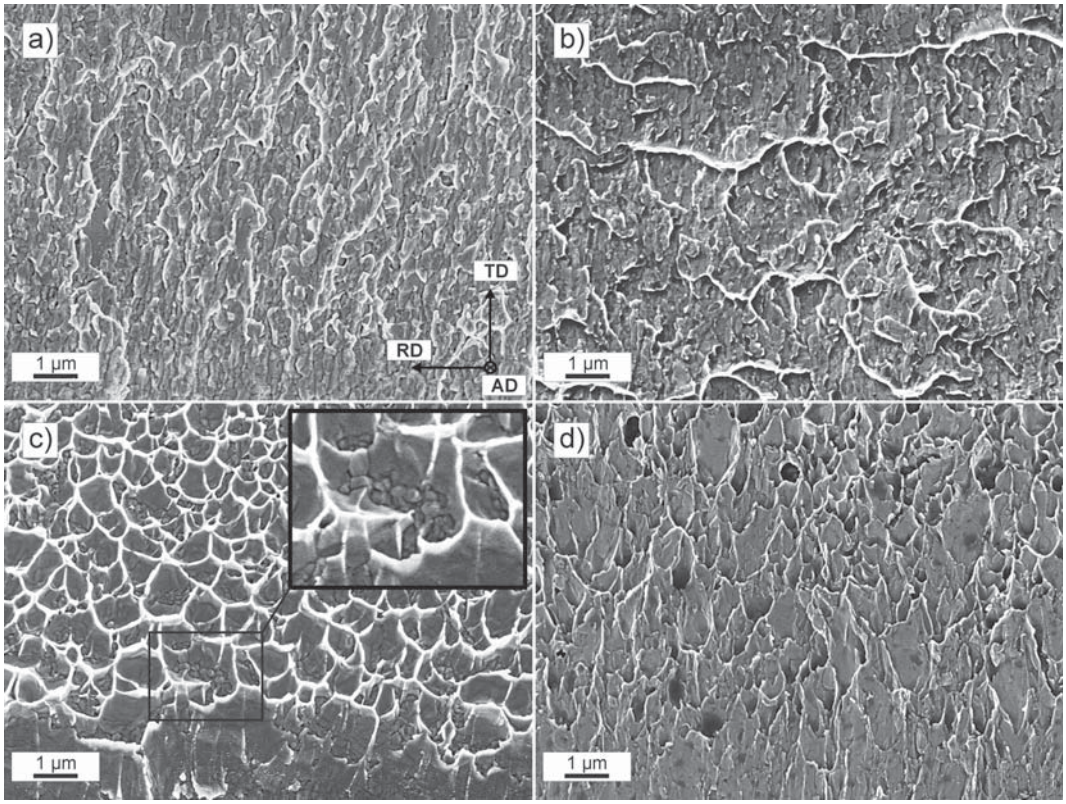

Figure E.5 Representative fractographs demonstrating important features of the different fracture types found in submicrocrystalline specimens with tangential specimen orientation. SPD specimens tested at (a) -196 °C revealing intercrystalline fracture. (b) SPD specimen tested at 70 °C showing evidences of increased plasticity. (c) SPD specimen tested at 200 °C with dimple fracture and (d) a specimen with a nominal grain size of 300 nm already exhibiting dimple fracture at room temperature.

temperature, σ_b is fairly independent on the temperature, but increases with decreasing grain size. This is due to the fact that a smaller grained microstructure provides a higher density of grain boundaries to stop or even blunt a crack. To conclude, one method to decrease the DBTT is to increase σ_b by decreasing the grain size. These considerations are based on the occurrence of a transcrystalline crack path, where the crack runs on low indicated crystallographic planes. However, in this study intergranular fracture occurred and therefore it seems that the model mentioned before cannot apply. The intergranular fracture type is often associated with a certain type of grain boundary embrittlement, where sulphur and phosphor are well known examples in connection with steels leading to a pronounced grain boundary embrittlement. In this study an iron with a rather high purity was chosen, see the experimental section, and the heat-treated microstructures show a different behavior. These factors weaken the impurity argument, as follows.

Regarding the 300 nm samples of the same specimen orientation, it was found that the fracture toughness values are comparable to the SPD values for measurements below room temperature. Also in this temperature regime intercrystalline fracture occurred as shown in Figure E.5a for the SPD specimen. However, at room temperature a large difference in the fracture toughness was found. This is also reflected on the fracture surface by dimple formation, see Figure E.5d. These dimples are elongated since they are part of the stretched zone. After this stretched zone intergranular fracture sets in again (not shown here). The stretched zone could be formed due to a larger deformation capacity of the 300 nm state compared to the SPD state.

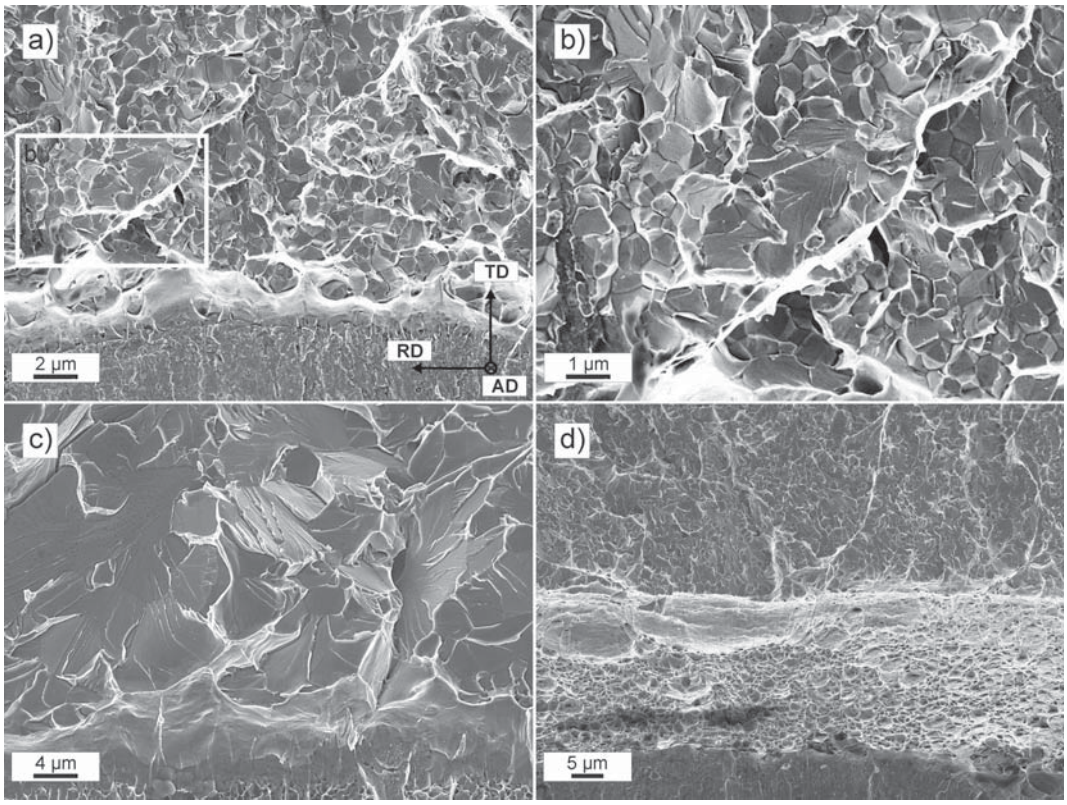

Figure E.6 Fractographs presenting fracture surfaces of specimens with microcrystalline grain size with tangential orientation. (a) Specimen with 1 μm nominal grain size tested at -196 °C. (b) Detail of (a) revealing intercrystalline fracture and also areas of transcrystalline fracture. (c) Specimen with 5 μm nominal grain size tested at -196 °C showing fully transcrystalline fracture. (d) Specimen with 1 μm grain size tested at -100 °C with ductile dimple fracture followed by brittle intercrystalline fracture.

Specimens with 1 μm grain size having the same specimen orientation, Figure E.6a, show at cryogenic temperature after strong crack blunting, a mixture of intercrystalline and transcrystalline fractured grains. In a more detailed view in Figure E.6b it can be seen that transcrystalline fracture occurs in the larger grains, where a

typical feature of transcrystalline fracture, river patterns, can be found. Specimens with 5 μm grain size also exhibit first a stretched zone before exclusively transcrystalline fracture sets in, Figure E.6c. At a higher testing temperature, for example a specimen with 1 μm grain size tested at -100 °C in Figure E.6d, ductile fracture occurs before in the upper part of the image again intercrystalline fracture can be found. Despite this the fracture toughness determined by means of linear elastic fracture mechanics (LEFM) strongly increases and becomes invalid. Although the fracture type is different for the 1 and 5 μm specimens, the fracture toughness values at -196 °C are more or less the same. Surprisingly, the microcrystalline specimens (1 and 5 μm grain size) show both a crack blunting behavior before cleavage fracture sets in.

The occurrence of classical ductile fracture for grain sizes starting from 1 μm below room temperature and the large ductile stretched zone of the 300 nm specimen at room temperature gives the hint that intercrystalline fracture of the SPD structure is not due to an impurity embrittlement. When we assume that remaining impurities are dragged along the grain boundaries during the heat-treatments, which is classically the case, the amount of impurities should increase with increasing grain size as the fraction of grain boundaries decreases. Therefore these microstructures (larger than SPD) are more prone to fail through grain boundary embrittlement at -196 °C. On the contrary even a blunting for the 1 and 5 μm specimens was found. Additionally, at room temperature the microcrystalline specimens showed full ductile fracture and even the 300 nm specimen showed dimple fracture at least within a large stretched zone before brittle fracture set in. In contrast to this the SPD state showed brittle behavior at room temperature. To conclude, the intercrystalline crack path seems to be an intrinsic property of ultrafine grained Armco-iron that is not caused by impurities, but eventually leads to the lower DBTT for submicrocrystalline iron.

The reason for this property is not yet clear, however, simulations on nanocrystalline iron [16] indicate that under certain conditions an intercrystalline crack path in nanocrystalline iron could be observed by the formation of voids in front of the crack tip, which coalesce with the crack tip along the grain boundary. Also the strong alignment and their aspect ratio could be contributing to the observed crack path and the associated low fracture toughness. In reference [14] a method to increase the fracture toughness was discussed where after deformation via HPT the deformation path is changed and as a result a mixture of elongated and equiaxed grains was obtained. This microstructure showed still intercrystalline fracture, however a larger fracture toughness due to a stronger blunting of the crack tip. To conclude, the small grain size with the connected high hardness, the aspect ratio of the grains and the alignment of them seem to be factors contributing to the occurrence of the intercrystalline crack path.

E.4.2 The influence of the crack plane orientation on the DBTT

The microcrystalline specimens of the radial testing direction show more or less the same mechanical behavior like those of the tangential orientation, see Figure

E.4. Additional fractographic studies revealed the same features as for the first testing direction already presented before. That implies that the microcrystalline specimens, show no influence of the crack plane orientation on the fracture results. However, comparing the results in Figure E.3 and Figure E.4 for SPD and 300 nm specimens, both testing directions reveal large differences in the absolute fracture toughness values in the low temperature regime. For example, regarding the SPD state tested at -196 °C the fracture toughness has improved from 5.5 MPa $m^{1/2}$ to 22.3 MPa $m^{1/2}$, which is by a factor of ∼4. Almost the same increase was found for room temperature experiments for the SPD microstructure. Through fractographic studies this exceptional toughening can be explained.

Fractography of the radial orientation

In Figure E.7a an overview fractograph of the SPD microstructure tested at -196 °C is presented.

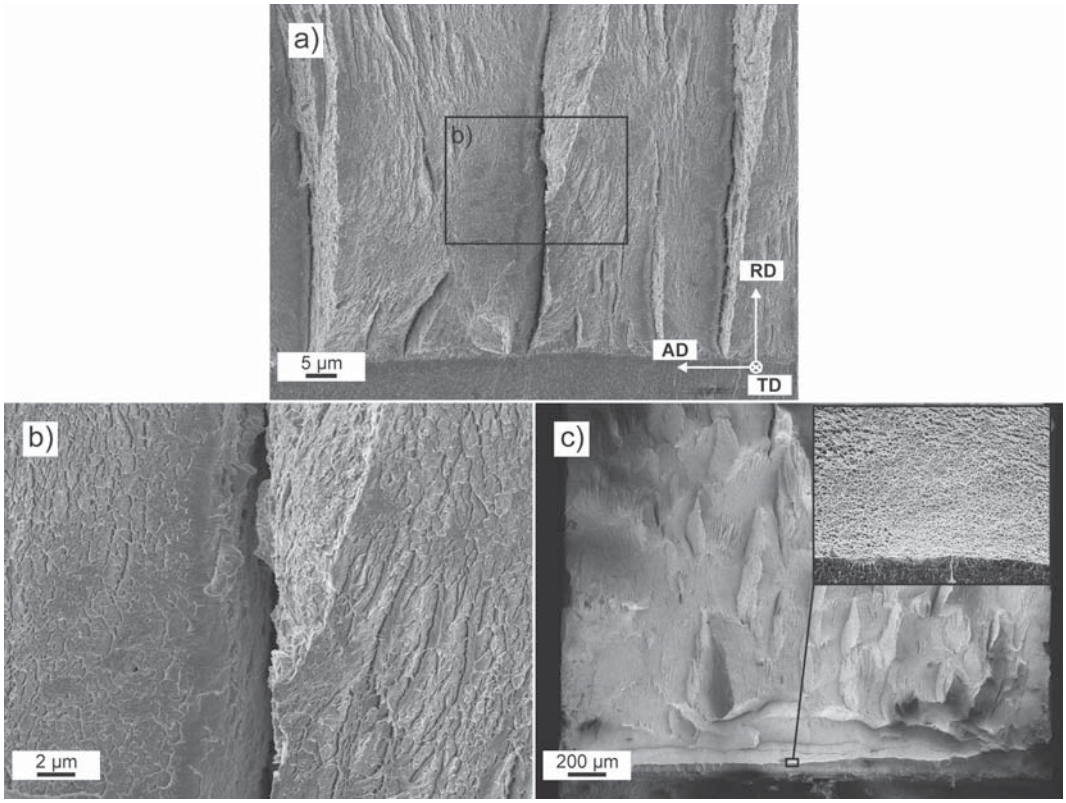

Figure E.7 Selection of fractographs presenting fracture surfaces of specimens with a radial specimen orientation: (a) Overview fractograph of SPD iron tested at -196 °C showing delamination cracks perpendicular to the actual fracture surface. (b) Detailed view of (a) revealing a dimpled fracture surface between a delamination. (c) Overview of a specimen with nominal grain size 300 nm tested at room temperature showing dimple fracture (inserted micrograph) followed by various delaminations.

Additionally, the coordinate system is displayed, and is the same for all three micrographs. In the lower part of the image the fatigue pre-crack is visible. The overload fracture has single secondary cracks or delaminations which are parallel to the crack propagation direction, which is the radial direction (RD). Such delaminations are well known to increase the fracture toughness of a material. This delamination induced toughening mechanism is explained for instance by Hertzberg [17]. The stress state in the immediate vicinity in front of the crack tip consists of very high tensile stresses due to the high tensile triaxiality. Through the occurrence of these delaminations the stress component in the thickness direction of the specimen is reduced and the specimen behaves like an array of thin specimens, which usually exhibit a higher fracture toughness. In order to understand the origin of the delaminations better, Figure E.7 must be examined again.

Here it can be seen that for specimens with tangential orientation the crack opening direction will be the axial direction (AD) of the HPT sample according to the used coordinate system. The delaminations of specimens with the radial specimen orientation also have the axial direction as the crack opening direction, see Figure E.7a. Therefore it can be concluded that the occurrence of the delamination is promoted by the low fracture toughness of the tangential orientation, which was previously discussed in the "Fractography of the tangential orientation" section, when it can be assumed that pre-existing flaws are present.

These delaminations divide the specimen into smaller ligaments which experience a less pronounced triaxiality. The plane stress state allows plastic deformation, which can be seen in a higher magnification of Figure E.7a better, visible in Figure E.7b. Here many small dimples can be found, which can form between the material delaminations. At this stage it should be pointed out that in this case the improvement of the toughness is here not accomplished by the small grain size but rather by the low fracture toughness of the other testing direction discussed before. Since the mechanical measurements of the specimens with microcrystalline microstructures become invalid before room temperature is reached, compared to the 300 nm specimens, it can be assumed that the fracture toughness is again higher leading to a lower DBTT for the microcrystalline states compared to the submicrocrystalline samples. Although dimples can be found at liquid nitrogen temperature in the SPD and 300 nm states, the fracture toughness is still lower for the submicrocrystalline specimens compared to their microcrystalline counterparts which show transcrystalline fracture already.

At room temperature the delamination induced toughening mechanism is still working for the SPD state and partly also for the specimen with 300 nm grain size, which is illustrated in Figure E.7c, where still many delamination can be seen on the fracture surface. However at the very beginning of the overload fracture surface also a large stretched zone is visible consisting of fine dimples, see detailed image section in Figure E.7c. This stretched zone indicates the high fracture toughness. For larger grain sizes delaminations cannot be found and therefore the fracture behaviour becomes more or less isotropic.

E.5 Conclusions and summary

In this paper the fracture behavior of a bcc metal, ARMCO-iron, as a function of the grain size in a wide range of testing temperatures was analyzed. The main results are as follows:

1. It was found that the DBTT is higher for submicrocrystalline grain sizes compared to microcrystalline microstructures. This behavior was related to the intercrystalline crack path for grain sizes smaller than 1 μm.

2. Simultaneously this crack path and the connected low fracture toughness favors the anisotropy of the fracture behavior. Due to delamination induced toughening a pronounced increase in the fracture toughness for the radial specimen orientation was achieved.

3. Interesting for room temperature applications it could be shown that a heat-treatment increasing the grain size from the SPD state (200 nm) to 300 nm can increase the fracture toughness significantly.

In the future the analyses of the plastic deformation behavior by tensile or compression tests ranging from -196 °C to room temperature should help for a deeper understanding of the observed fracture mechanism, especially for the understanding of the intercrystalline crack path.

Bibliography to paper E

[1] A.A. Griffith, Philos. Trans. R. Soc. London 221 (1920) 163-198.

[2] J.R. Rice, R. Thomson, Phil. Mag. 29 (1974) 73-97.

[3] J.H. Chen, Q. Wang, G.Z. Wang, Z. Li, Acta Mater. 51 (2003) 1841-1855.

[4] M.A.Meyers, A. Mishra, D.J. Benson, Prog. Mater. Sci. 51 (2006) 427-556.

[5] R.Z. Valiev, R.K. Islamgaliev, I.V. Alexandrov, Prog. Mater. Sci. 45 (2000) 103-189.

[6] A.P. Zhilyaev, T.G. Langdon, Prog. Mater. Sci. 53 (2008) 893-979.

[7] S. Suresh, Eng. Frac. Mech. 21 (1985) 453-463.

[8] A. Hohenwarter, A. Bachmaier, B. Gludovatz, S. Scheriau, R. Pippan, Int. J. Mat. Res. (formerly Z.Metallkunde) 100 (2009) 1653-1661.

[9] A. Vorhauer, R. Pippan, Scripta Mater. 51 (2004) 921-925.

[10] C. Xu, Z. Horita, T.G. Langdon, Acta Mater. 56 (2008) 5168-5176.

[11] A. Vorhauer, R. Pippan, Metall. Mater. Trans. A 39 (2008) 417-429.

[12] R. Song, D. Ponge, D. Raabe, Acta Mater. 53 (2005) 4881-4892.

[13] T. Inoue, F. Yin, Y. Kimura, K. Tsuzaki, S. Ochiai, Metall. Mater. Trans. A 41 (2009) 341-355.

[14] A. Hohenwarter, R. Pippan, Mater. Sci. Eng. A 527 (2010) 2649-2656.

[15] J.W. Morries Science 320 (2008) 1022-1023.

[16] A. Latapie, D. Farkas, Phys. Rev. 69 (2004) 134110-1 - 134110-9.

[17] R.W. Hertzberg, Deformation And Fracture Mechanics Of Engineering Materials, 4th ed., John Wiley & Sons Inc., New York , 1996.